NASA TM X-668

TECHNICAL MEMORANDUM

X-668

SUBSONIC LONGITUDINAL AERODYNAMIC CHARACTERISTICS OF A 1/30-SCALE CANARD-AIRPLANE MODEL HAVING A WING WITH AN ASPECT RATIO OF 6.0

By William B. Igoe, Francis J. Capone, and Richard J. Re

Langley Research Center
Langley Station, Hampton, Va.

[redacted]

NATIONAL AERONAUTICS AND SPACE ADMINISTRATION
WASHINGTON

June 1962

[redacted]

NATIONAL AERONAUTICS AND SPACE ADMINISTRATION

TECHNICAL MEMORANDUM X-668

SUBSONIC LONGITUDINAL AERODYNAMIC CHARACTERISTICS OF A 1/30-SCALE CANARD-AIRPLANE MODEL HAVING A WING WITH AN ASPECT RATIO OF 6.0*

By William B. Igoe, Francis J. Capone, and Richard J. Re

SUMMARY

An investigation has been conducted to determine the longitudinal aerodynamic characteristics of a 1/30-scale, nuclear-powered canard airplane model having a wing with an aspect ratio of 6.0. The model was tested primarily at Mach numbers from 0.60 to 0.92 for an angle-of-attack range of approximately -2° to 20°. The Reynolds number per foot varied from 2.0×10^6 to 4.5×10^6.

The effects of end plates mounted as vertical tails, wing leading-edge chord-extension deflection, body filler (model cross-sectional area increased), and boundary-layer transition were studied for the model without the canard surface. Tests of the model with the canard surface were conducted with canard-surface deflection angles of -12° to 8° and with canard-surface tab deflections from -8° to 0° at Mach numbers from 0.60 to 0.85.

The model tested was unstable about its selected moment reference center. The test results indicated that the end plates increased the maximum lift-drag ratios up to a Mach number of 0.74 and decreased the model instability at low lift coefficients for all Mach numbers. Deflection of the wing leading-edge chord-extension to 12° resulted in an increase in maximum lift-drag ratio up to a Mach number of 0.75. Trimming the model with the canard surface resulted in a loss of maximum lift-drag ratio, in some cases as much as 2, over that obtained for the untrimmed model without the canard surface. Most of the loss was due to the canard-surface tab deflection required to trim the canard surface.

Author

*Title, Unclassified.

INTRODUCTION

The longitudinal aerodynamic characteristics of a 1/30-scale proposed long-range and long-duration bomber, missile carrier, and airborne-alert aircraft with nuclear-powered jet engines have been investigated in the Langley 16-foot transonic tunnel. The proposed airplane configuration included a free-floating canard surface and wing-tip end plates for vertical tails. The model was tested with the canard surface fixed rather than free floating. This report contains the results of the investigation of the model having a wing with an aspect ratio of 6.0. Similar results for an investigation of the model having a wing with an aspect ratio of 3.6 are contained in reference 1. In addition to the canard-surface effectiveness and loads, the effects of end plates, wing leading-edge chord-extensions, a body filler which increased the model cross-sectional area, and boundary-layer transition on the airplane's stability and performance were determined.

Tests were conducted primarily at Mach numbers from 0.60 to 0.92 and for an angle-of-attack range of approximately -2° to 20°. Some tests to evaluate take-off characteristics were made at a Mach number of 0.30 at angles of attack up to approximately 29°. The test Reynolds number per foot varied from 2.0×10^6 to 4.5×10^6.

SYMBOLS

a	lift-curve slope per deg, $\frac{\partial C_L}{\partial \alpha}$
A	cross-sectional area
$A_{t,\infty}$	free-stream cross-sectional area of stream tube which enters nacelle duct
$\bar{c}$	mean aerodynamic chord of basic wing (11.598 in.)
$\bar{c}_c$	mean aerodynamic chord of exposed canard planform (6.494 in.)
$\bar{c}_{tab}$	mean aerodynamic chord of canard tab (0.943 in.)
C_D	drag coefficient, $\frac{\text{Drag}}{qS}$

$C_{D,i}$ nacelle duct internal-drag coefficient,

$$\frac{2A_i}{S}\left\{\frac{A_{t,\infty}}{A_i} + \frac{1}{\gamma M^2}\frac{A_e}{A_i}\left[1 - \frac{p_e}{p_\infty}\left(1 + \gamma M_e^2\right)\right]\cos(\alpha - 5.5^\circ)\cos 5^\circ\right\}$$

$C_{h,c}$ canard-surface hinge-moment coefficient,

$$\frac{\text{Canard-surface hinge moment (one side)}}{qS_c\bar{c}_c}$$

$C_{h,tab}$ canard-surface tab hinge-moment coefficient, $\dfrac{\text{Tab hinge moment}}{qS_{tab}\bar{c}_{tab}}$

C_L lift coefficient, $\dfrac{\text{Lift}}{qS}$

$C_{L,c}$ canard-surface lift coefficient, $C_{N,c}\cos(\alpha + \delta_c)$

C_m pitching-moment coefficient about $0.249\bar{c}$, $\dfrac{\text{Pitching moment}}{qS\bar{c}}$

$C_{m_{C_L}}$ static longitudinal stability parameter, $\dfrac{\partial C_m}{\partial C_L}$ at $C_L = 0$

$C_{m_{\delta_c}}$ canard-surface effectiveness parameter, $\dfrac{\partial C_m}{\partial \delta_c}$ at $\alpha = 0$

$C_{N,c}$ canard-surface normal-force coefficient,

$$\frac{\text{Canard-surface normal force (one side)}}{qS_c}$$

$C_{p,b}$ base pressure coefficient, $\dfrac{p_b - p_\infty}{q}$

L/D lift-drag ratio

M free-stream Mach number

M_e Mach number at nacelle duct exit

p static pressure, lb/sq ft

[redacted]

q	free-stream dynamic pressure, lb/sq ft
S	planform area of basic wing, includes area covered by fuselage and nacelles (5.258 sq ft)
S_c	canard-surface exposed planform area (one side) (0.21144 sq ft)
S_{tab}	canard-surface tab planform area (one side) (0.012874 sq ft)
α	angle of attack of wing chord plane, positive leading edge up, deg
γ	ratio of specific heats (1.4 for air)
δ_c	canard deflection angle from wing chord plane measured normal to hinge line, positive leading edge up, deg
δ_{le}	outboard leading-edge chord-extension deflection angle from wing chord plane measured normal to hinge line, positive leading edge down, deg
δ_{te}	trailing-edge flap deflection angle from wing chord plane measured normal to hinge line, positive trailing edge down, deg
δ_{tr}	trailing-edge trim-flap deflection angle from wing chord plane measured normal to hinge line, positive trailing edge up, deg
δ_{tab}	canard-surface tab deflection angle from canard-surface chord plane measured normal to hinge line, positive trailing edge down, deg

Subscripts:

b	base
c	canard
e	nacelle duct exit
i	nacelle duct inlet
∞	free stream
max	maximum
min	minimum

L 1 8 4 0

CON[redacted]

MODEL COMPONENT DESIGNATIONS AND ABBREVIATIONS

The following designations are used in the present paper to identify the various components of the model:

B	fuselage and nacelles with modified rear end
B_1	B with filler
C	canard
E	wing end plate
W	wing with outboard leading-edge chord-extension

The following abbreviations are used in the present paper to identify various distances measured on the model:

BL	buttock lines, in.
WL	water lines, in.
FS	fuselage station, measured positive rearward from a reference point 1/2 in. ahead of actual fuselage nose, in.
WS	wing station, measured positive rearward from leading-edge apex, in.
SS	span station, measured positive outboard from plane of symmetry in wing or canard-surface chord plane, in.

MODEL, APPARATUS, AND PROCEDURE

Model

The 1/30-scale model consisted of a wing with an aspect ratio of 6.0 and end plates, a fuselage, a canard surface, and flow-through nacelles. A photograph of the model with the canard sting mounted in the wind tunnel is shown in figure 1. A sketch of the complete model with overall dimensions is shown in figure 2.

Wing.- The wing details are given in table I and the planform geometry is shown in figure 3. The basic wing plan form had an aspect ratio of 6.339 but this was decreased to 6.000 by the addition of an outboard leading-edge chord-extension. A take-off configuration was represented

by deflection of plain trailing-edge flaps and trailing-edge trim flaps. When the trailing-edge flaps were deflected down, the trailing-edge trim flaps were deflected up to trim out the pitching moment caused by the flaps.

End plates.- The wing-tip end plates served as vertical tails. They had sweptback planforms with about 75 percent of the surface area above the wing chord plane and the remainder beneath. The end-plate geometry is shown in figure 3 and details are given in table I.

Fuselage.- The fuselage, shown in figure 4, had an overall length of 59.333 inches, a maximum height including the ducts of 5.937 inches, and a maximum width including ducts of 13.706 inches. There was a simulated canopy shape near the nose, and the sides of the fuselage were flat in the vicinity of the canard surface. The rear end of the fuselage differed from the proposed airplane shape so that the model could be sting mounted in the wind tunnel. In order to allow for the presence of the sting cavity, the nacelle inboard duct exits were also altered. These differences between the model and the proposed airplane are shown in figure 5 which also shows that some external duct-exit shroud geometry was not duplicated.

L 1840

Nacelles.- Two nacelles were mounted side by side near the rear of the fuselage. The elliptical inlets were located at the side of the fuselage just forward and below the wing leading edge. The external geometry of the nacelles may be seen in figure 4 and the nacelle internal ducting is illustrated in figure 6. Each duct had two exits, with the area of the inboard exits for each duct decreased (see fig. 5) because of the presence of the model-sting cavity as has already been indicated.

The duct internal cross-sectional-area distribution is given in figure 7. Internal blockage was provided in the ducts by a screen, of about 70-percent porosity, installed just forward of the duct splitter plate for the inboard and outboard exits. The external geometry of the nacelles was varied with the use of a filler, as shown in figure 4, to simulate an alternate power plant configuration.

Canard surface.- The canard surface was located at the nose of the fuselage with the hinge line normal to the plane of symmetry, 31.863 inches forward of and 2.634 inches below the model moment reference center. Although the airplane canard is free floating, the model canard was fixed, but its incidence was variable about the hinge line from -12° to 20°. A sketch of the canard planform is shown in figure 8 and geometrical details are given in table I. A trailing-edge tab on the canard was used to obtain canard moment trim conditions about the hinge line. Because the sides of the fuselage were flat in the vicinity

of the canard, the canard root chord fit relatively flush with the fuselage side and any canard unporting throughout the range of canard deflection angles was eliminated.

Area distribution.- Cross-sectional area distributions of the various model components are shown in figure 9. In figure 10, total area distributions for the model with and without filler are compared with the area distribution the model would have if its external geometry had not been altered due to the presence of the sting cavity. External wetted areas for the model configurations are given in table II.

Boundary-layer transition grain pattern.- For most of the tests in which the boundary-layer transition point was fixed, No. 120 carborundum grains were sparsely distributed in a thin film of shellac in strips near the leading edges of the various model components. On the wing a 0.40-inch-wide strip was parallel to and 0.60 inch behind the leading edge. On the end plates, nacelles, and canard, a 0.25-inch-wide strip was parallel to and 0.40 inch behind the leading edge. On the fuselage, a 0.25-inch-wide circumferential strip was 0.75 inch behind the nose. All distances are measured in the streamwise direction. Configuration BWE with $\delta_{le} = 12^{\circ}$ was also tested with free transition.

Instrumentation

The model forces and moments were measured with a six-component internal strain-gage balance. The canard was instrumented with strain gages to measure canard normal force, hinge moment, and tab hinge moment. The model angles of attack were determined with an internal pendulum-type attitude indicator. Canard attitudes, however, were determined from deflection calibrations under load.

The nacelle-duct internal flow characteristics were determined with temporary duct-exit rakes consisting of static- and stagnation-pressure probes. Permanently installed model pressure instrumentation consisted of inlet stagnation-pressure rakes and throat- and maximum-area static-pressure orifices. This permanent instrumentation was calibrated with the exit-pressure data so that the nacelle internal flow characteristics could be determined when the temporary rakes were removed during the force tests. The duct pressure instrumentation is shown in figure 12.

Model base pressure was measured during the tests by means of three static-pressure taps distributed around the model base.

[redacted]

Wind Tunnel

The model was sting mounted (as shown in fig. 1) in the Langley 16-foot transonic tunnel which is described in reference 2. This is a single-return wind tunnel with a slotted octagonal throat and is operated at atmospheric stagnation pressures. The wind-tunnel model-support system pivoted so that the balance moment center remained near the center of the test section throughout the angle-of-attack range.

Data Reduction

All forces and moments have been reduced to standard coefficient form with the model force data referred to the stability axis system. The nacelle internal drag has been subtracted from the model drag. The nacelle internal-drag coefficients $C_{D,i}$ are presented in figure 12 for the model without the canard (BWE with $\delta_{le} = 12^\circ$ and $\delta_{le} = 25^\circ$) and for the model with the canard (BCWE with $\delta_{le} = 12^\circ$). In addition, model forces have been adjusted to the condition of free-stream static pressure existing at the base. Typical model base pressure coefficients for models BWE and B_1WE with $\delta_{le} = 12^\circ$ and BWE with $\delta_{le} = 25^\circ$ are presented in figure 13. As mentioned previously, the model angle of attack was determined independently with an attitude transmitter. The canard-surface incidence settings were corrected for deflections under load. No other corrections or adjustments have been applied to the data.

Accuracy

The accuracy of the data, based on instrumentation error and repeatability, has been estimated to be:

M	± 0.01
α, deg	± 0.1
δ_c, deg	± 0.2
δ_{tab}, deg	± 0.5

At $M = 0.30$,

C_L	± 0.030
C_D at low C_L	± 0.004
C_D at high C_L	± 0.020
C_m	± 0.020

[redacted]

At M = 0.60 to M = 0.98,

C_L	±0.010
C_D at low C_L	±0.001
C_D at high C_L	±0.005
C_m	±0.005
$C_{N,c}$	±0.010
$C_{h,c}$	±0.001
$C_{h,tab}$	±0.002

TESTS

Most of this investigation was conducted at Mach numbers from 0.60 to 0.92 and through an angle-of-attack range of approximately -2° to 20°. A body alone configuration (B) was also tested at Mach numbers of 0.95 and 0.98. Another configuration (BWE with $\delta_{te} = 25°$, $\delta_{tr} = 25°$, and $\delta_{le} = 25°$ or $\delta_{le} = 40°$) was tested as a take-off configuration at M = 0.30 at angles of attack up to 29°. The Reynolds number per foot varied from 2.0×10^6 to 4.5×10^6 (fig. 14). All configurations were tested with transition fixed except for configuration BWE with $\delta_{le} = 12°$ which was tested with and without transition. The test variables are summarized in table III.

PRESENTATION OF RESULTS

The results of this investigation are plotted in coefficient form. Basic aerodynamic data for the configuration without the canard are shown in figures 15 to 24 and summary data are given in figures 25 to 34. Basic data for the configuration with the canard are presented in figures 35 to 41. Canard loads data are shown in figures 42 to 48 and canard tab loads data are shown in figure 49. Trimmed drag polars are presented in figure 50 for the configuration with the canard. Table III lists the configurations, test conditions, and the numbers of the figures in which the results are given.

DISCUSSION

The basic force data without the canard (figs. 15 to 21) show that the model is unstable about its moment reference center. In order to

show the cause of this instability, the pitching-moment coefficients for configurations B (body alone) and BW (body and wing without end plates) have been plotted against angle of attack in figure 22. In this figure, the difference between the pitching-moment coefficients of configurations BW and B is the contribution of the wing pitching moment plus the mutual interference effects of the wing and body. It is evident that the wing-body instability is caused by the body which is highly unstable about the selected moment reference center. However, the wing itself has a stable contribution and its addition to the body reduces the instability.

Force Data for Model Without the Canard

Effects of end plates.- The effects of end plates can be found by comparing configurations BW and BWE in the basic-data figures 16 and 17 and in the summary figures 25 to 29. The addition of the end plates helped to decrease the model instability at $C_L = 0$ (fig. 26). As seen in figure 25, there is an increase in lift-curve slope with the addition of end plates at Mach numbers up to 0.80. At Mach numbers up to 0.75 (fig. 28), the value of $(L/D)_{max}$ is higher for BWE than for BW even though figure 27 shows that for all Mach numbers BWE has a higher value of $C_{D,min}$ than does BW. The increase in $(L/D)_{max}$ is a result of an increase in the effective aspect ratio of the wing with the addition of end plates.

Effect of deflection of leading-edge chord-extension.- The effect of deflecting the leading-edge chord-extension can be found by comparing $\delta_{le} = 0^\circ$, 12°, and 25° for configuration BWE in the basic-data figures 17 to 19 and in the summary figures 30 to 34. Figure 31 shows that the model with $\delta_{le} = 0^\circ$ was less unstable at $C_L = 0$ than the model with either $\delta_{le} = 12^\circ$ or $\delta_{le} = 25^\circ$, the model with the chord-extension deflection of 25° being very unstable. However, the model with $\delta_{le} = 12^\circ$ exhibited less abrupt instability at high lift coefficients than the model with $\delta_{le} = 0^\circ$ (figs. 17(c) and 18(c)).

The maximum lift-drag ratio (fig. 33) was higher for $\delta_{le} = 12^\circ$ than for $\delta_{le} = 0^\circ$ up to $M = 0.74$ even though $C_{D,min}$ (fig. 32) was higher at all Mach numbers for $\delta_{le} = 12^\circ$ than for $\delta_{le} = 0^\circ$. This increase in the value of $(L/D)_{max}$ may be due to an improvement in wing-span load efficiency with chord-extension deflection. However, the value of $C_{D,min}$ for $\delta_{le} = 25^\circ$ was much higher than for the other two chord-extension settings with a resulting large loss in the value of $(L/D)_{max}$.

The deflection of the leading-edge chord-extension of 12° resulted in the highest lift-curve slope (fig. 30) at Mach numbers up to 0.82. Because of this higher lift-curve slope and also because of better high-lift stability and $(L/D)_{max}$ characteristics, a deflection of the leading-edge chord-extension of 12° was probably near the best chord-extension deflection for cruise conditions.

Effect of body filler.- The effect of body filler can be found by comparing models BWE and B_1WE in the basic-data figures 17 and 20 and in the summary figures 25 to 29. The addition of the body filler decreased the instability at $C_L = 0$ (fig. 26), and the model became slightly stable at $M = 0.92$. However, the addition of body filler caused more high-lift instability (figs. 17(c) and 20(c)). The body filler also caused a reduction in lift-curve slope at Mach numbers up to 0.78 (fig. 25), a small increase in $C_{D,min}$ (fig. 27), and a decrease in $(L/D)_{max}$ (fig. 28).

Effect of boundary-layer transition.- The effect of boundary-layer transition can be found by comparing basic-data figures 17 and 21 and summary figures 25 to 29 for configuration BWE ($\delta_{le} = 12°$) with and without fixed boundary-layer transition. The effect of fixing boundary-layer transition can best be seen by examination of the basic-data figures. For the model with free transition at Mach numbers of 0.80, 0.83, and 0.875, abrupt changes in C_L and C_D occur (figs. 21(a) and 21(b)) which are probably caused by local flow separation. There is also very abrupt high-lift instability (fig. 21(c)) at the same Mach numbers. The model with free transition was also more unstable at $C_L = 0$ as shown by the data for $C_{m_{C_L}}$ in figure 26. An expected decrease in $C_{D,min}$ (fig. 27) resulted in an increase in $(L/D)_{max}$ (fig. 28).

Take-off characteristics.- A comparison of the take-off characteristics of configuration BWE with $\delta_{le} = 25°$ and 40°, $\delta_{te} = 25°$, and $\delta_{tr} = 25°$ is shown in the basic-data figures 23 and 24. The maximum lift coefficient obtained was about 1.13 for both chord-extension deflections. Both chord-extension deflections gave neutral or slightly negative stability at low lift coefficients with an abrupt increase in stability near a C_L of 1.0.

Force Data for Model With the Canard

A fixed canard is generally destabilizing; and since the model was tested with a fixed canard, the model was more unstable with the canard than without it. However, for the airplane, the canard would be free

floating so that its aerodynamic contribution would be essentially for trim purposes and would not affect the longitudinal stability. This characteristic of free-floating canards for use as longitudinal trim controls is discussed in reference 3. The results of the investigation of the model with the canard are presented in figures 35 and 36 for configuration BC and in figures 37 to 41 for configuration BCWE with $\delta_{le} = 12^\circ$. These results can be compared with configuration BWE with $\delta_{le} = 12^\circ$ (fig. 17) for the effects of the canard.

Since the canard was fixed in this investigation, the effect of a free-floating canard on data for C_L, C_D, and C_m is difficult to determine because it is necessary to interpolate for conditions where both the model moments about the moment reference center and the canard hinge moments about the canard hinge line are simultaneously trimmed. Sufficient data to cross plot for interpolation at these conditions are available only at $M = 0.80$, and therefore the possible comparisons of the model with and without the canard would be limited to a single point. However, some canard effects can be seen from the untrimmed data of figures 37 to 41. The fixed canard caused slight increases in the lift-curve slope and $C_{D,min}$ in addition to making the model more unstable.

L 1840

Trimmed drag polars.- In order to determine the effects of the canard on maximum trimmed lift-drag ratios, drag polars were constructed for the model trimmed about $0.169\bar{c}$. This forward shift of the moment reference center from $0.249\bar{c}$ resulted in a stable configuration without the canard (BWE with $\delta_{le} = 12^\circ$) with a static margin of from 1 to 4 percent at Mach numbers from 0.60 to 0.85. The trimmed drag polars, determined only for trimmed model moments and not for trimmed canard-surface hinge-line moments, are presented for configuration BCWE with $\delta_{le} = 12^\circ$ in figure 50 for $\delta_{tab} = -4^\circ$ at $M = 0.60$, $M = 0.80$, and $M = 0.85$, and at $M = 0.80$ for $\delta_{tab} = 0^\circ$, $\delta_{tab} = -4^\circ$, and $\delta_{tab} = -8^\circ$.

The following table shows a comparison of trimmed and untrimmed maximum lift-drag ratios for the model with $\delta_{le} = 12^\circ$:

M	BCWE		BWE	BW
	δ_{tab}, deg	Trimmed $(L/D)_{max}$	Untrimmed $(L/D)_{max}$	Untrimmed $(L/D)_{max}$
0.80	0	12.5	12.6	12.8
.60	-4	14.9	16.2	15.7
.80	-4	11.6	12.6	12.8
.85	-4	9.2	10.2	10.6
.80	-8	10.6	12.6	12.8

A comparison of the data in the table shows that the use of the canard for trim resulted in a loss up to about 2 in $(L/D)_{max}$.

For $M = 0.80$, the canard hinge moments are nearly trimmed at $(L/D)_{max}$ on the drag polars of figure 50 for $\delta_{tab} = -4^{o}$. The variation of $(L/D)_{max}$ with δ_{tab} at $M = 0.80$ shows that significant losses can result from the tab deflections which may be necessary to trim the canard hinge moments.

Canard and tab loads.- The canard normal-force and hinge-moment coefficients are presented in figures 42 to 48 and the canard tab hinge-moment coefficients are presented in figure 49. By comparing appropriate data figures, the interference effects of the canard on model components such as the body or wing, or the model components on the canard are seen to be small except for the interference effects of the body on the canard. This effect is evident in the data for $C_{N,c}$ in figures 42 to 48. When the canard should have been alined with the free stream ($\alpha + \delta_c = 0$), $C_{N,c}$ should have been zero. The measured load on the canard at this condition was probably due to an induced flow field at the body nose.

The variation of $C_{h,c}$ with α at fixed δ_c or with δ_c at fixed α indicates that the canard was generally stable about its hinge line. The nonlinearities present in the data for $C_{h,c}$ were apparently associated with the local angle of attack and not due to body interference. This may be seen from the data for $C_{h,c}$ in figure 46(c) where $C_{h,c}$ is plotted against the canard angle of attack $\alpha + \delta_c$.

Canard effectiveness.- The canard effectiveness parameter $C_{m_{\delta_c}}$ was obtained from the data for C_m in figures 35 to 41 at a constant angle of attack ($\alpha = 0^{o}$). The value of $C_{m_{\delta_c}}$ has also been calculated from the exposed panel canard loads (with no allowance for fuselage carryover or canard chord-force effects) by the following equation:

$$C_{m_{\delta_c}} = 2\,\frac{S_c}{S}\left[\frac{\partial C_{L,c}}{\partial \delta_c}\,\frac{d}{\bar{c}} + \frac{\partial C_{h,c}}{\partial \delta_c}\,\frac{\bar{c}_c}{\bar{c}}\right]$$

where d is the distance from the canard hinge line to the model moment reference center. These results are compared in the following table:

Configuration	δ_{le}, deg	M	δ_{tab}, deg	$\frac{\partial C_{L,c}}{\partial \delta_c}$	$\frac{\partial C_{h,c}}{\partial \delta_c}$	Calculated $C_{m_{\delta_c}}$	Measured $C_{m_{\delta_c}}$
BC		0.80	0	0.0437	-0.0028	0.0095	0.0103
BC		.85	0	.0475	-.0035	.0104	.0103
BCWE	12	.80	0	.0430	-.0024	.0094	.0101
BCWE	12	.60	-4	.0432	-.0024	.0094	.0099
BCWE	12	.80	-4	.0435	-.0027	.0095	.0100
BCWE	12	.85	-4	.0426	-.0025	.0093	.0098
BCWE	12	.80	-8	.0438	-.0027	.0096	.0098

The measured values of $C_{m_{\delta_c}}$ indicate that the canard effectiveness is not influenced appreciably by canard tab deflection, Mach number variation (from M = 0.60 to 0.85), or the presence of the wing.

A comparison of the calculated and measured canard effectiveness $C_{m_{\delta_c}}$ shows that this parameter could be satisfactorily predicted from $C_{L,c}$ and $C_{h,c}$ despite the neglect of body carryover loads and canard chord force.

CONCLUSIONS

A wind-tunnel investigation of the longitudinal aerodynamic characteristics of a 1/30-scale subsonic, nuclear-powered canard airplane model which was longitudinally unstable for the selected moment reference center, indicated the following conclusions:

1. The addition of end plates as vertical tails increased the maximum lift-drag ratio up to a Mach number of 0.75 and decreased the model instability at low lift coefficients and at all Mach numbers.

2. Deflection of the wing leading-edge chord-extension to 12° resulted in an increase in maximum lift-drag ratio up to a Mach number of 0.74 and also decreased the abrupt model instability at high lift coefficients.

3. The addition of a body filler which increased the cross-sectional area of the model decreased the model instability at low lift coefficients and caused small increases in minimum drag.

4. The addition of a canard with its associated loads for longitudinal trim resulted in a loss of maximum lift-drag ratio, in some cases as much as 2, over that obtained for the untrimmed model without the canard. Most of the loss was a result of canard tab deflection required to trim the canard.

5. Canard effectiveness was not influenced appreciably by canard tab deflection, Mach number variation, or the presence of the wing.

Langley Research Center,
National Aeronautics and Space Administration,
Langley Air Force Base, Va., January 24, 1962.

REFERENCES

1. Igoe, William B., Re, Richard J., and Capone, Francis J.: Longitudinal Aerodynamic Characteristics of a 1/30-Scale Subsonic Canard-Airplane Model Having a Wing With an Aspect Ratio of 3.6 at Mach Numbers From 0.30 to 0.98. NASA TM X-669, 1962.

2. Ward, Vernon G., Whitcomb, Charles F., and Pearson, Merwin D.: Air-Flow and Power Characteristics of the Langley 16-Foot Transonic Tunnel With Slotted Test Section. NACA RM L52E01, 1952.

3. Bates, William R.: Low-Speed Static Longitudinal Stability Characteristics of a Canard Model Having a 60° Triangular Wing and Horizontal Tail. NACA RM L9H17, 1949.

TABLE I.- MODEL GEOMETRICAL CHARACTERISTICS

Wing:	
Aspect ratio -	
Basic planform	6.339
Including leading-edge chord-extension	6.000
Planform area -	
Basic planform, sq ft	[a]5.258
Including leading-edge chord-extension, sq ft	5.556
Mean aerodynamic chord (basic planform) -	
Length, in.	[a]11.598
Fuselage station of leading edge, in.	36.554
Fuselage station of 0.25$\bar{c}$, in.	39.454
Taper ratio, basic planform	0.400
Quarter-chord sweepback angle, deg	33.833
Root-chord incidence (relative to WL plane), deg	3.50
Dihedral angle outboard of SS 6.333, deg	4
Airfoil section (linear variation of airfoil thickness between SS) at -	
SS 0	NACA 0011.7-65 (modified)
SS 6.333	NACA 0011-65
SS 20.768	NACA 0008.5-65
SS 20.768	NACA 0008.5-65 (modified)
SS 34.641	NACA 0007.6-65 (modified)
End plate - upper part:	
Planform area (one side), sq ft	0.323
Taper ratio	0.2083
Airfoil section	NACA 0008-65
End plate - lower part:	
Planform area (one side), sq ft	0.094
Airfoil section	NACA 0007.3-65
Canard:	
Aspect ratio	2.093
Planform area, sq ft	0.724
Exposed area (one side), sq ft	[a]0.211
Exposed semispan, in.	5.384
Mean aerodynamic chord, in.	[a]6.494
Dihedral angle, deg	0
Airfoil section	NACA 0006-64
Hinge-line sweepback angle, deg	0
Tab area (one side), sq ft	[a]0.013
Tab mean aerodynamic chord, in.	[a]0.943

[a]Data reduction constant.

TABLE II.- WETTED AREAS

Configuration	Area, sq in.
BW	2,663
BWE	2,891
B_1WE	2,958
BCWE	3,020

TABLE III.- INDEX TO FIGURES

(a) Basic data

Configuration	Mach number	δ_{le}, deg	δ_c, deg	δ_{tab}, deg	δ_{te}, deg	δ_{tr}, deg	Boundary-layer transition	Figure
Model forces								
B	0.60 to 0.98				0	0	Fixed	15
BW	.60 to .92	12			0	0	Fixed	16
BWE	.60 to .92	12			0	0	Fixed	17
BWE	.60 to .92	0			0	0	Fixed	18
BWE	.60 to .92	25			0	0	Fixed	19
B_1WE	.60 to .92	12			0	0	Fixed	20
BWE	.60 to .92	12			0	0	Free	21
BWE	.30	25			25	25	Fixed	23
BWE	.30	40			25	25	Fixed	24
BC	.80		-12, 0	0			Fixed	35
BC	.85		-14, -2	0			Fixed	36
BCWE	.80	12	-12 to 0	0	0	0	Fixed	37
BCWE	.60	12	-12 to 4	-4	0	0	Fixed	38
BCWE	.80	12	-12 to 4	-4	0	0	Fixed	39
BCWE	.85	12	-12 to 4	-4	0	0	Fixed	40
BCWE	.80	12	-8 to 8	-8	0	0	Fixed	41
Canard loads								
BC	0.80		-12, 0	0			Fixed	42
BC	.85		-14, -2	0			Fixed	43
BCWE	.80	12	-12 to 0	0	0	0	Fixed	44
BCWE	.60	12	-12 to 4	-4	0	0	Fixed	45
BCWE	.80	12	-12 to 4	-4	0	0	Fixed	46
BCWE	.85	12	-12 to 4	-4	0	0	Fixed	47
BCWE	.80	12	-8 to 8	-8	0	0	Fixed	48
Trim tab loads								
BCWE	0.60, 0.80, and 0.85	12	-12 to 8	-8, -4, 0	0	0	Fixed	49

TABLE III.- INDEX TO FIGURES - Concluded

(b) Summary of Data

	Figure
Comparison of configurations B and BW with $\delta_{le} = 12^{\circ}$ for C_m	22
Comparison of configurations BWE (free transition), BW, BWE, and B_1WE with $\delta_{le} = 12^{\circ}$ for -	
a	25
$C_{m_{C_L}}$	26
$C_{D,min}$	27
$(L/D)_{max}$	28
C_L for $(L/D)_{max}$	29
Effect of leading-edge chord-extension deflection for configuration BWE with $\delta_{le} = 0^{\circ}$, 12°, and 25° for -	
a	30
$C_{m_{C_L}}$	31
$C_{D,min}$	32
$(L/D)_{max}$	33
C_L for $(L/D)_{max}$	34
Trimmed drag polars for configuration BCWE with $\delta_{le} = 12^{\circ}$	50

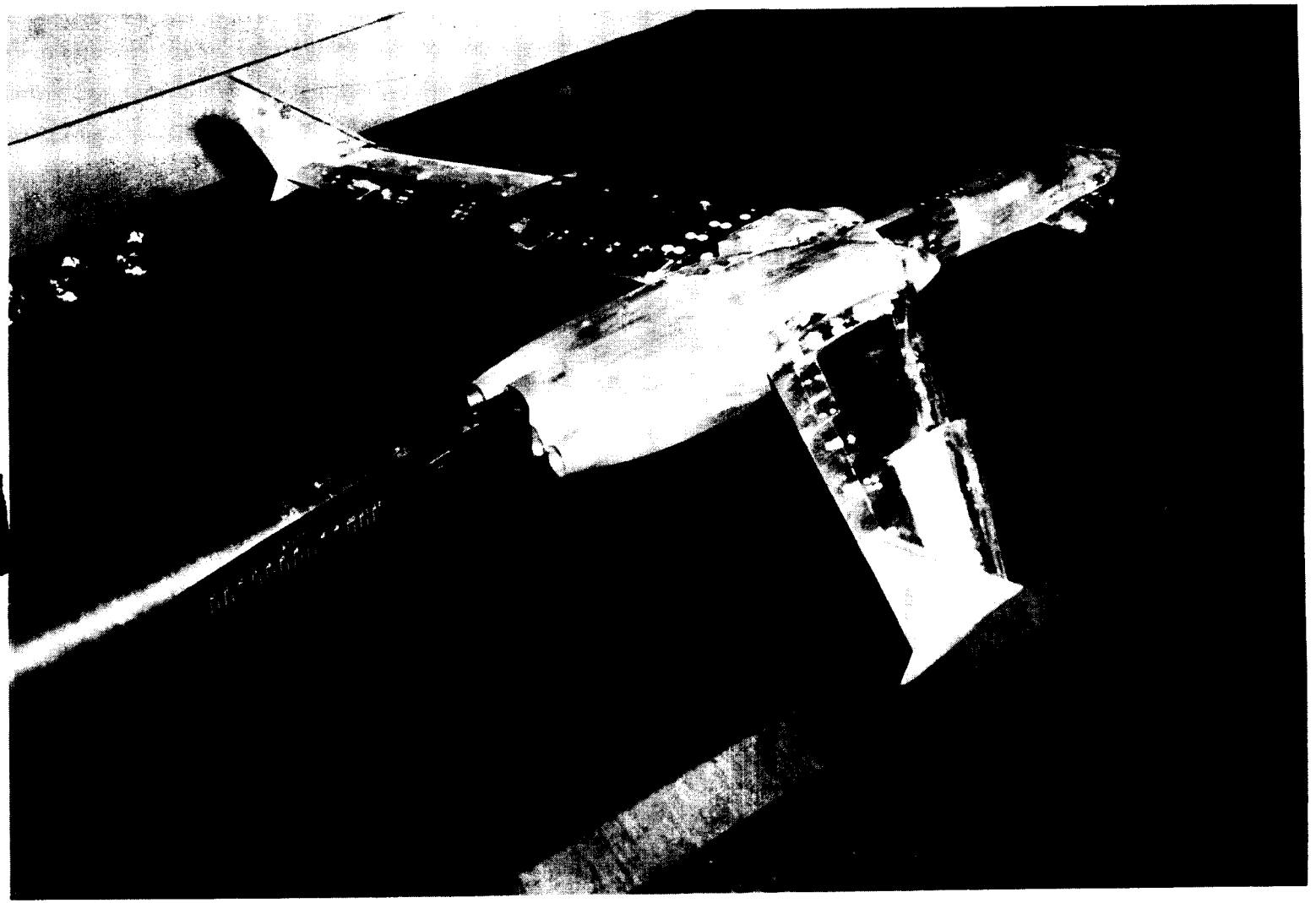

L-60-1385.1

Figure 1.- Photograph of configuration BCWE ($\delta_{le} = 12^{\circ}$) in Langley 16-foot transonic tunnel.

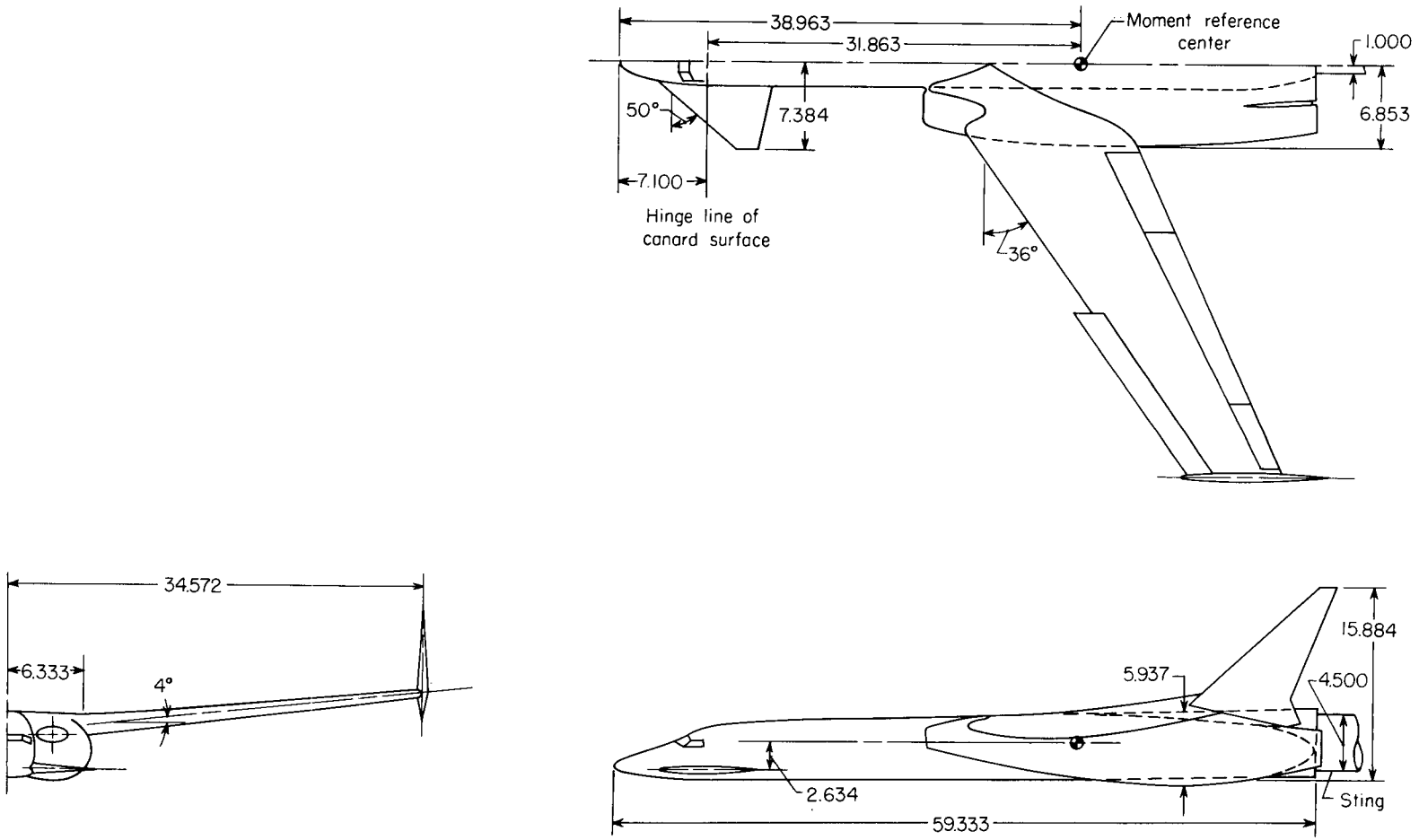

Figure 2.- General arrangement of model. All dimensions in inches unless otherwise noted.

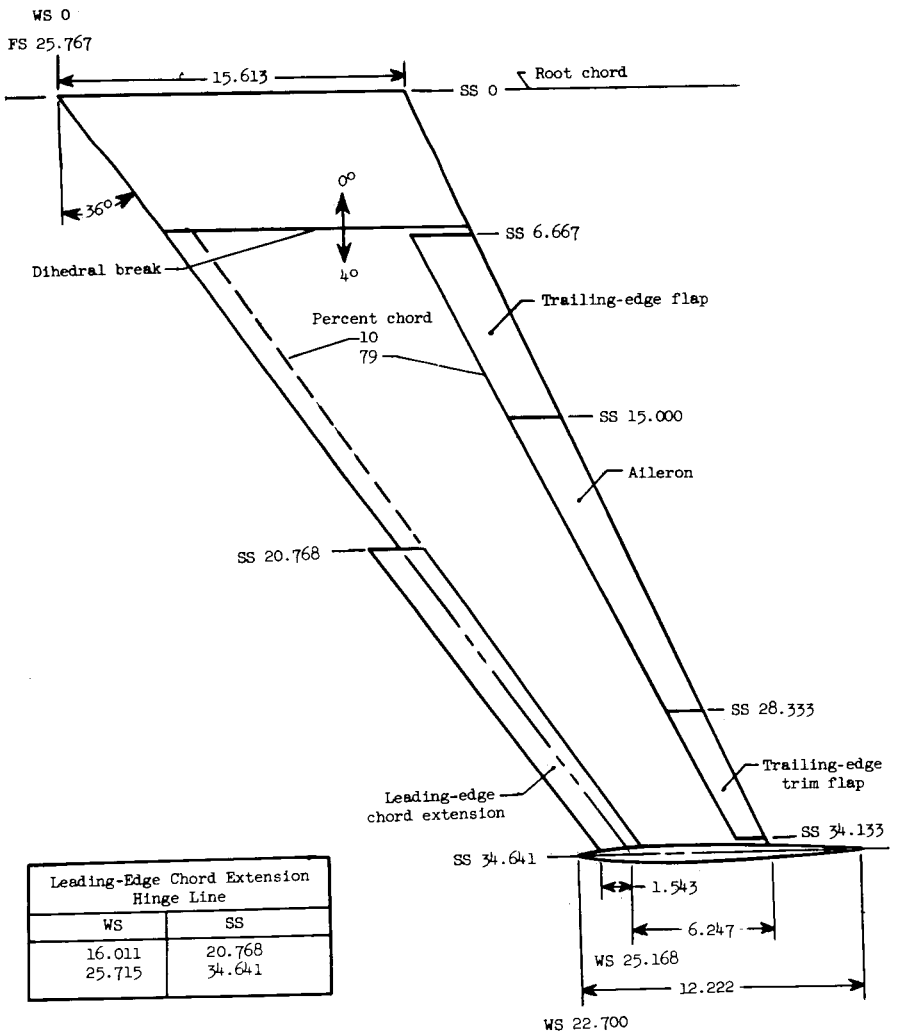

Leading-Edge Chord Extension Hinge Line	
WS	SS
16.011 25.715	20.768 34.641

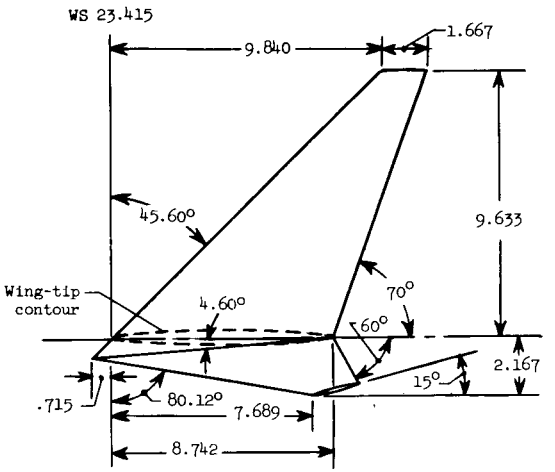

Figure 3.- Dimensional details of wing and end plates. All dimensions in inches unless otherwise noted.

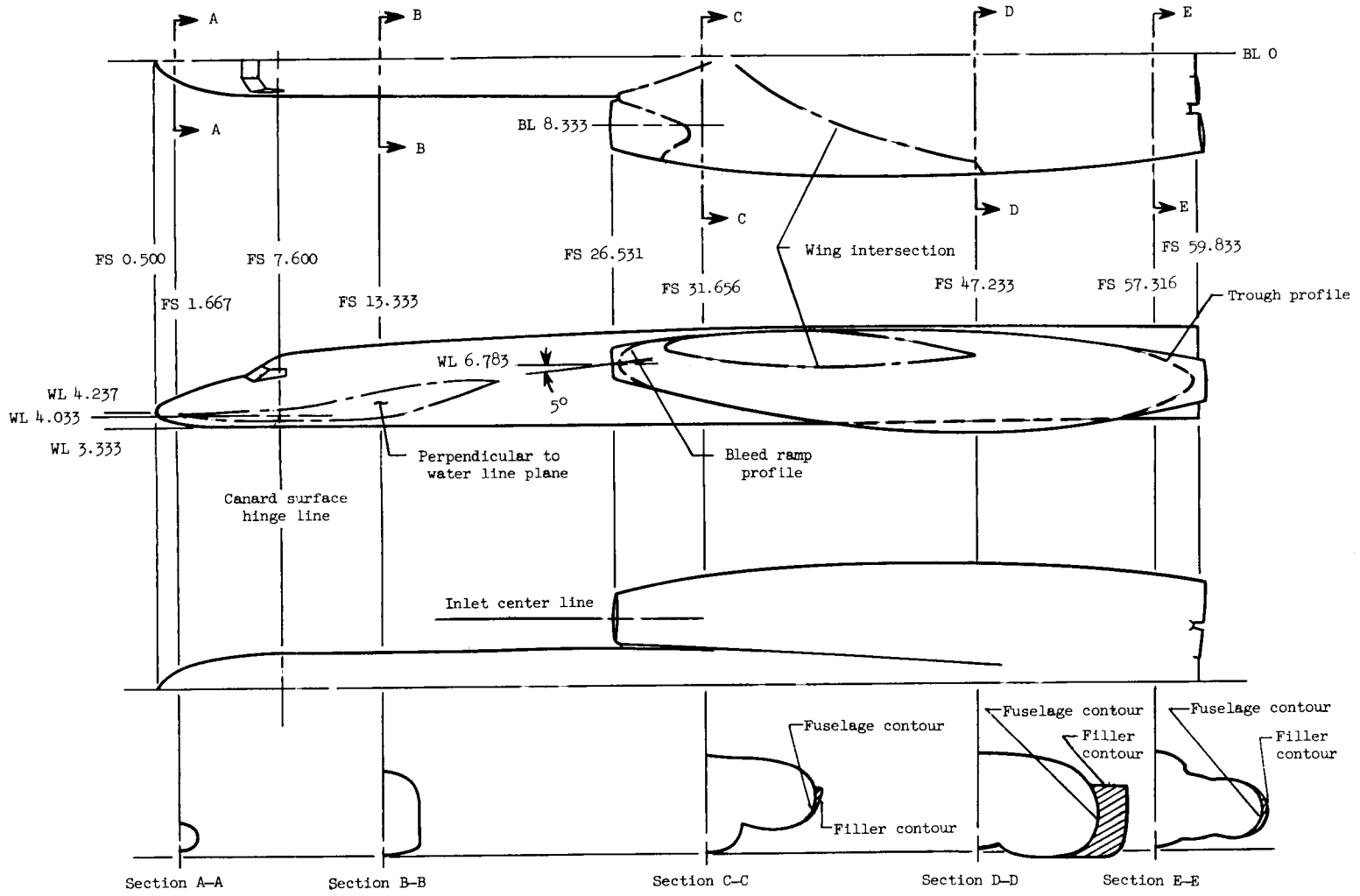

Figure 4.- External geometry of fuselage, nacelle, and filler. All dimensions in inches unless otherwise noted.

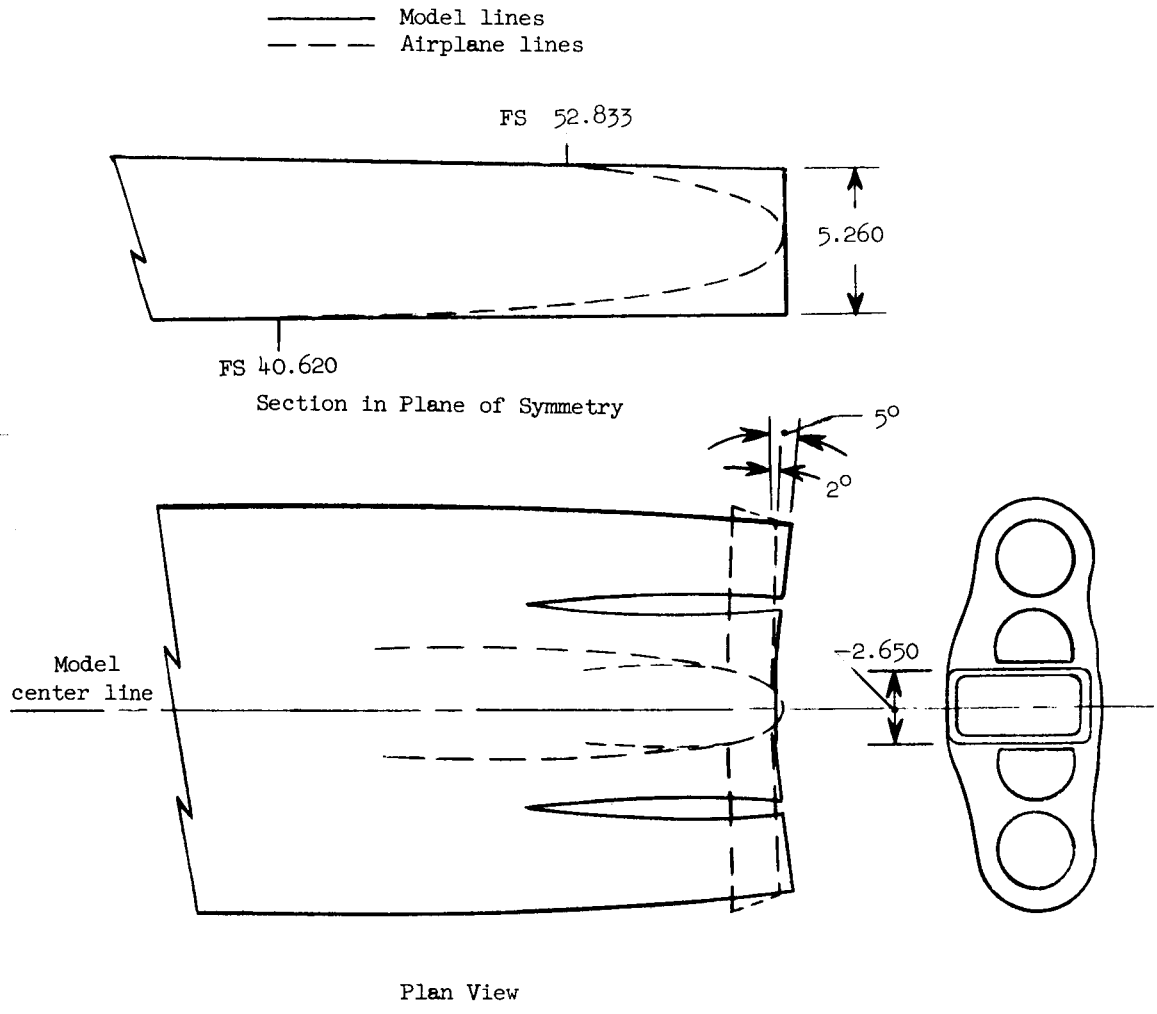

Figure 5.- Sketch showing differences between model and airplane aft ends. All dimensions in inches unless otherwise noted.

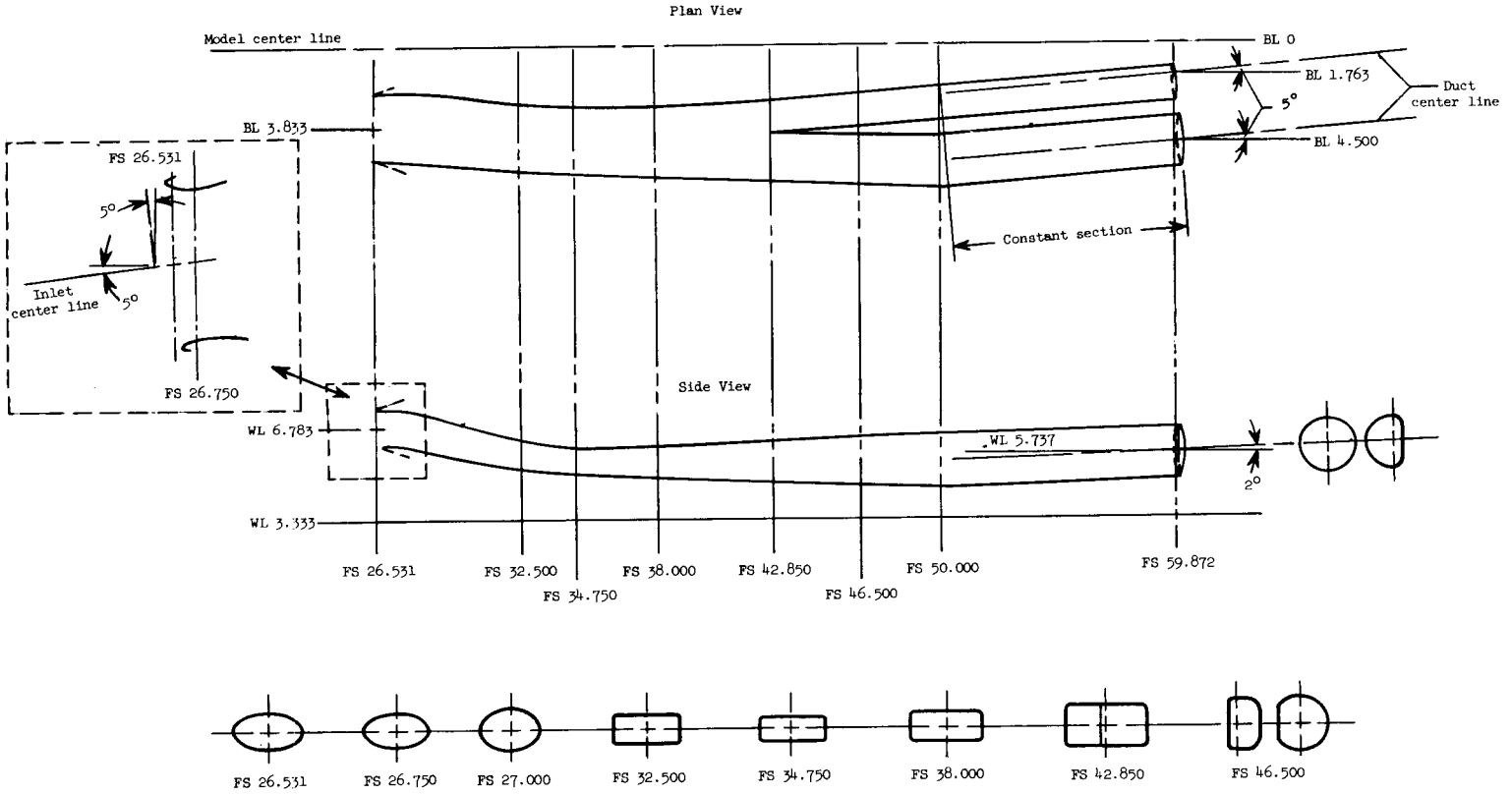

Figure 6.- Sketch of nacelle ducting. All dimensions in inches unless otherwise noted.

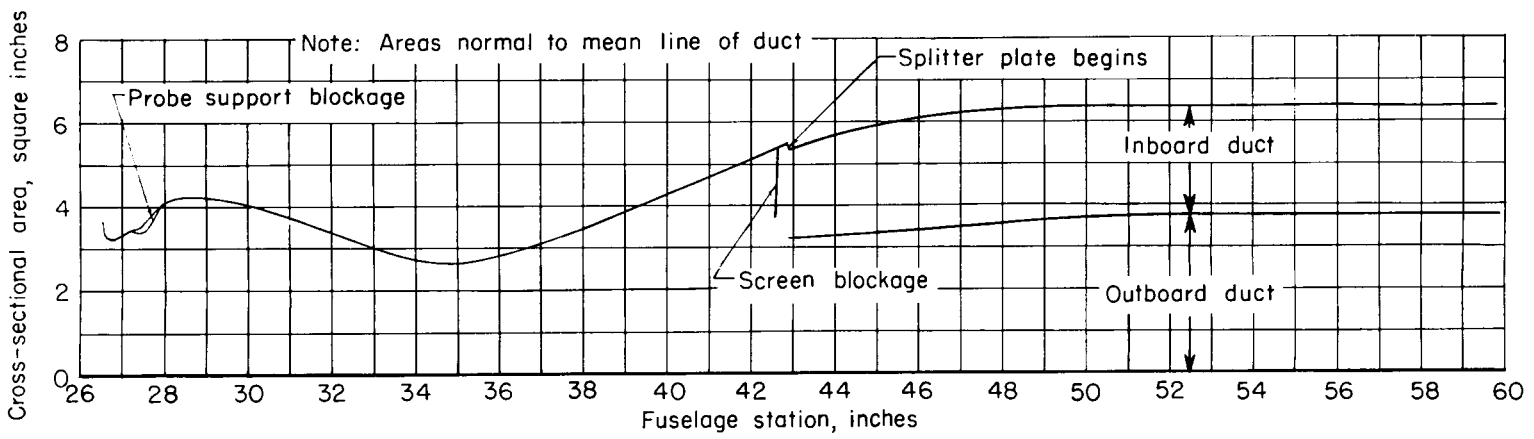

Figure 7.- Cross-sectional area distribution of nacelle ducting.

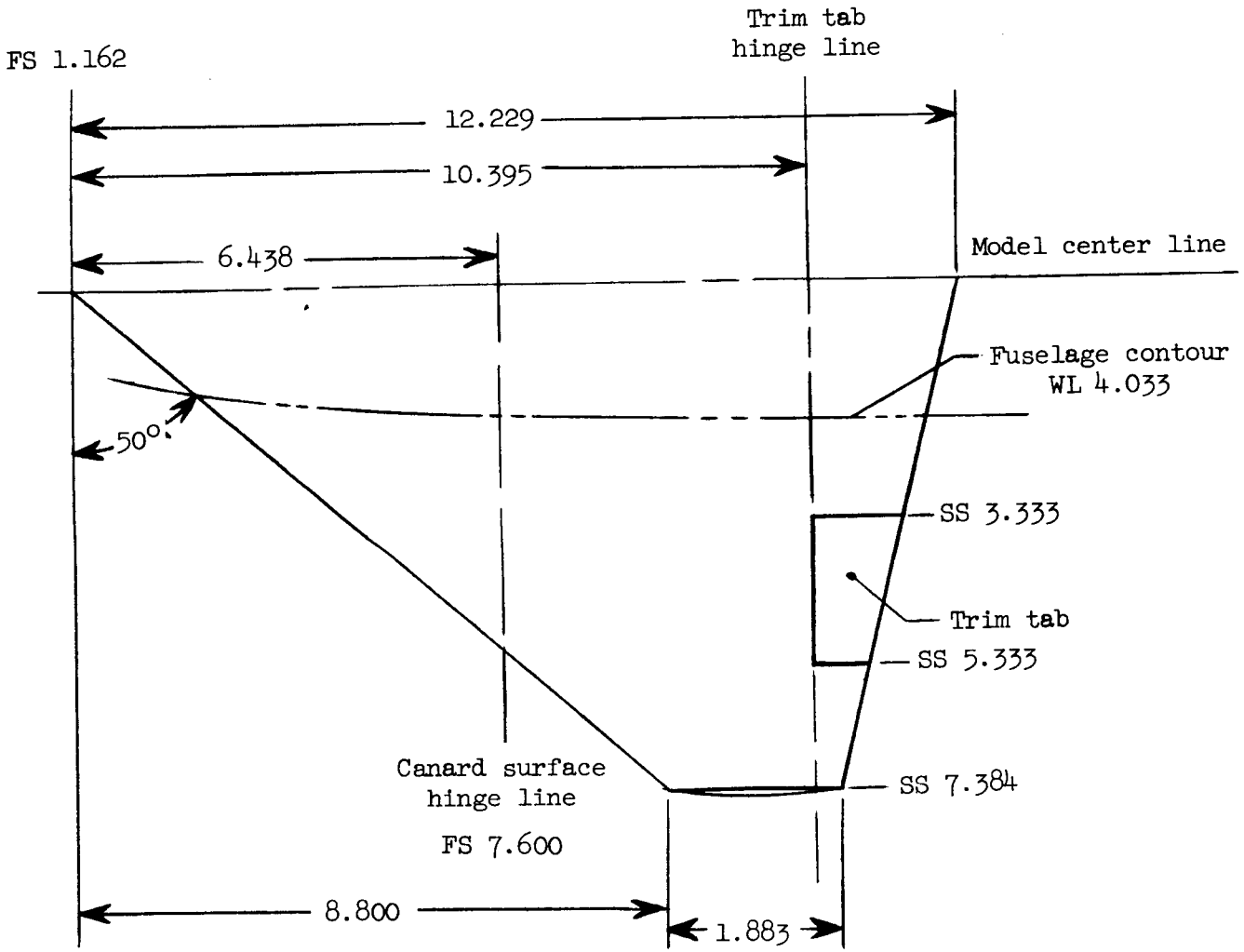

Figure 8.- Sketch of canard planform. All dimensions in inches unless otherwise noted.

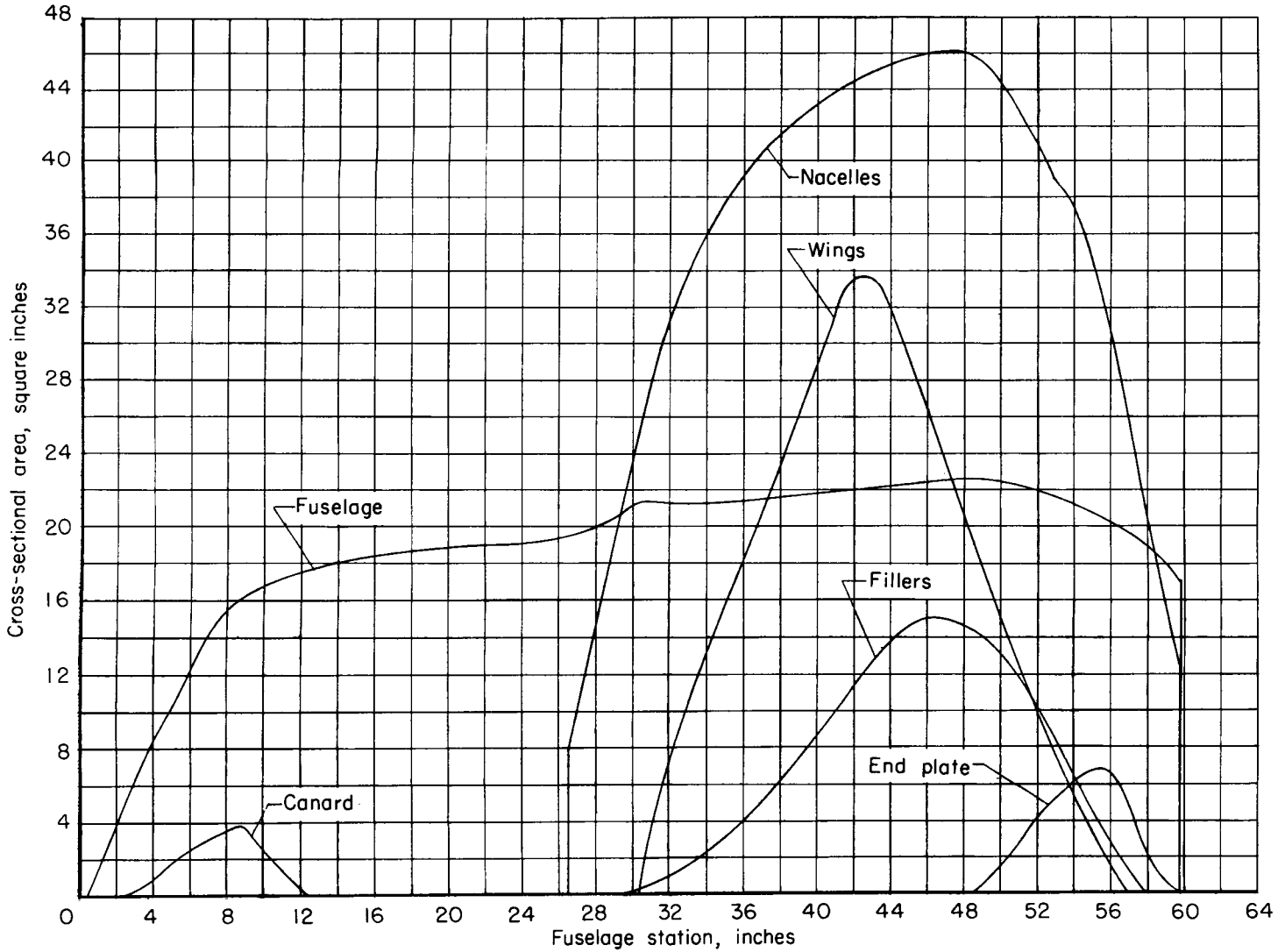

Figure 9.- Cross-sectional area distributions of model components.

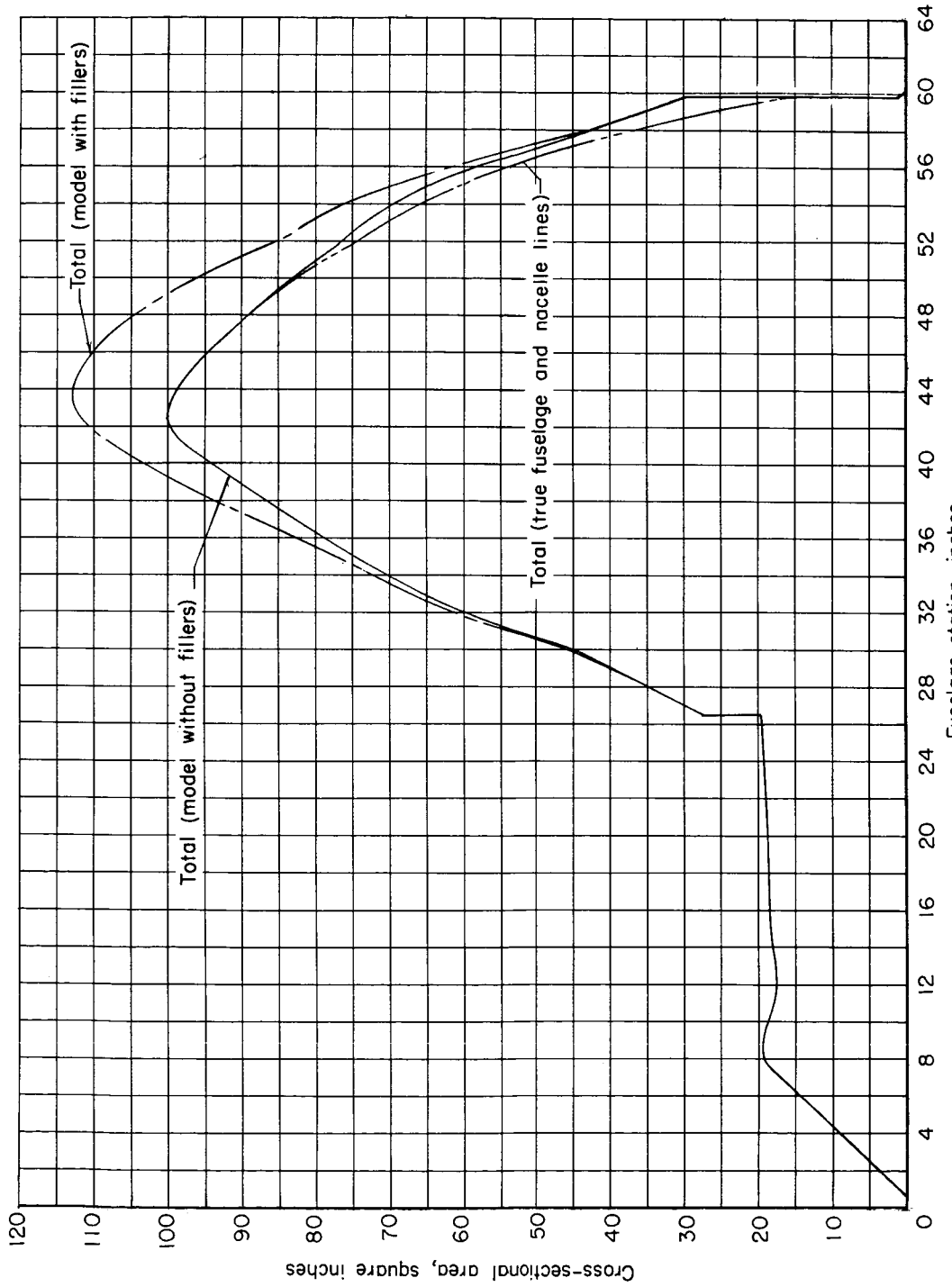

Figure 10.- Cross-sectional area distributions.

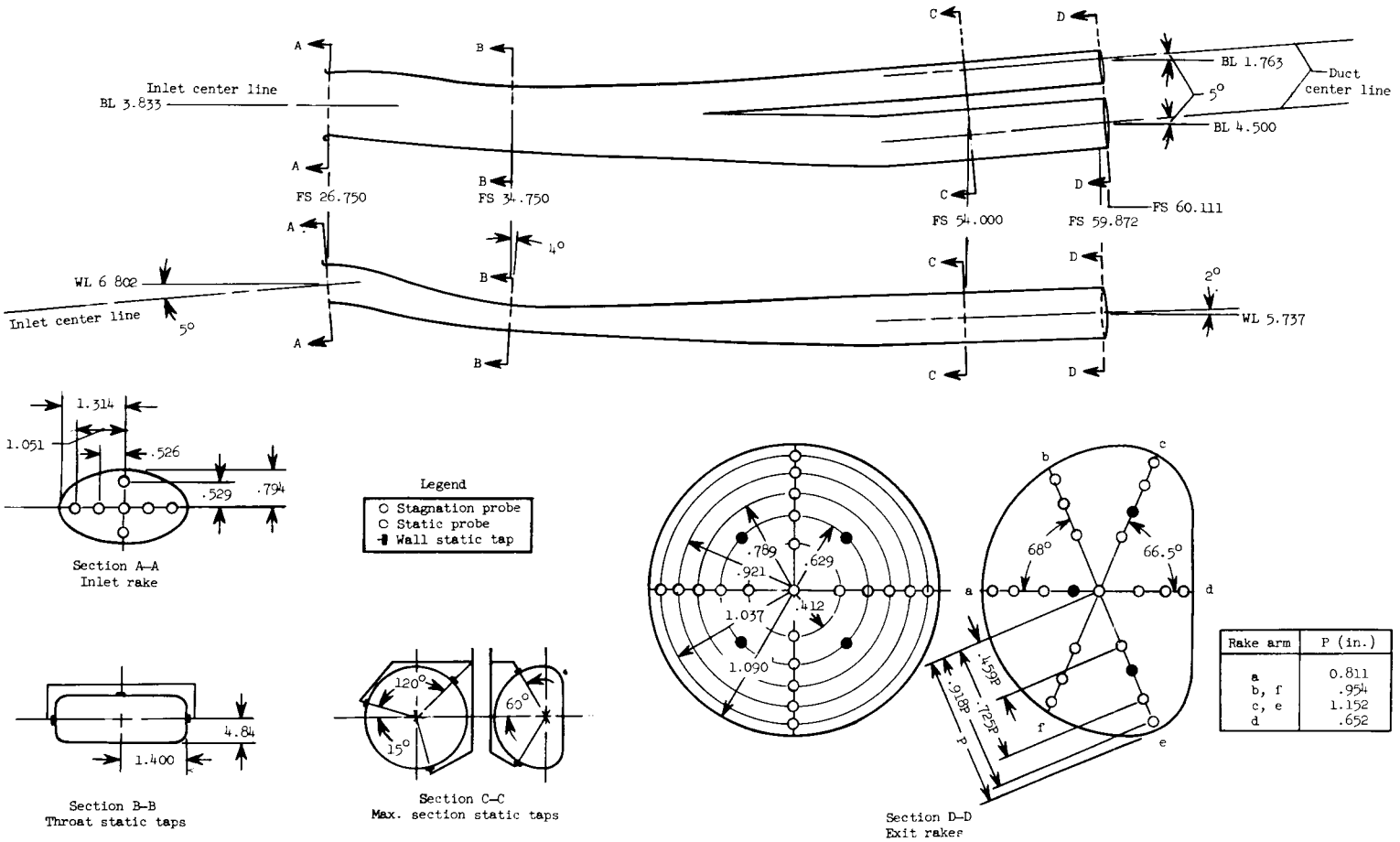

Figure 11.- Details of nacelle duct pressure instrumentation. All dimensions in inches unless otherwise noted.

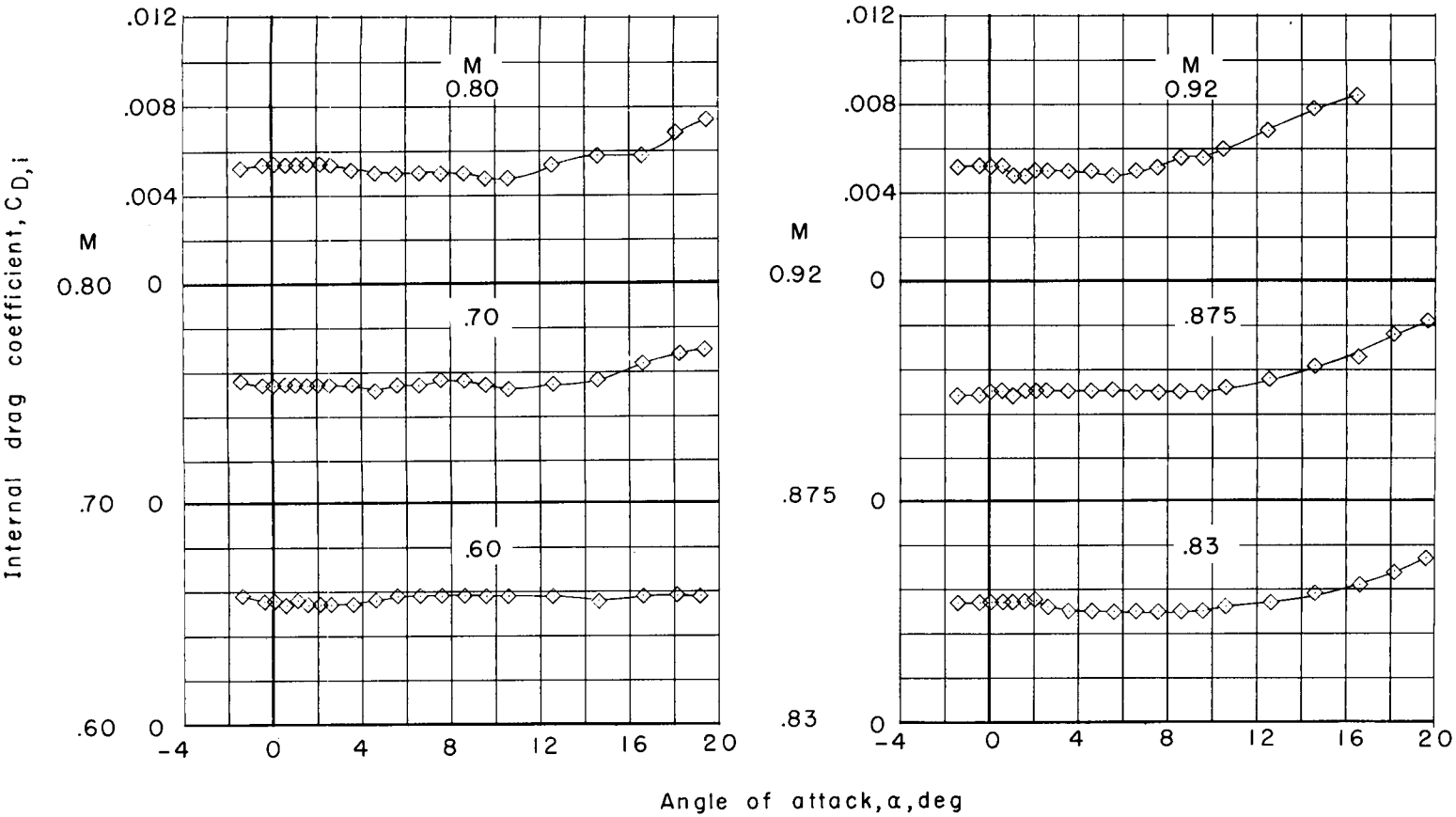

(a) Model BWE with $\delta_{le} = 12^{o}$.

Figure 12.- Variation of nacelle internal-drag coefficient with angle of attack.

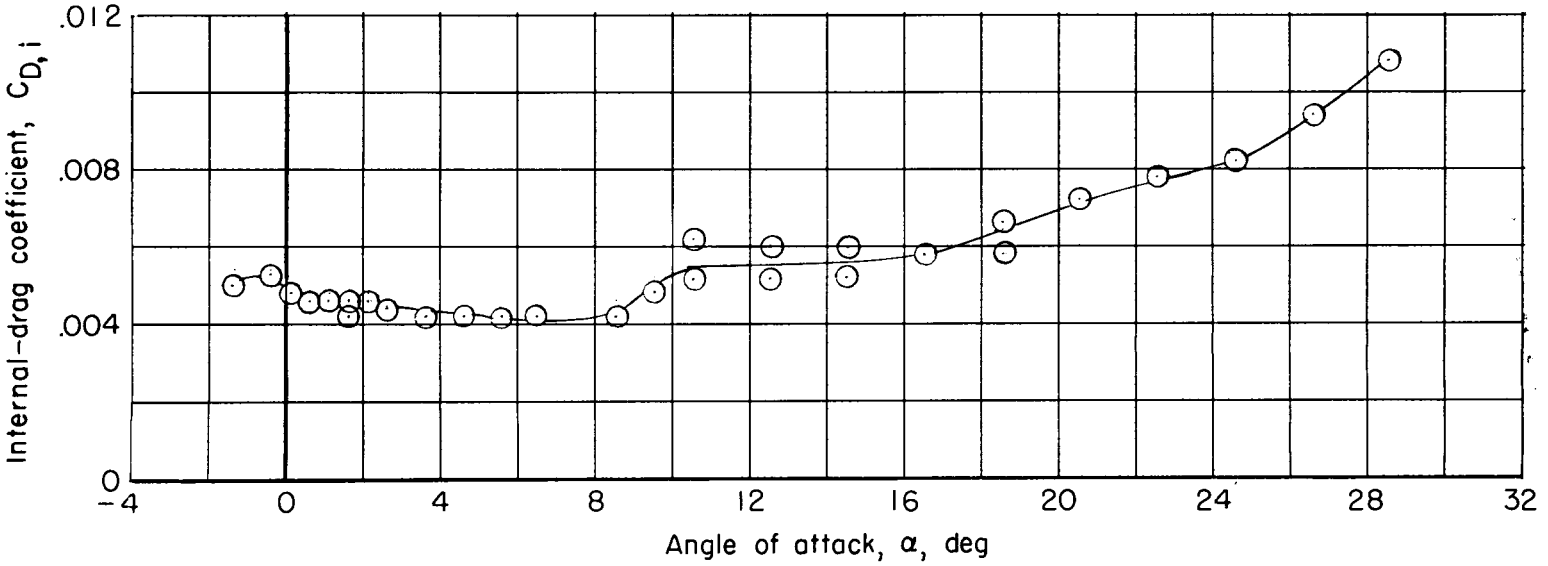

(b) Model BWE with $\delta_{le} = 25^{\circ}$ at $M = 0.30$.

Figure 12.- Continued.

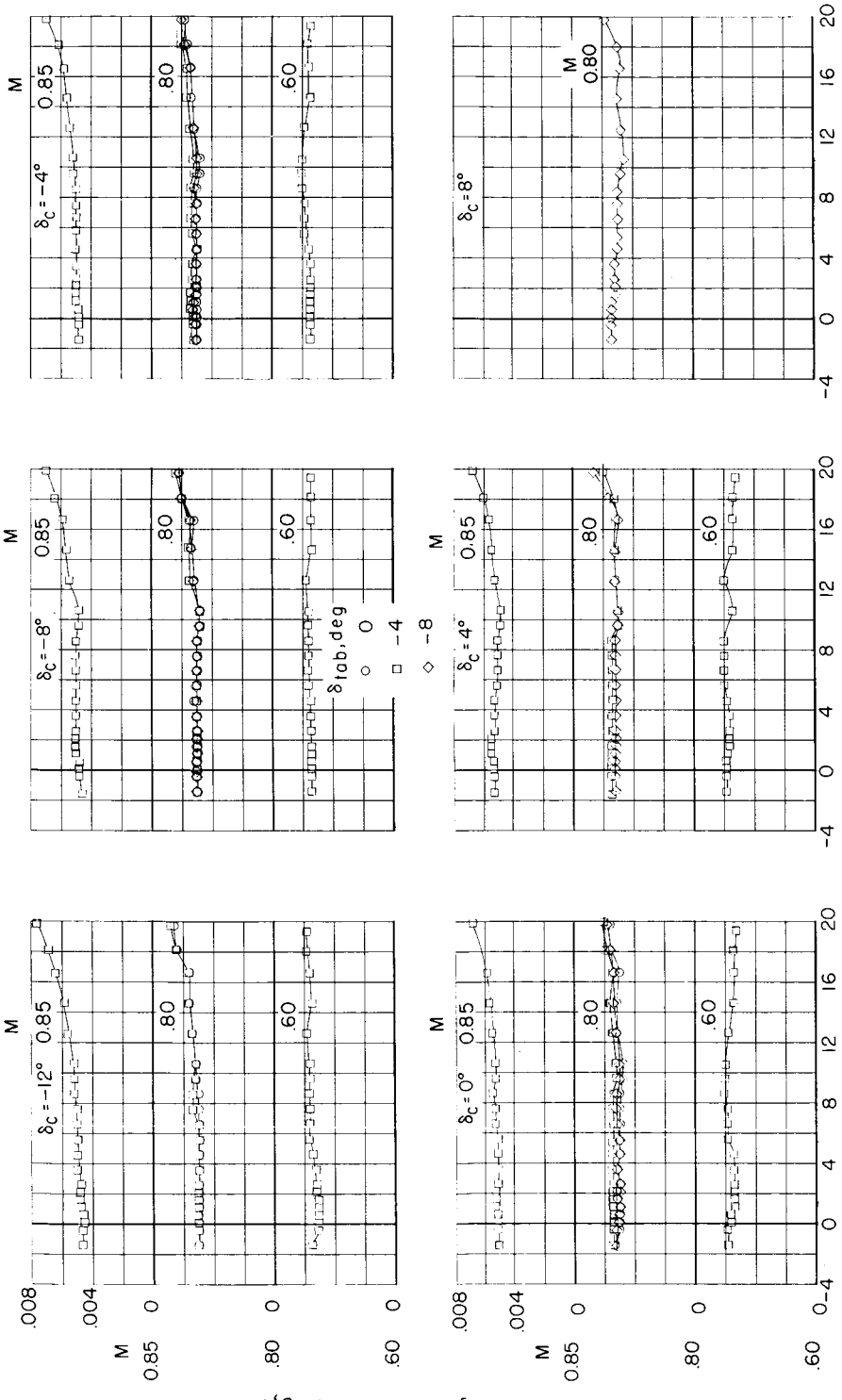

(c) Model BCWE with $\delta_{le} = 12°$.

Figure 12.- Concluded.

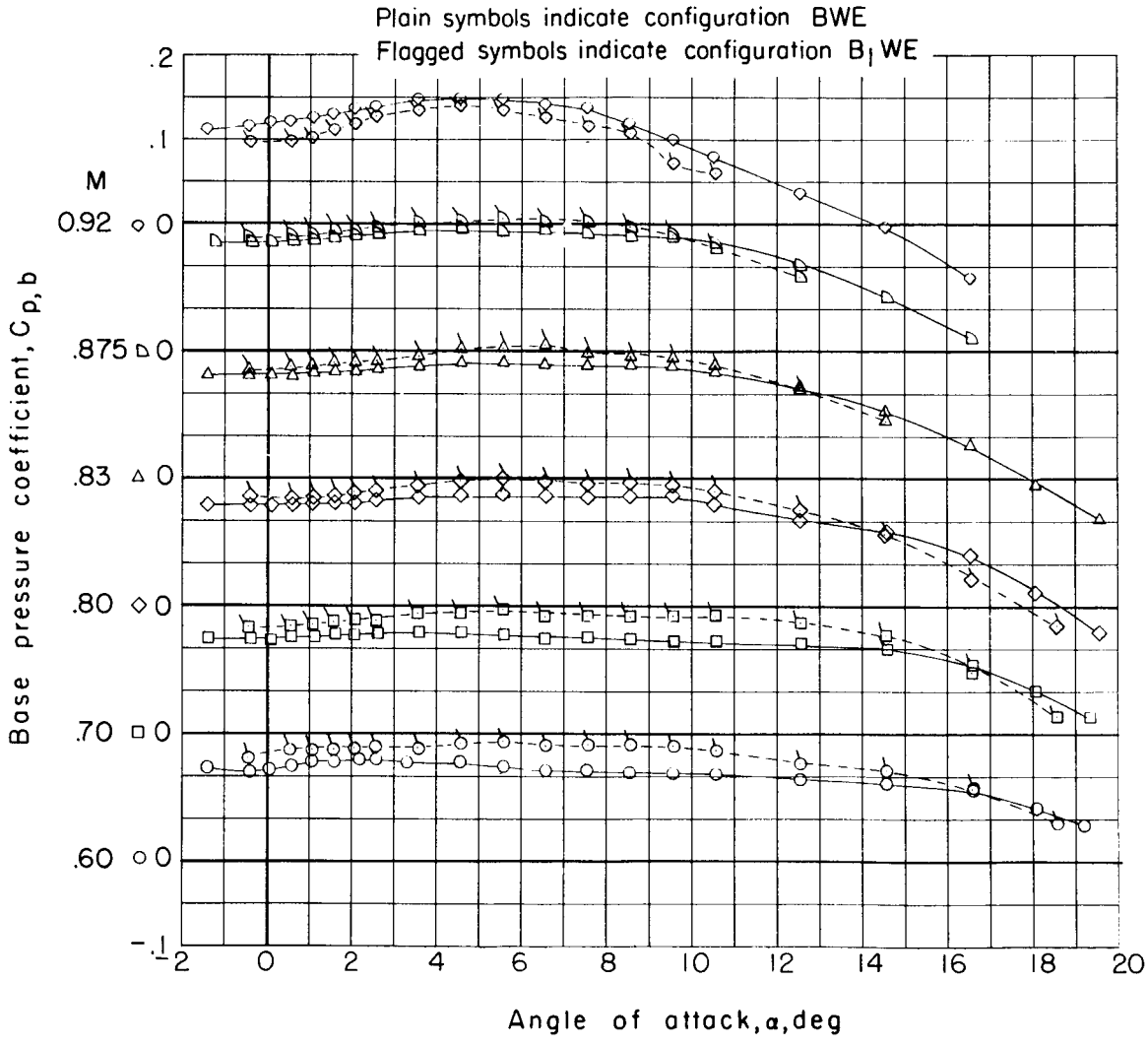

(a) Models BWE and B_1WE with $\delta_{le} = 12^\circ$.

Figure 13.- Variation of base pressure coefficient with angle of attack.

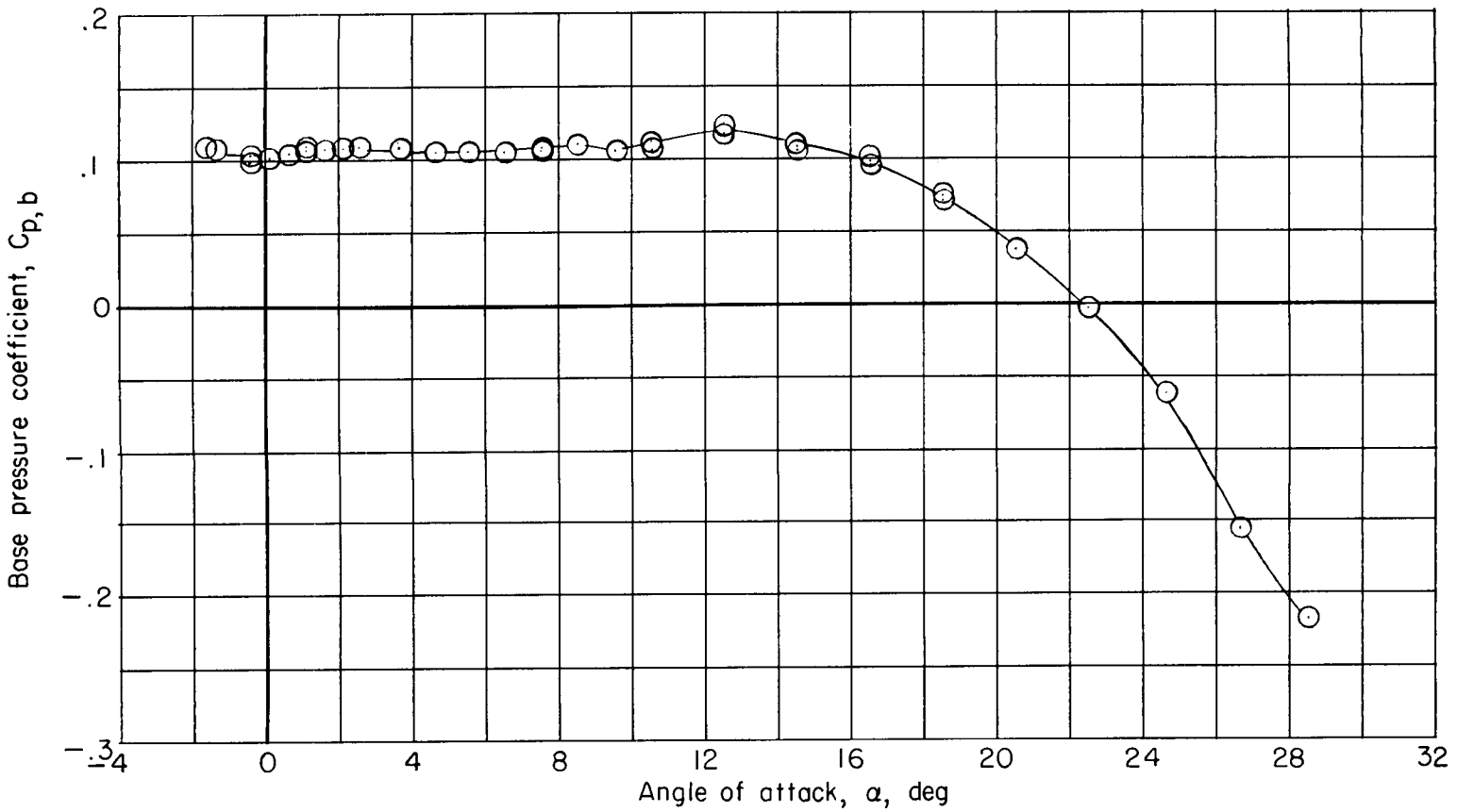

(b) Model BWE with $\delta_{le} = 25^{\circ}$ at M = 0.30.

Figure 13.- Concluded.

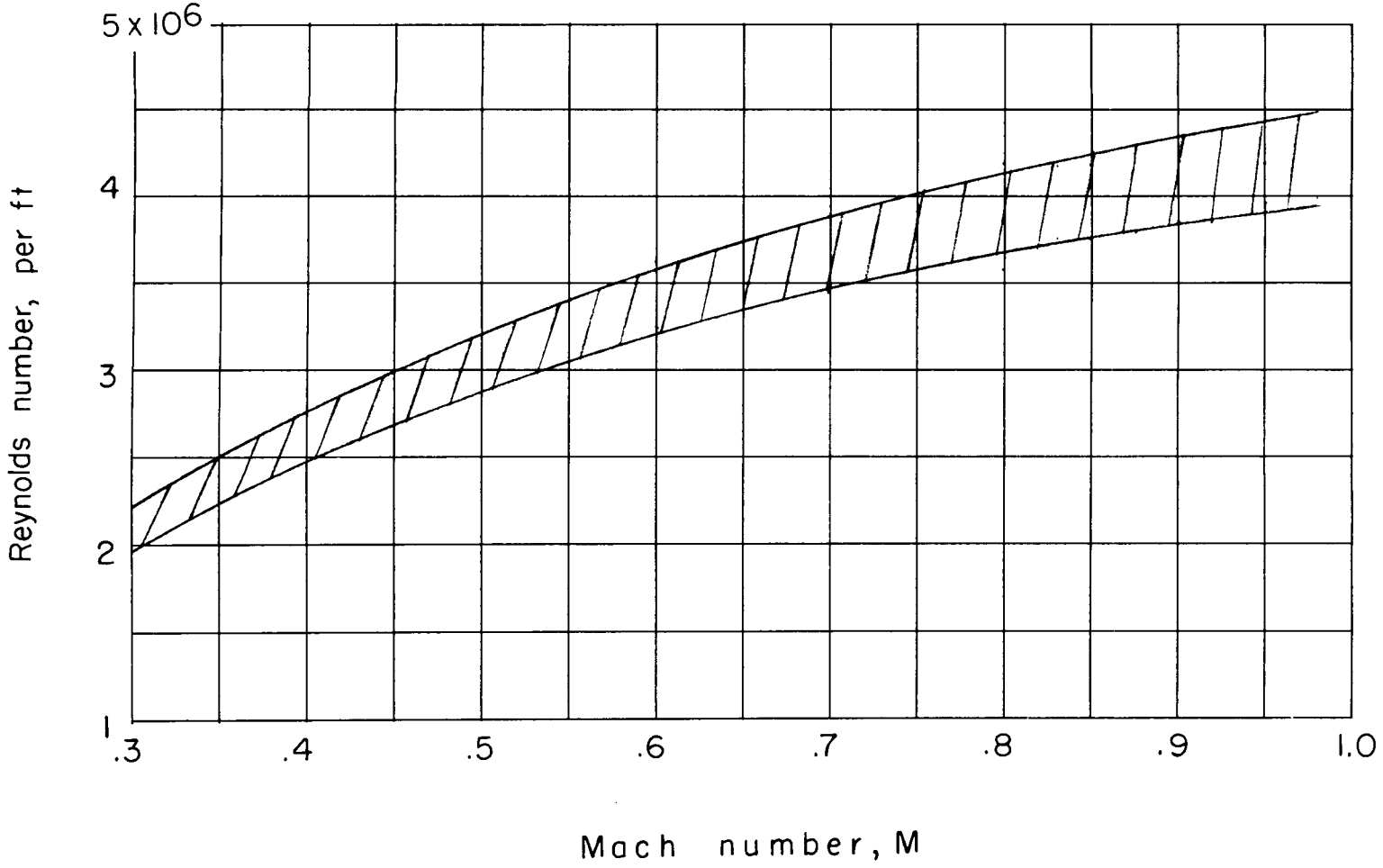

Figure 14.- Variation of Reynolds number (per foot) with Mach number for Langley 16-foot transonic tunnel.

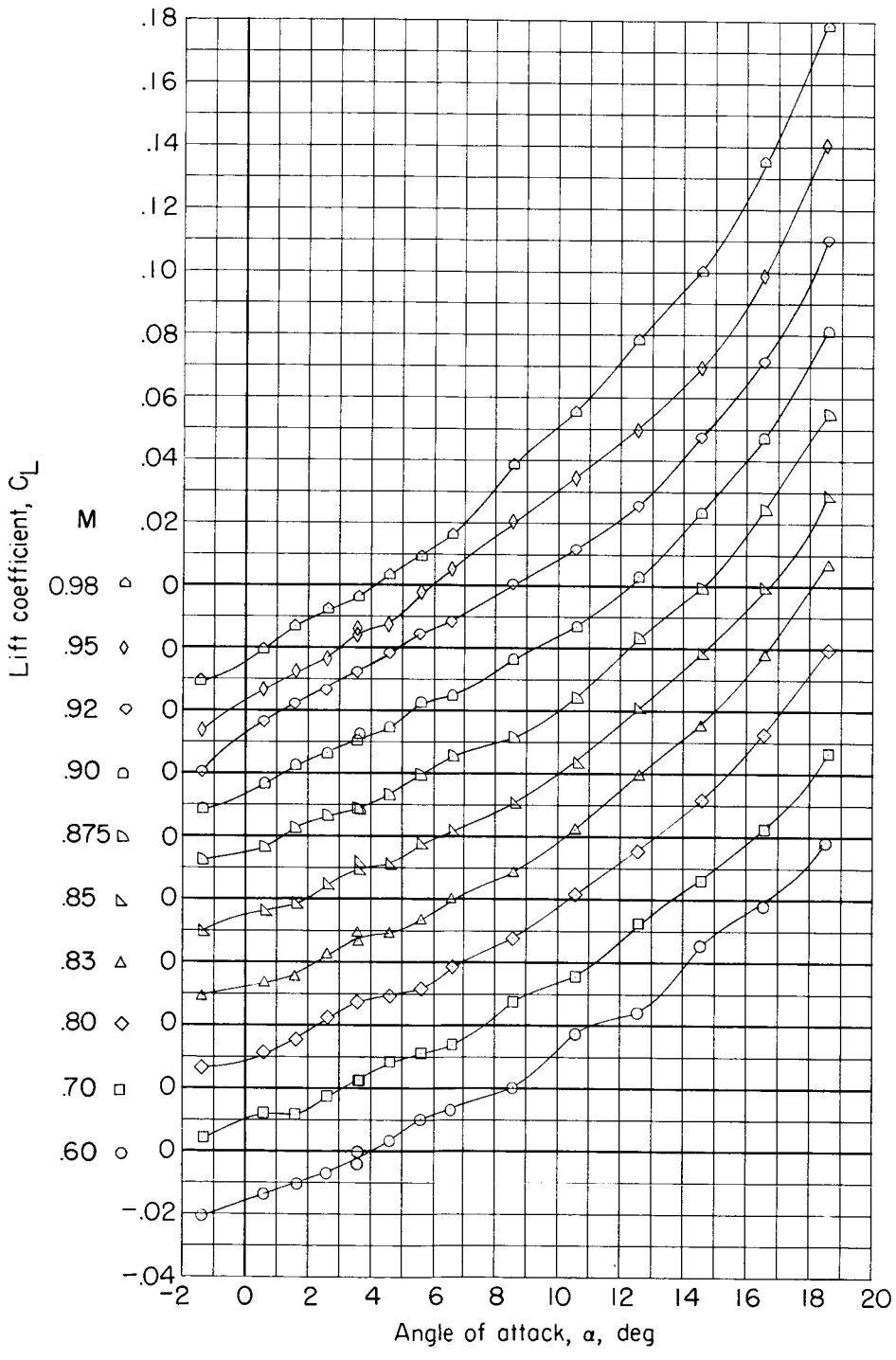

(a) Lift coefficient.

Figure 15.- Aerodynamic characteristics for configuration B.

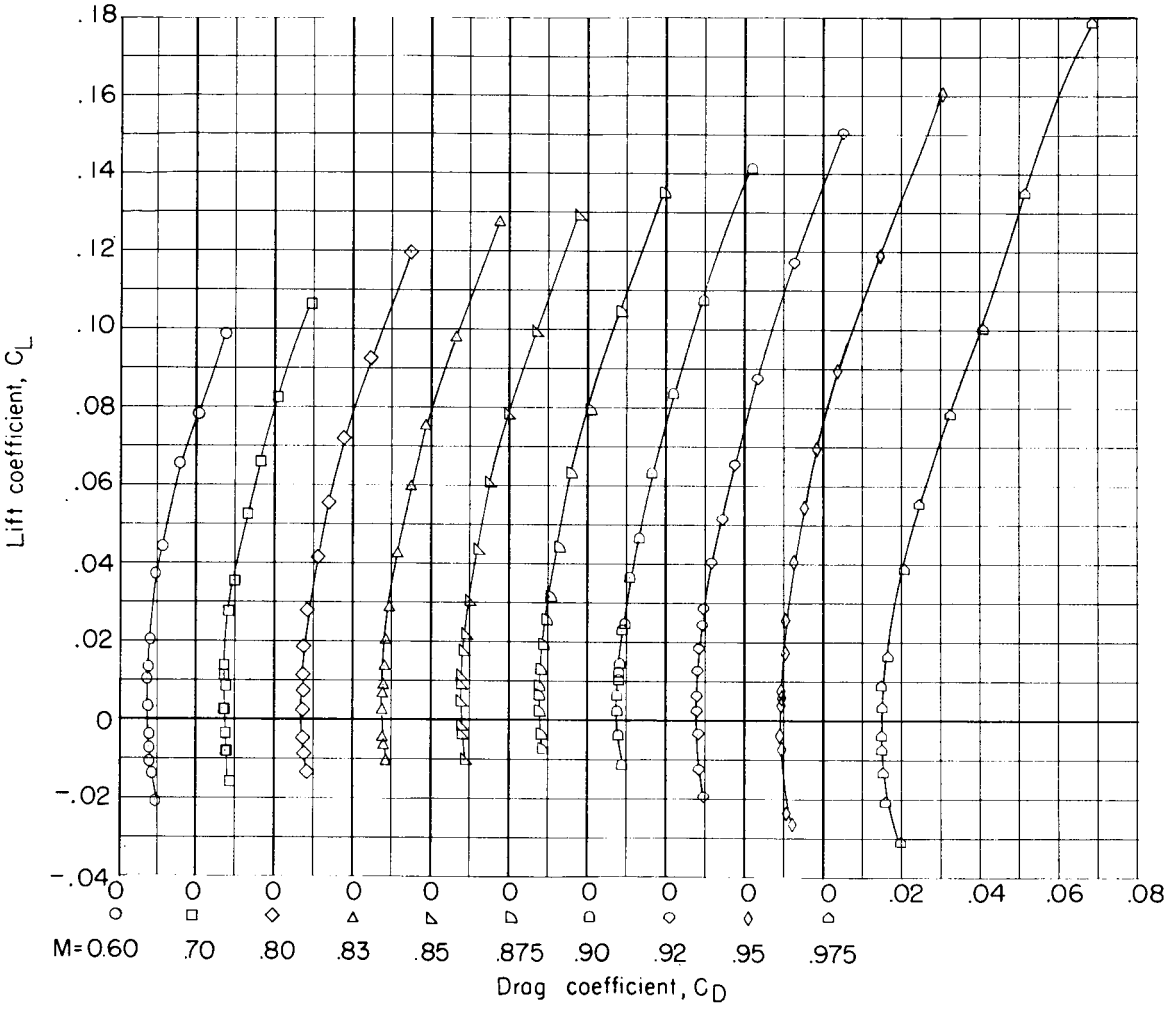

(b) Drag coefficient.

Figure 15.- Continued.

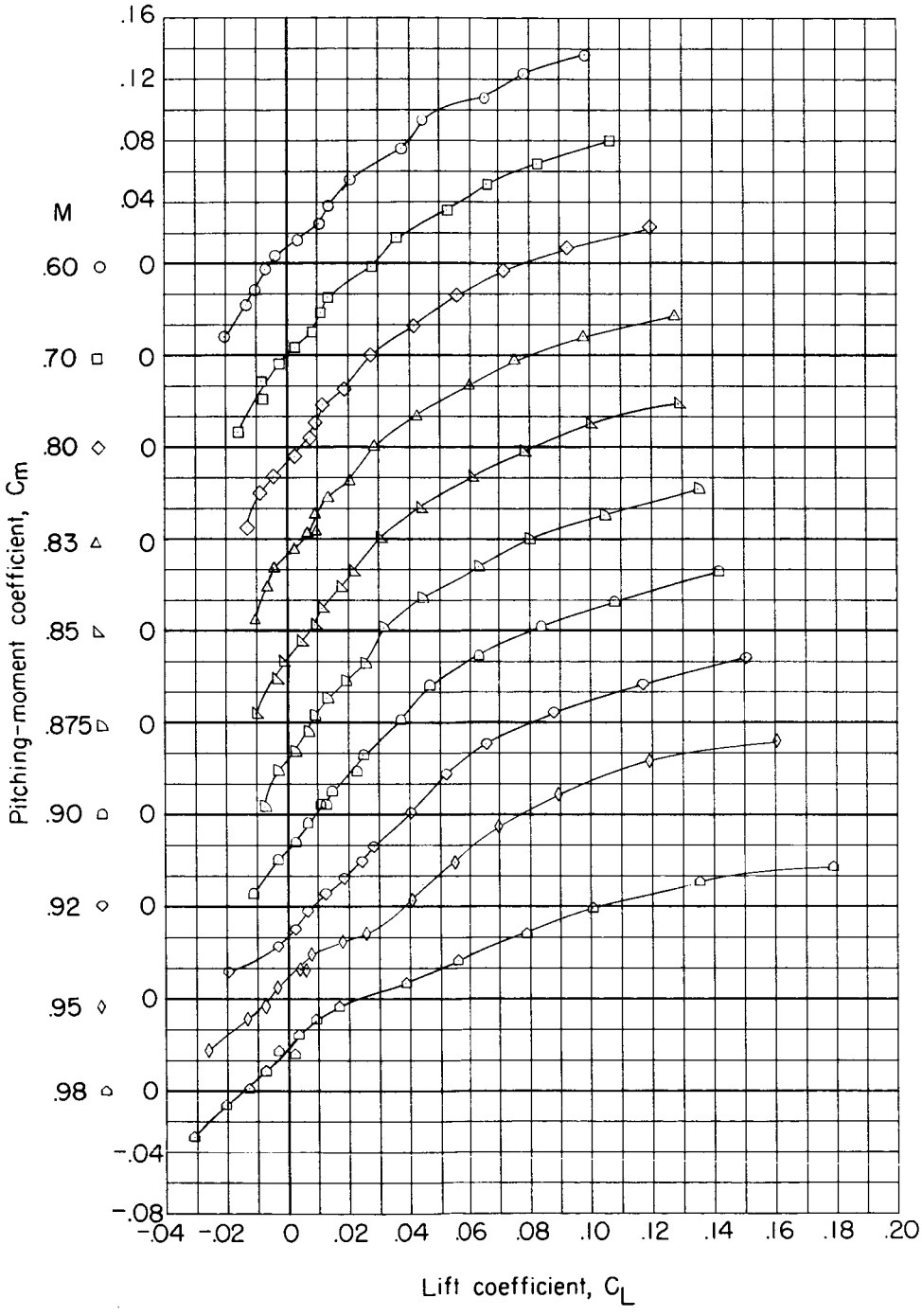

(c) Pitching-moment coefficient.

Figure 15.- Concluded.

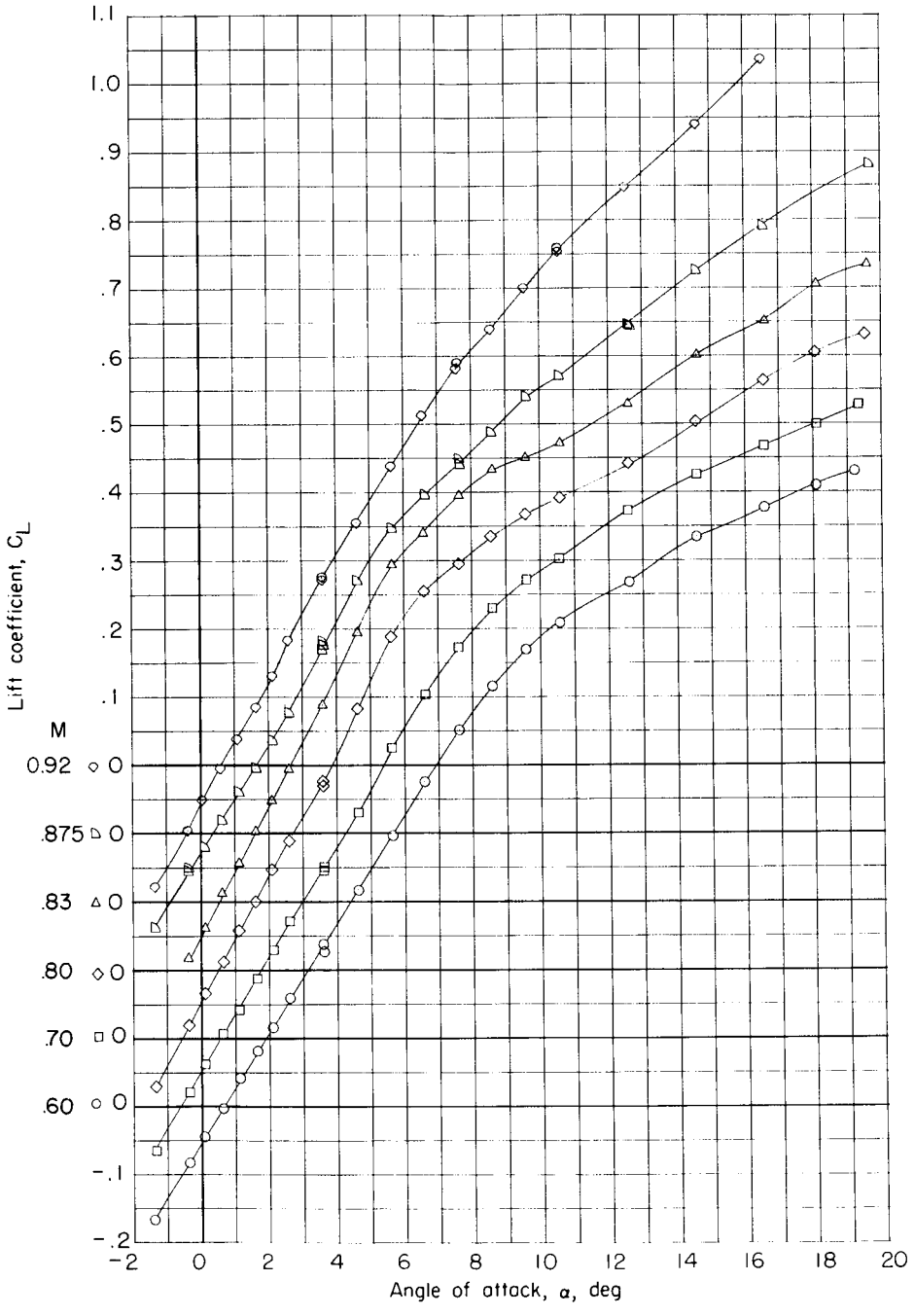

(a) Lift coefficient.

Figure 16.- Aerodynamic characteristics for configuration BW with $\delta_{le} = 12^{o}$.

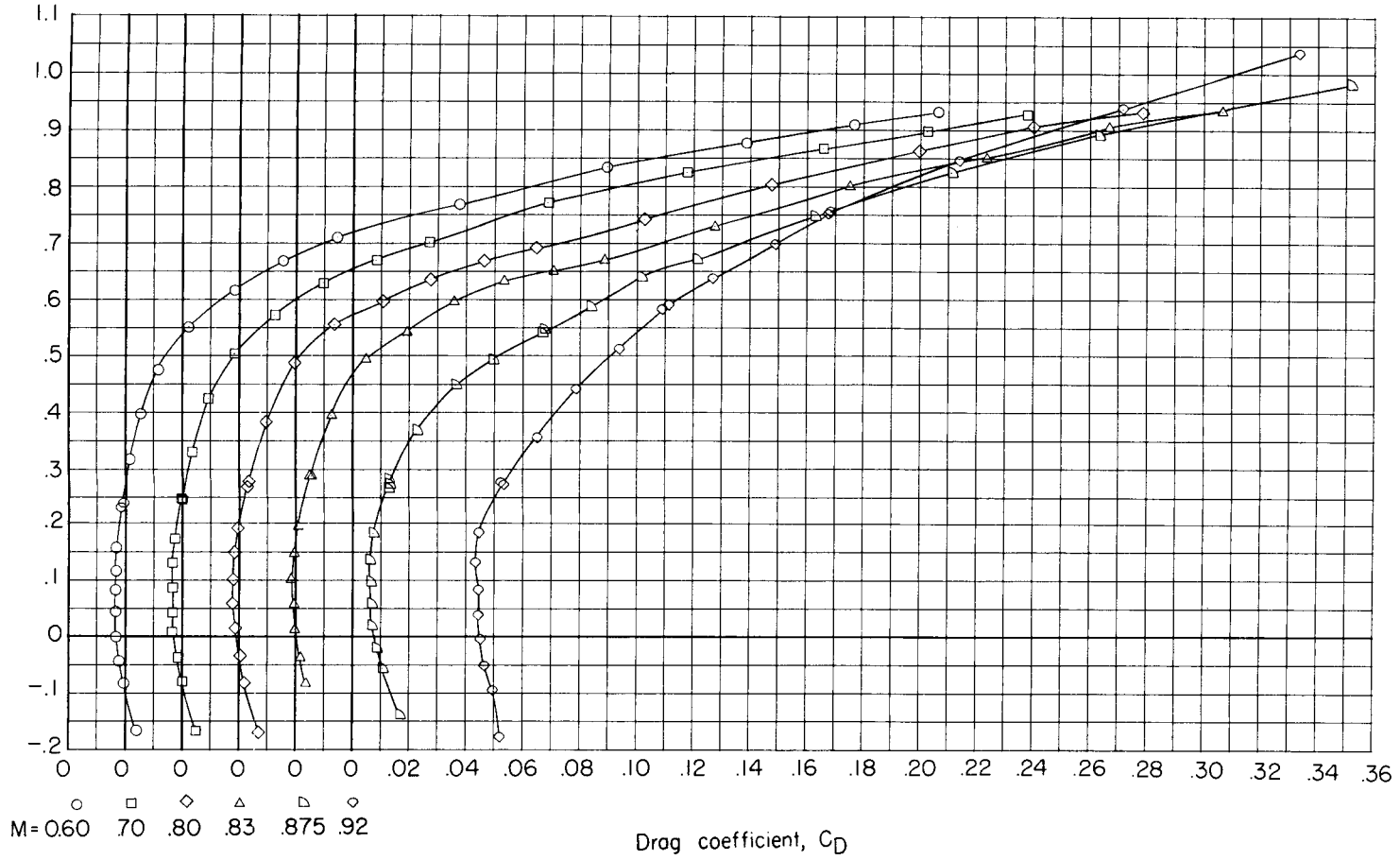

(b) Drag coefficient.

Figure 16.- Continued.

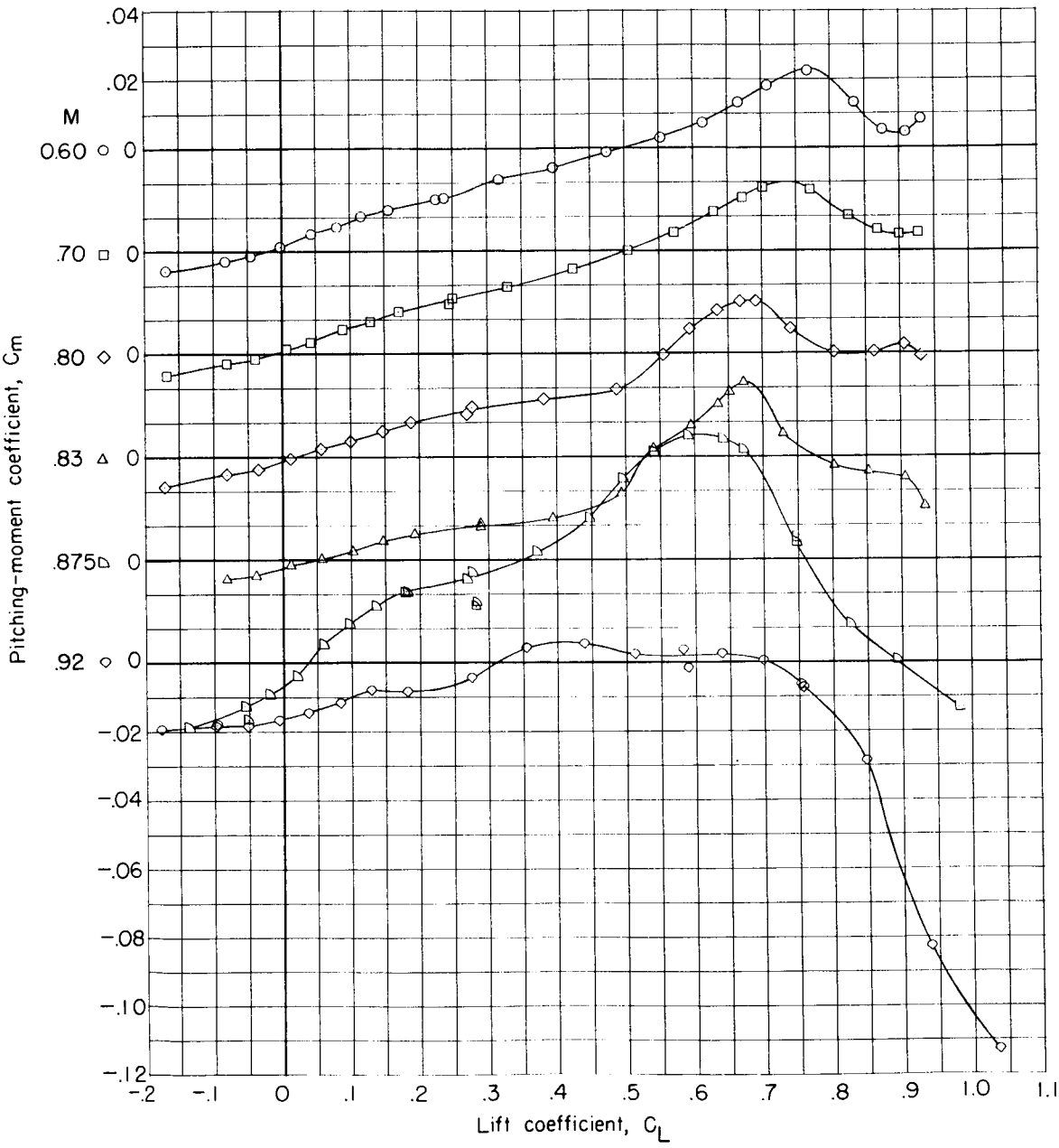

(c) Pitching-moment coefficient.

Figure 16.- Concluded.

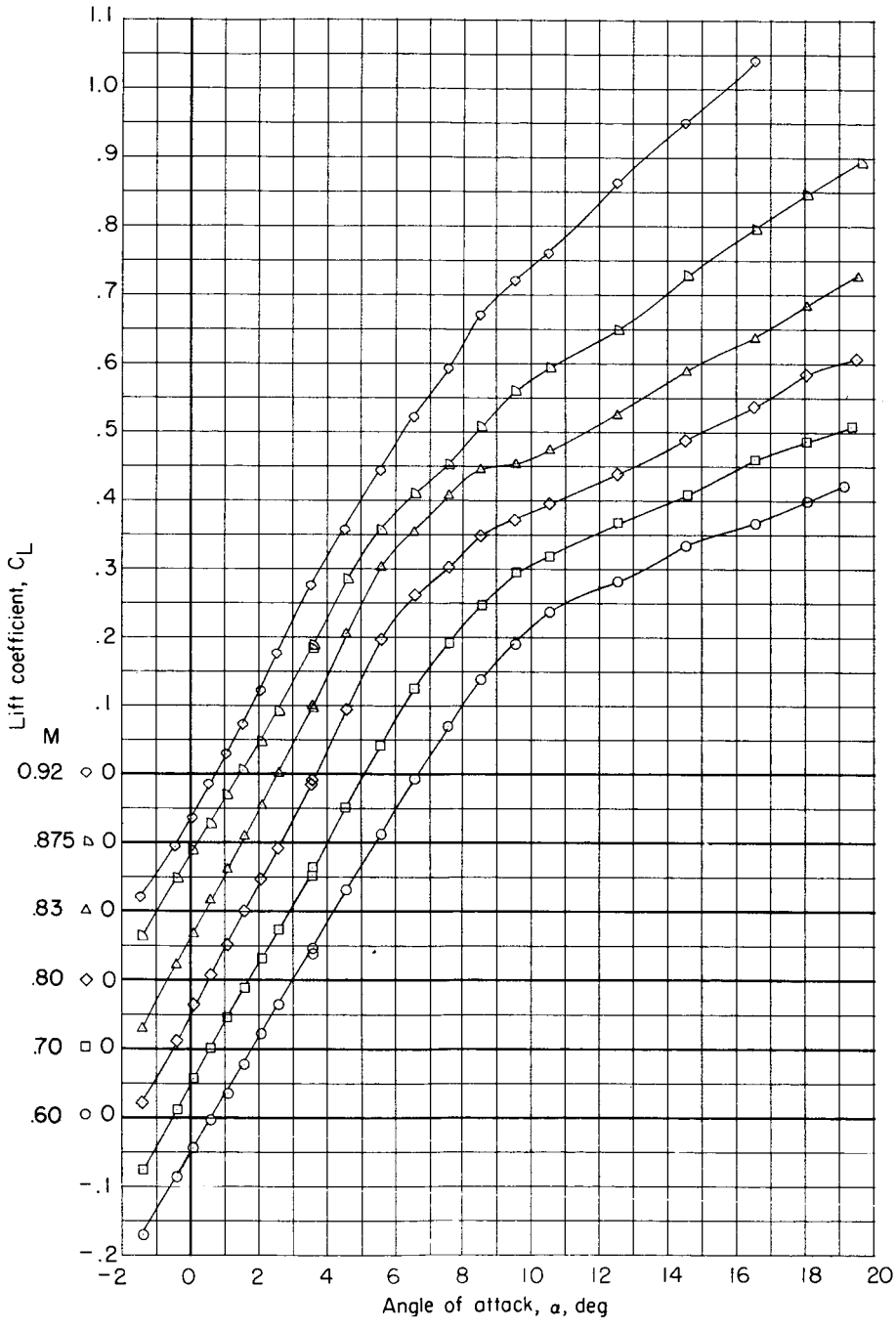

(a) Lift coefficient.

Figure 17.- Aerodynamic characteristics for configuration BWE with $\delta_{le} = 12^{\circ}$.

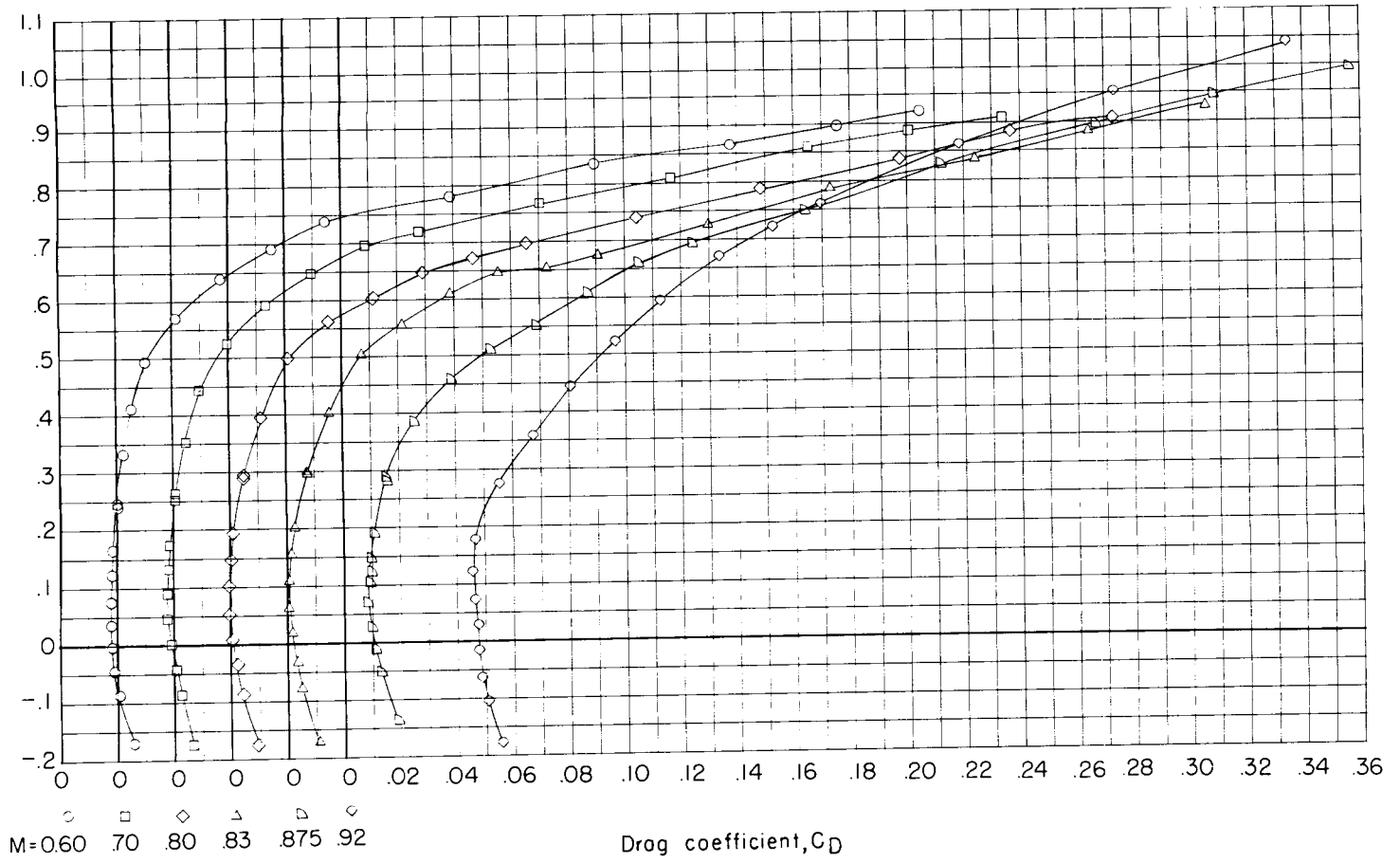

(b) Drag coefficient.

Figure 17.- Continued.

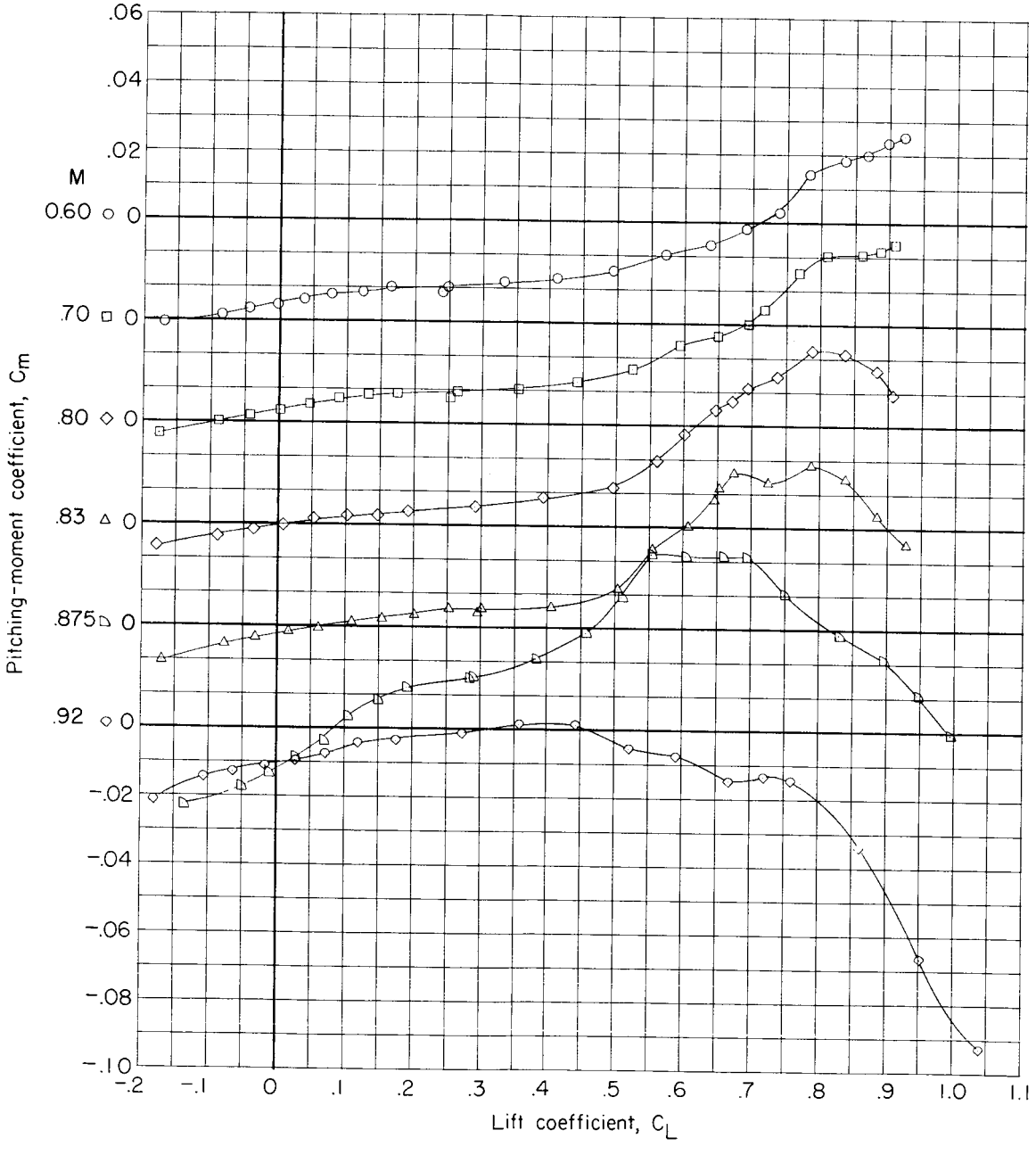

(c) Pitching-moment coefficient.

Figure 17.- Concluded.

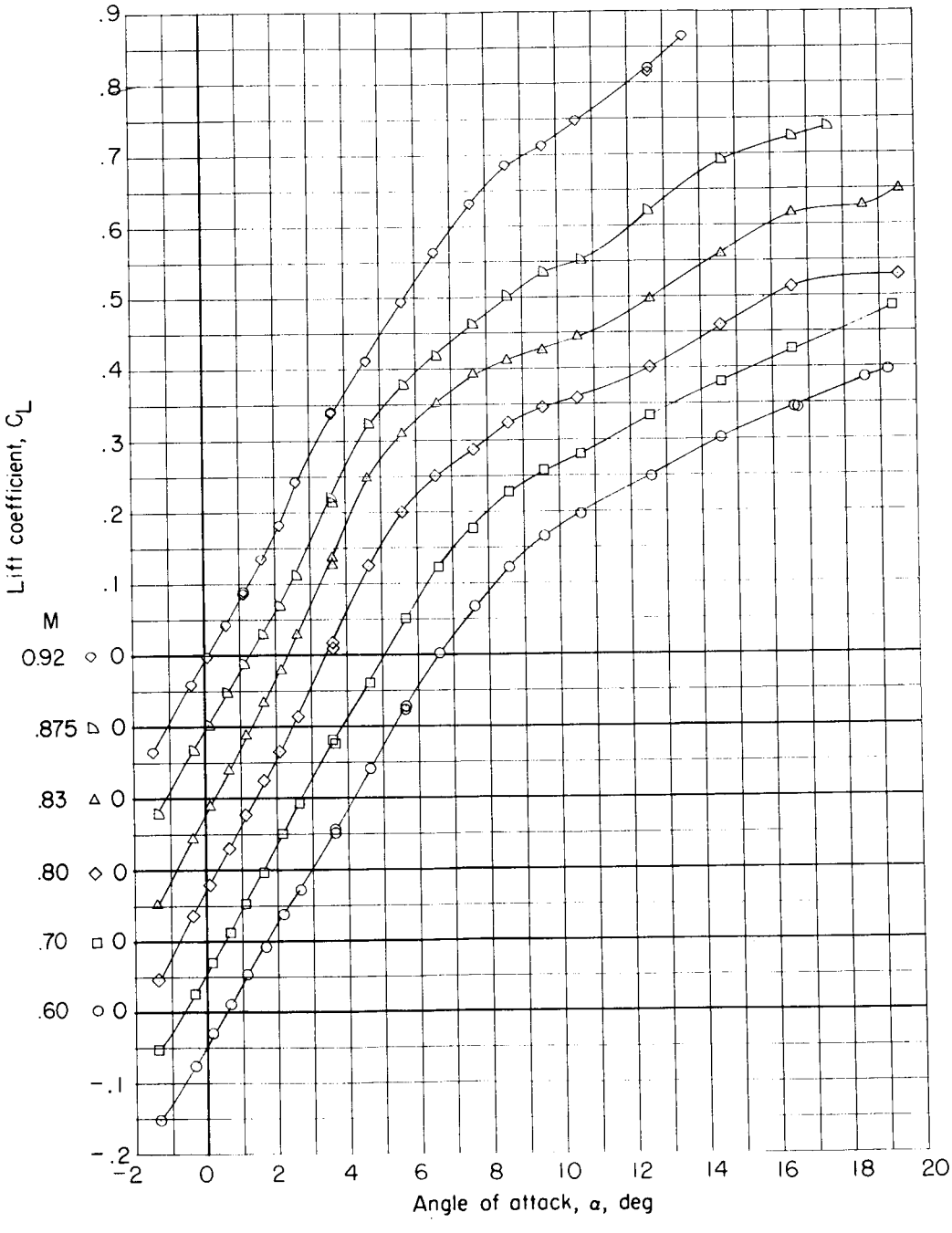

(a) Lift coefficient.

Figure 18.- Aerodynamic characteristics for configuration BWE with $\delta_{le} = 0^{\circ}$.

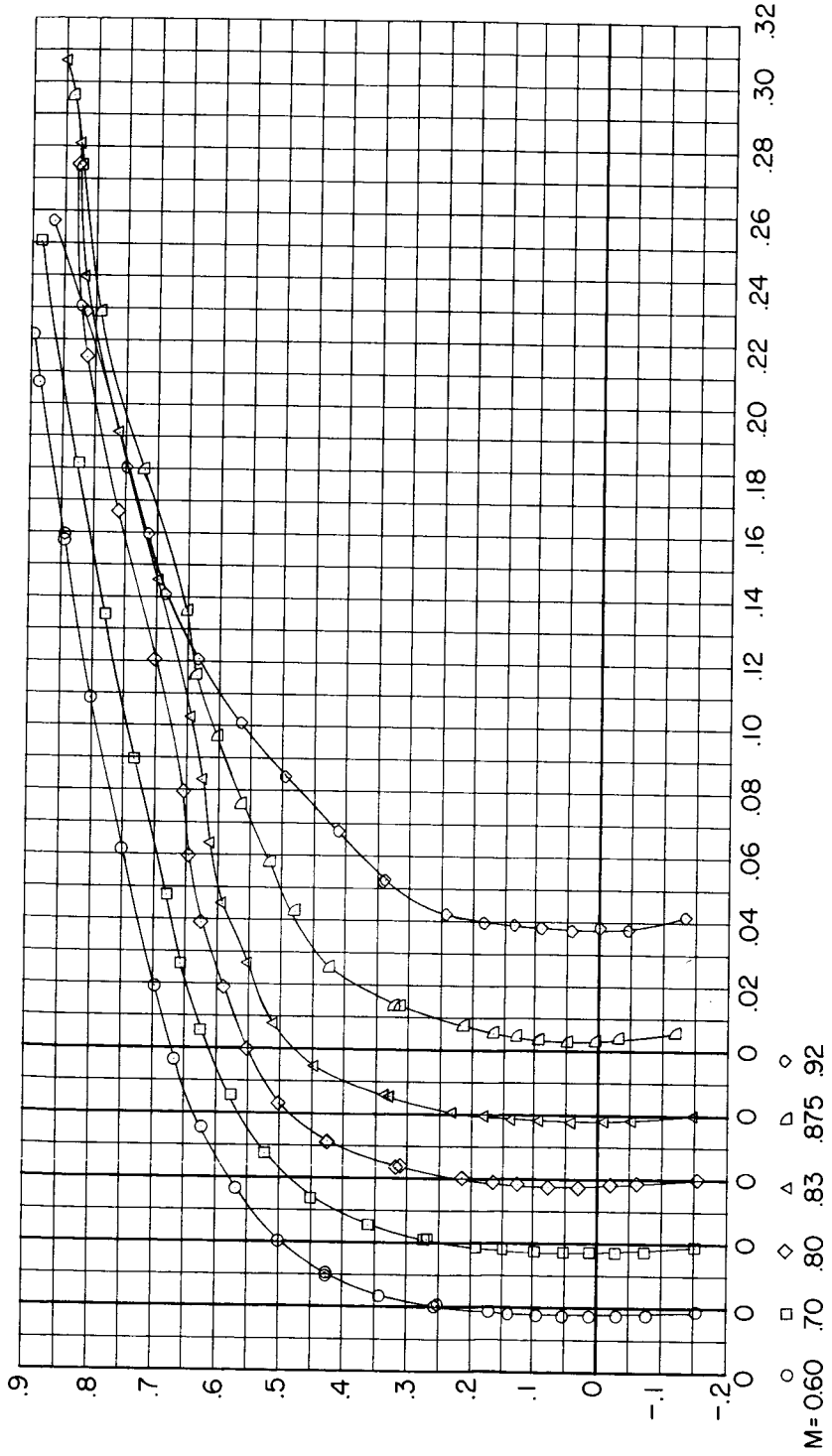

(b) Drag coefficient.

Figure 18.- Continued.

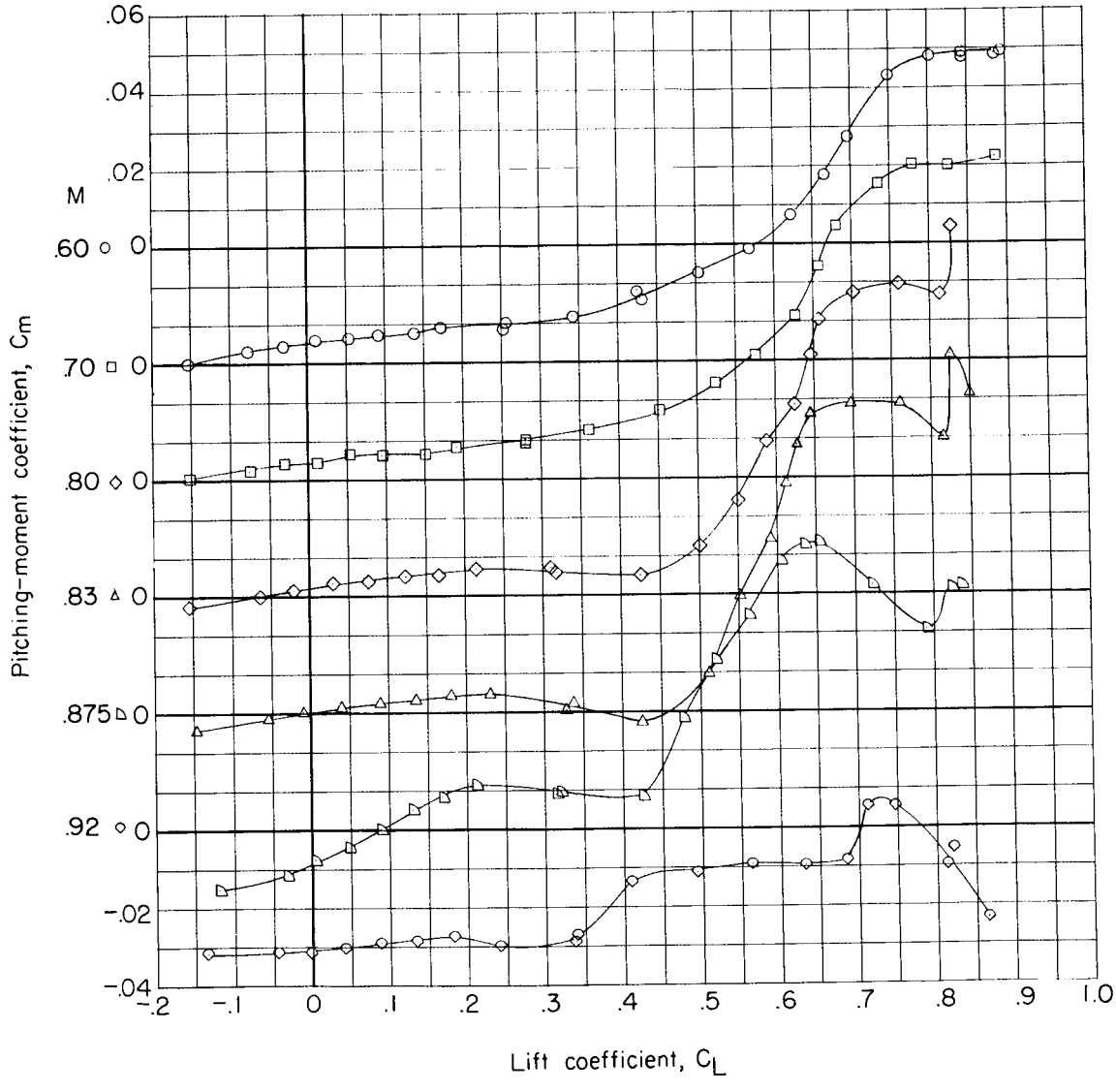

(c) Pitching-moment coefficient.

Figure 18.- Concluded.

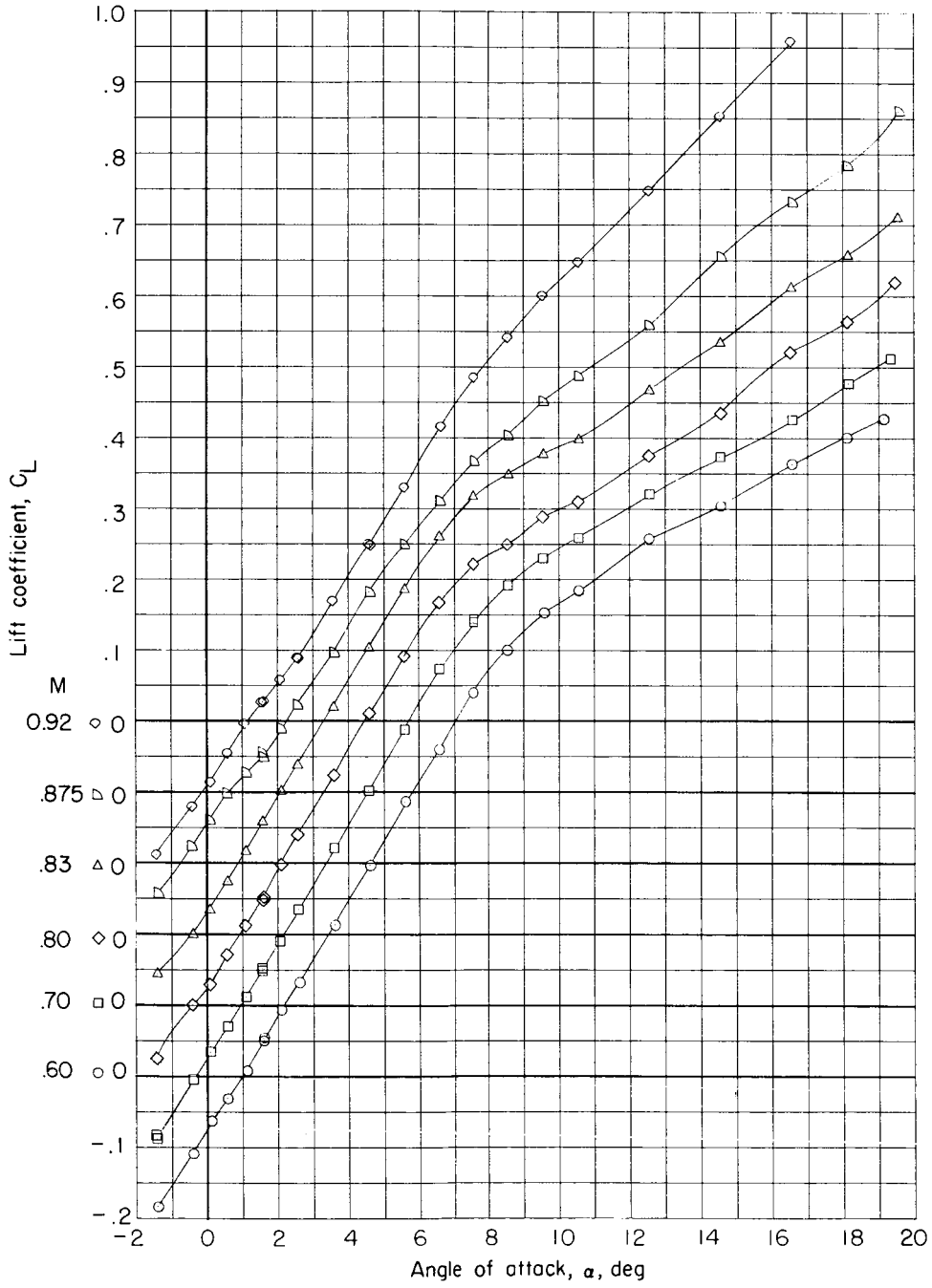

(a) Lift coefficient.

Figure 19.- Aerodynamic characteristics for configuration BWE with $\delta_{le} = 25^{\circ}$.

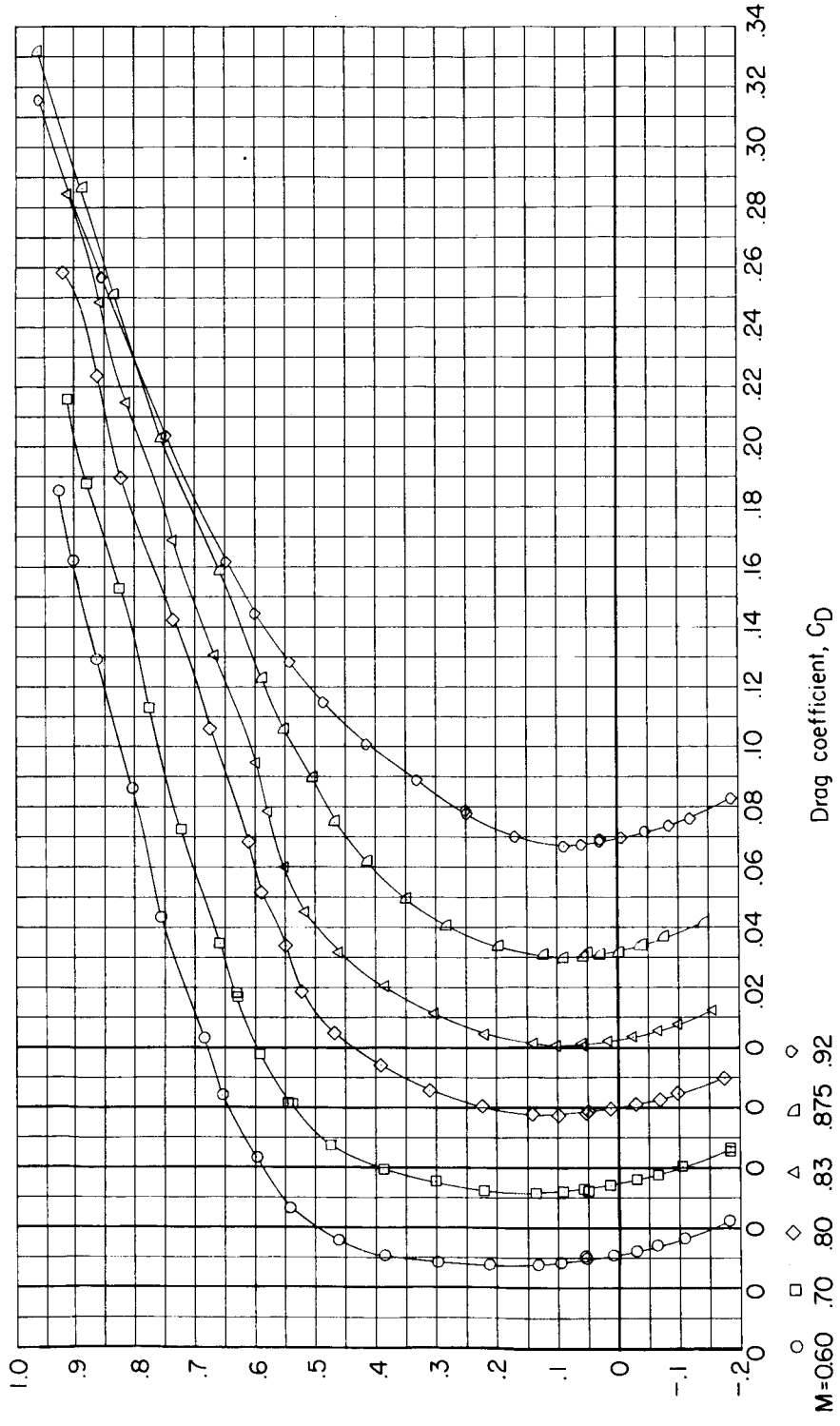

(b) Drag coefficient.

Figure 19.- Continued.

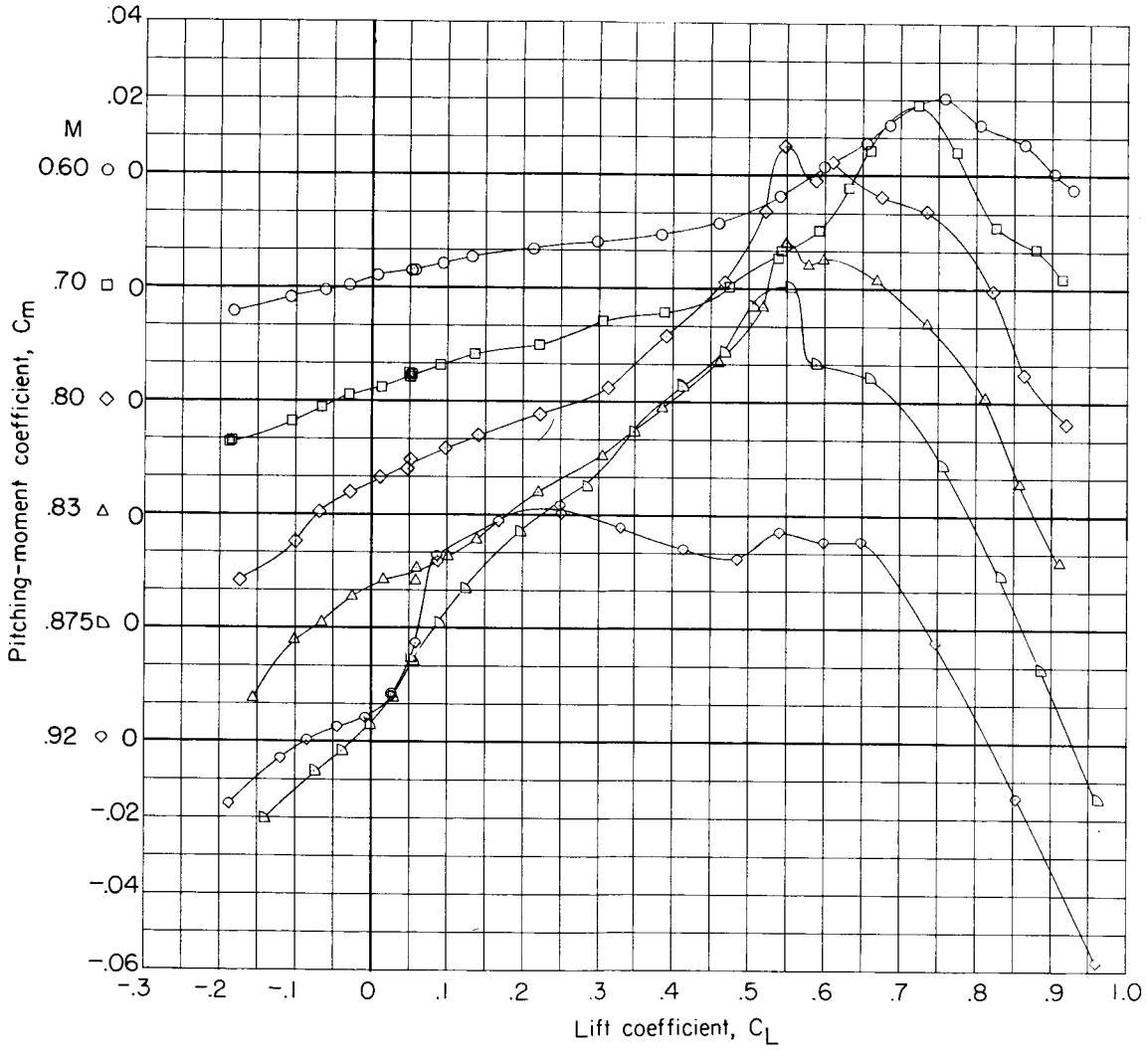

(c) Pitching-moment coefficient.

Figure 19.- Concluded.

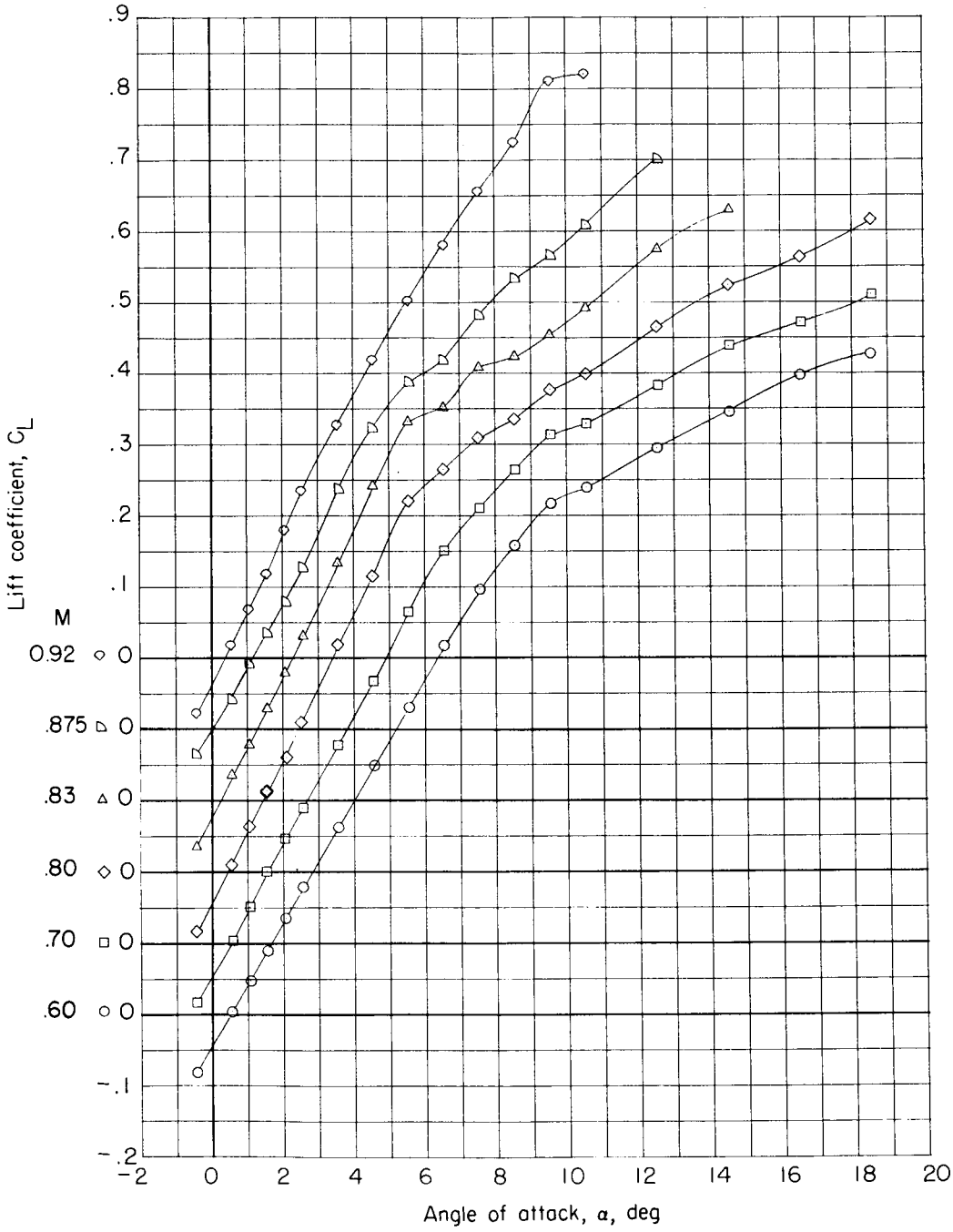

(a) Lift coefficient.

Figure 20.- Aerodynamic characteristics for configuration B_1WE with $\delta_{le} = 12^\circ$.

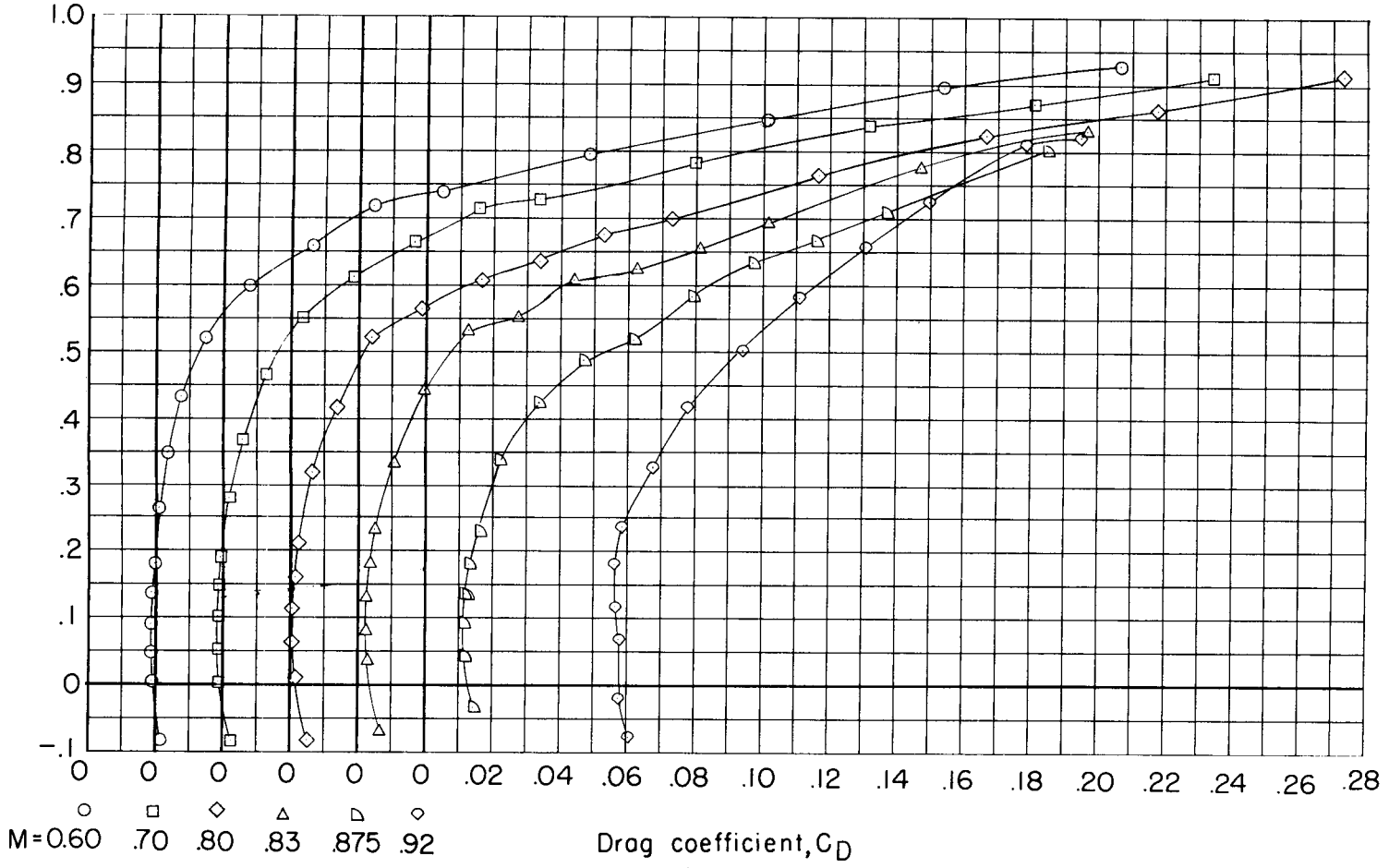

(b) Drag coefficient.

Figure 20.- Continued.

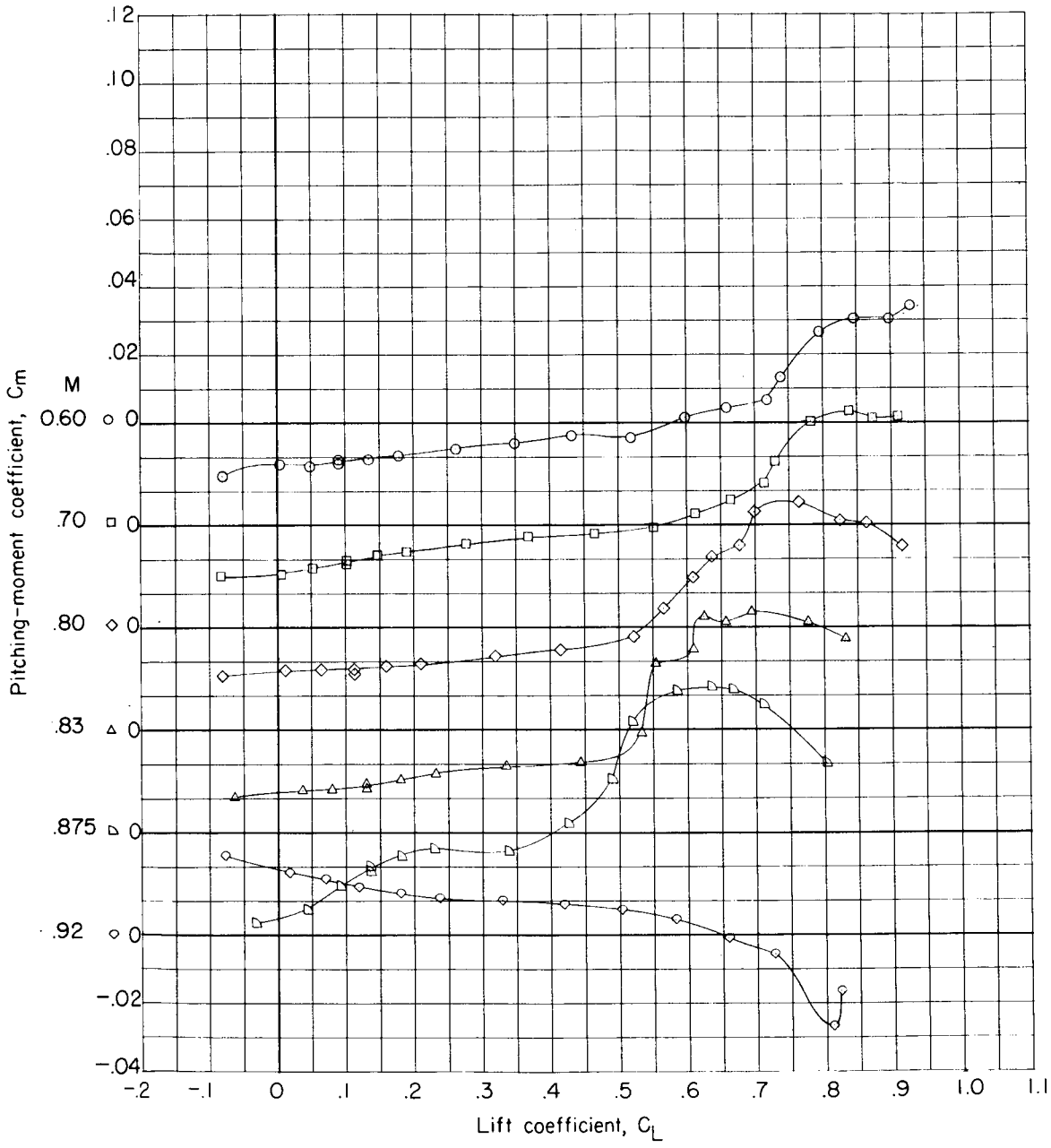

(c) Pitching-moment coefficient.

Figure 20.- Concluded.

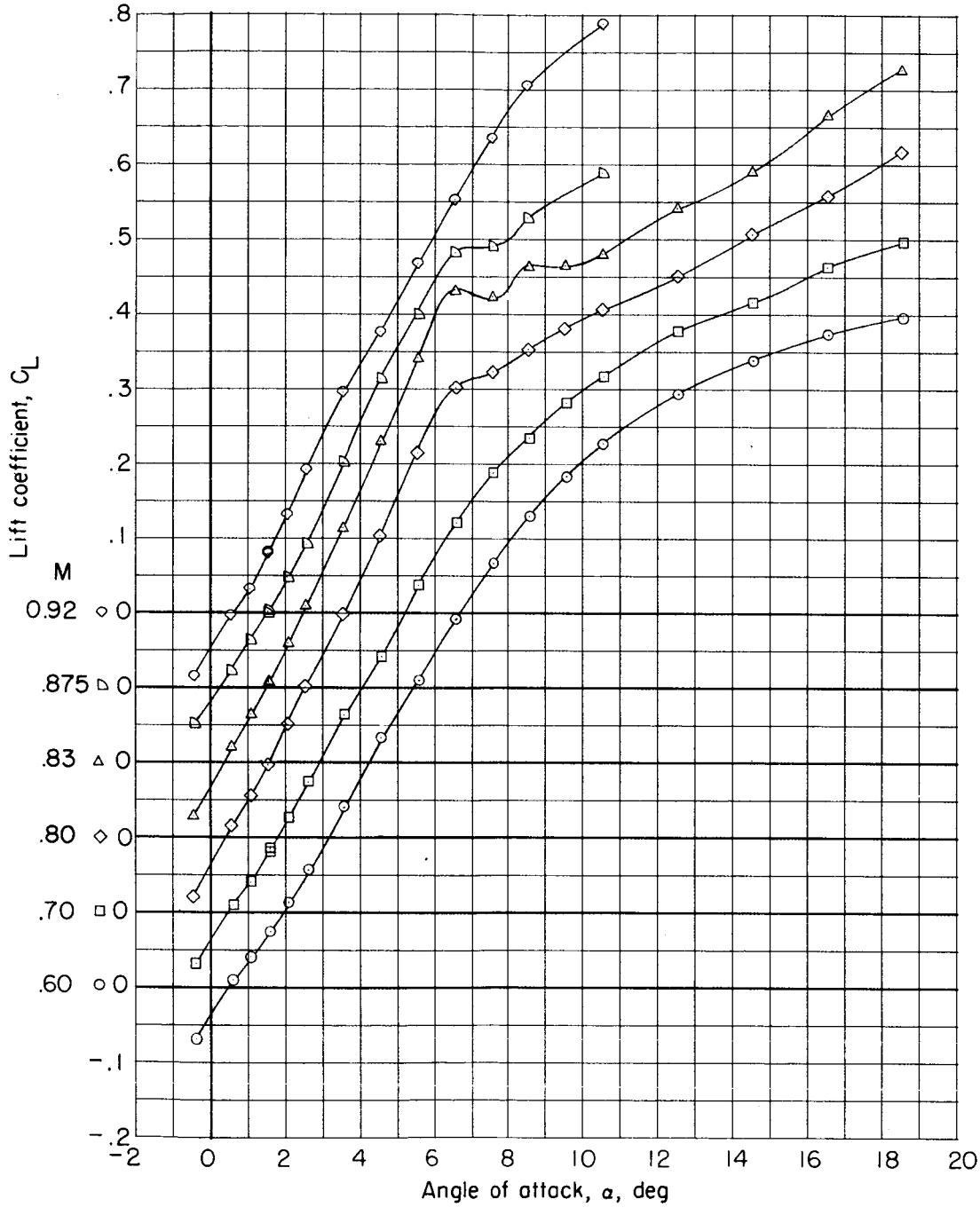

(a) Lift coefficient.

Figure 21.- Aerodynamic characteristics for configuration BWE with $\delta_{le} = 12^{\circ}$ (free transition).

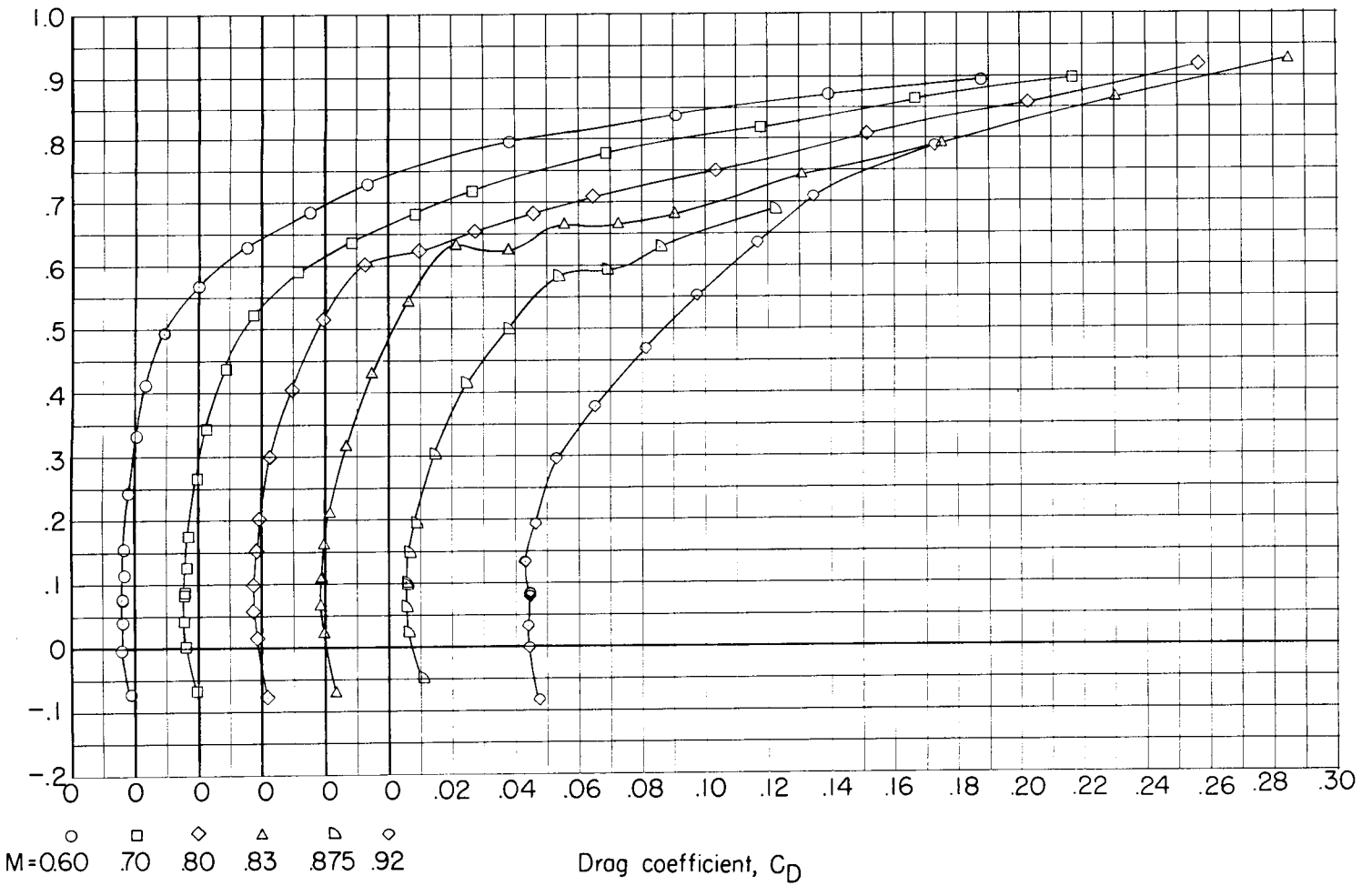

(b) Drag coefficient.

Figure 21.- Continued.

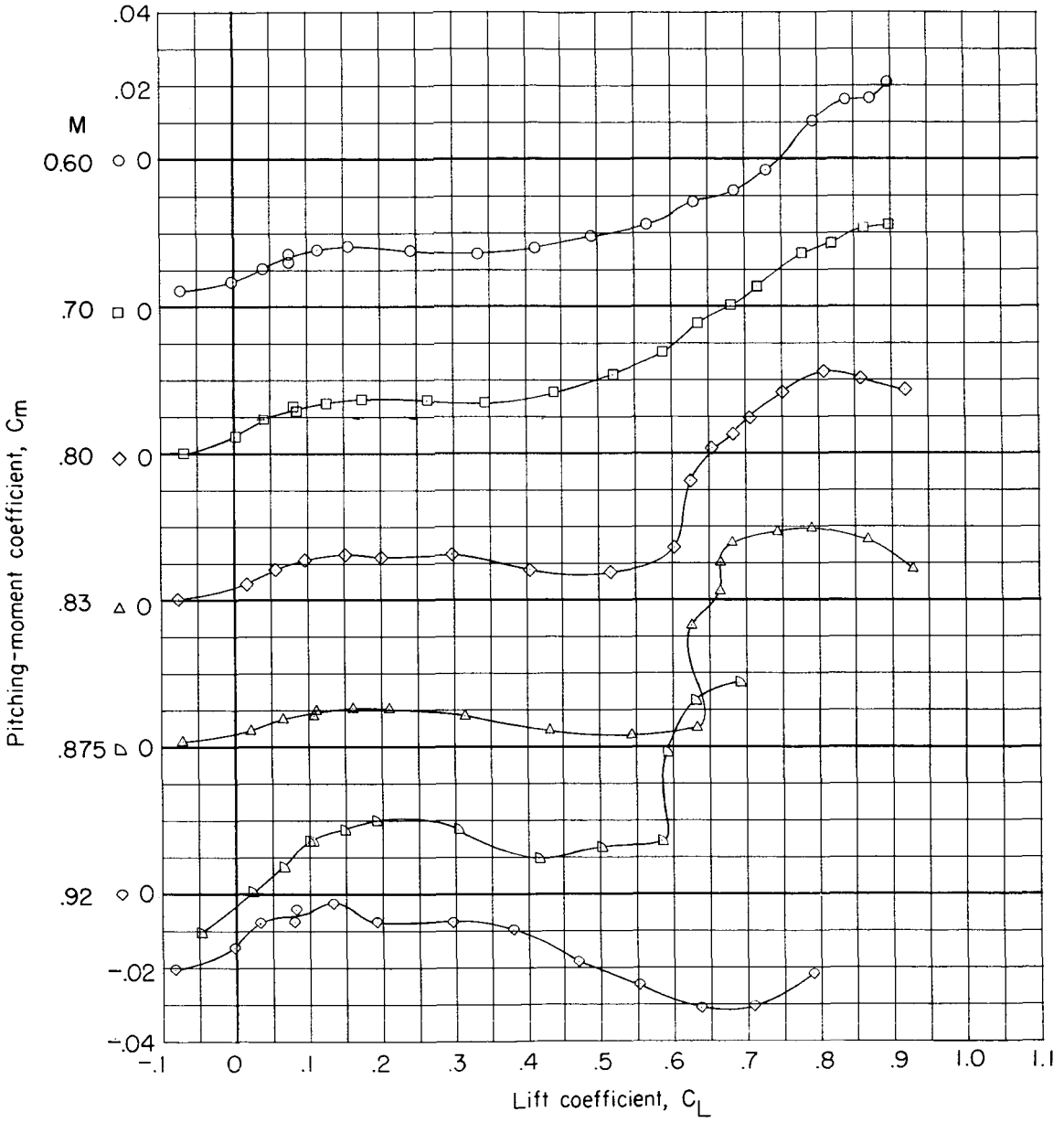

(c) Pitching-moment coefficient.

Figure 21.- Concluded.

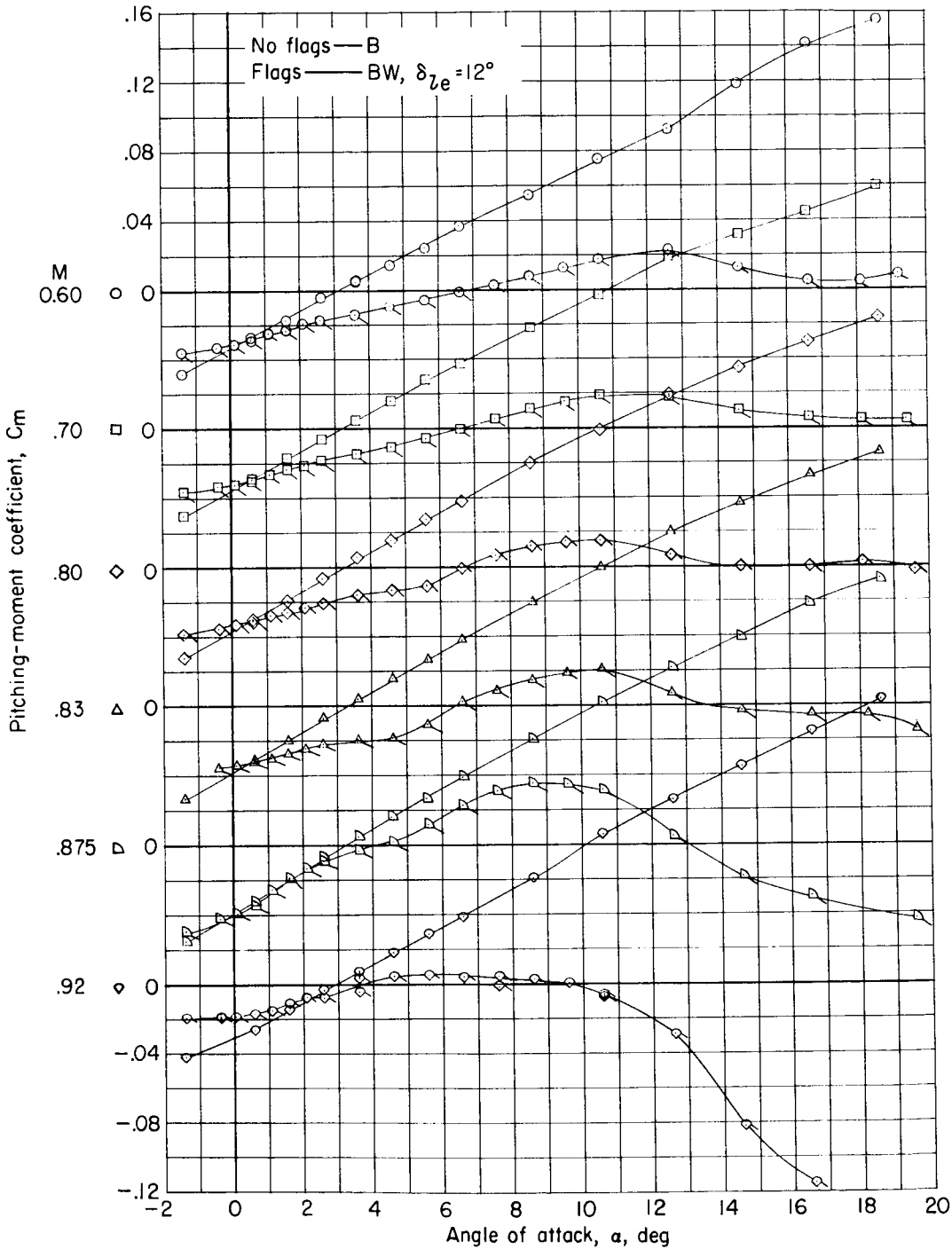

Figure 22.- A comparison of the pitching-moment coefficients for configurations B and BW with $\delta_{le} = 12^{o}$.

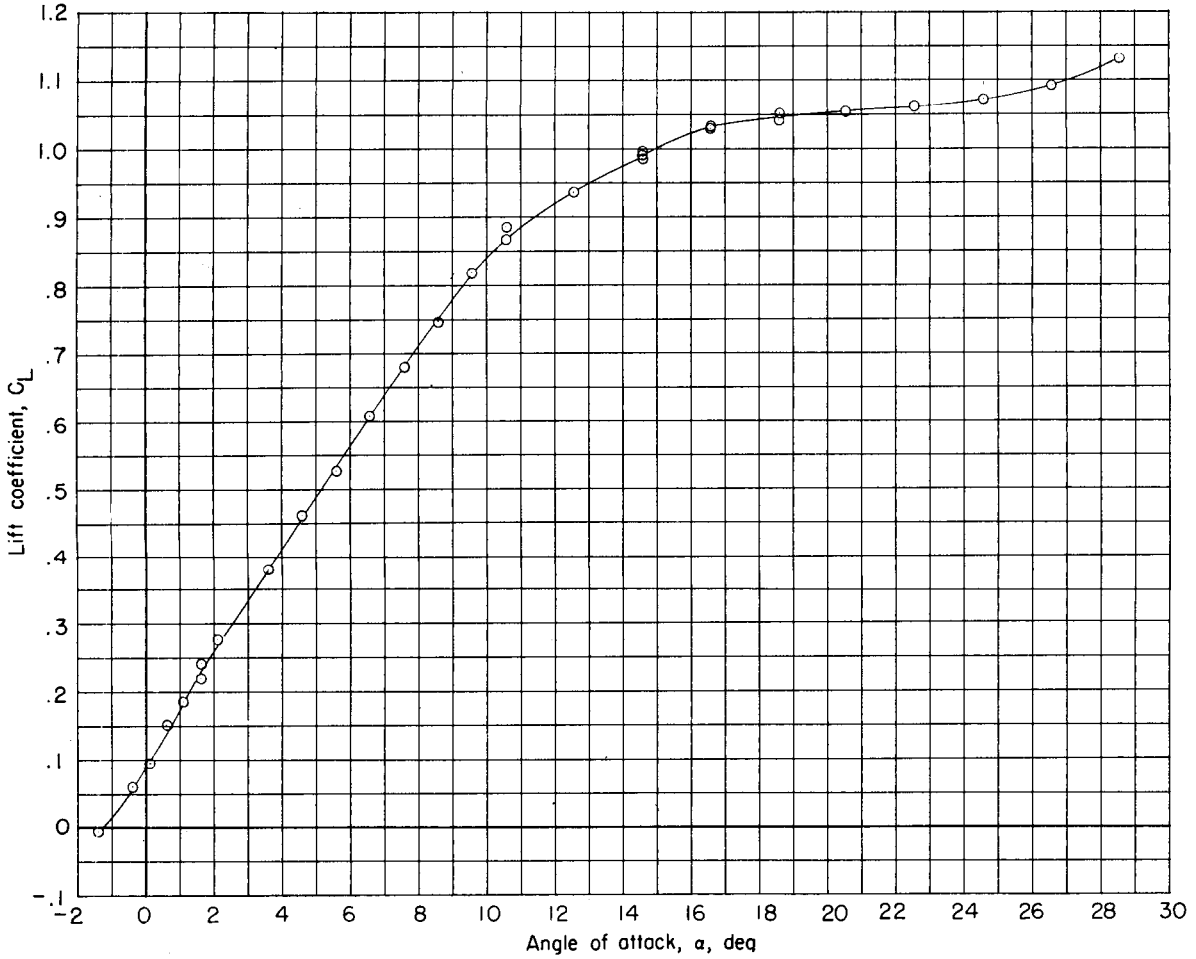

(a) Lift coefficient.

Figure 23.- Aerodynamic characteristics for configuration BWE with $\delta_{le} = 25°$, $\delta_{te} = 25°$, and $\delta_{tr} = 25°$ at M = 0.30.

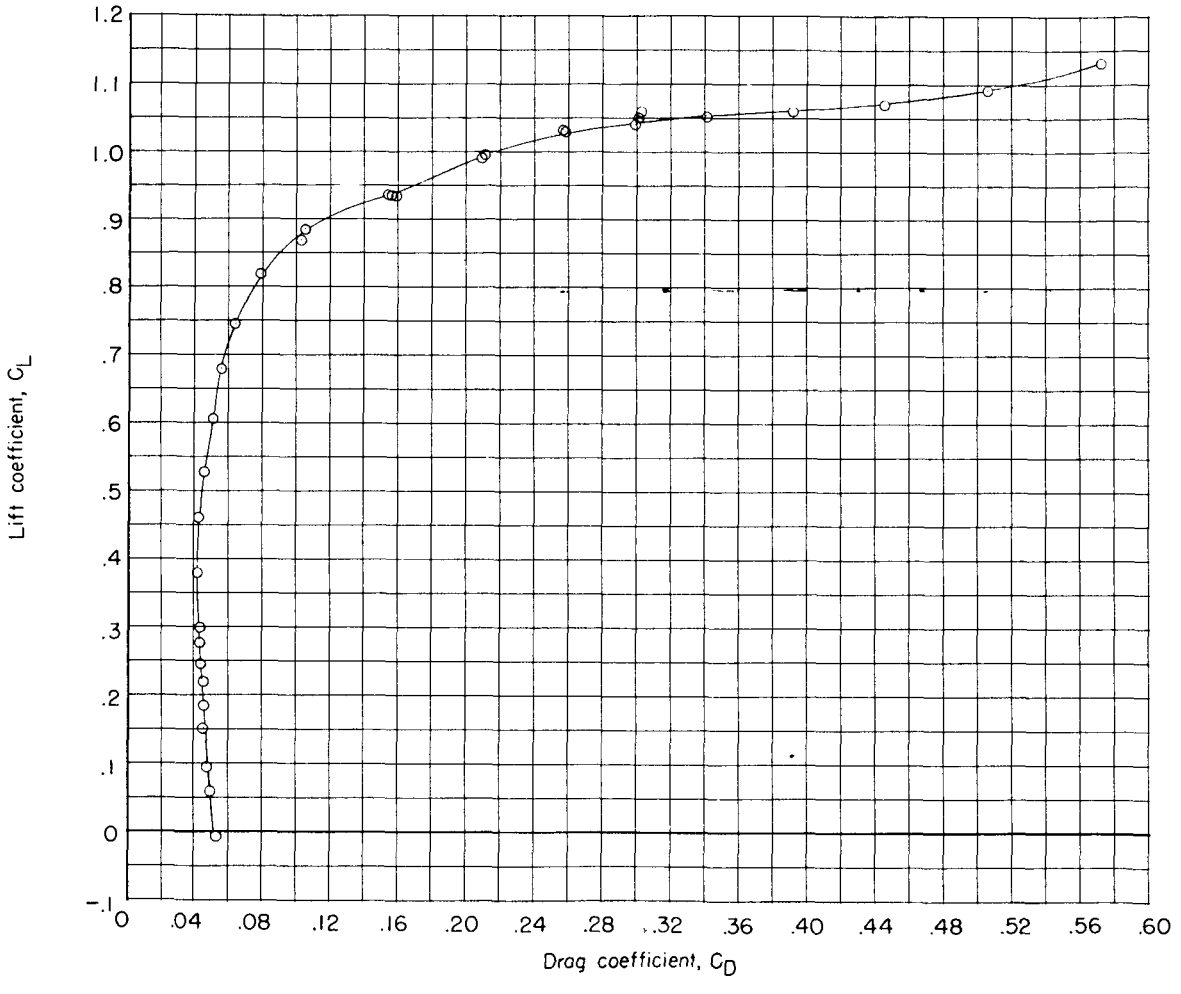

(b) Drag coefficient.

Figure 23.- Continued.

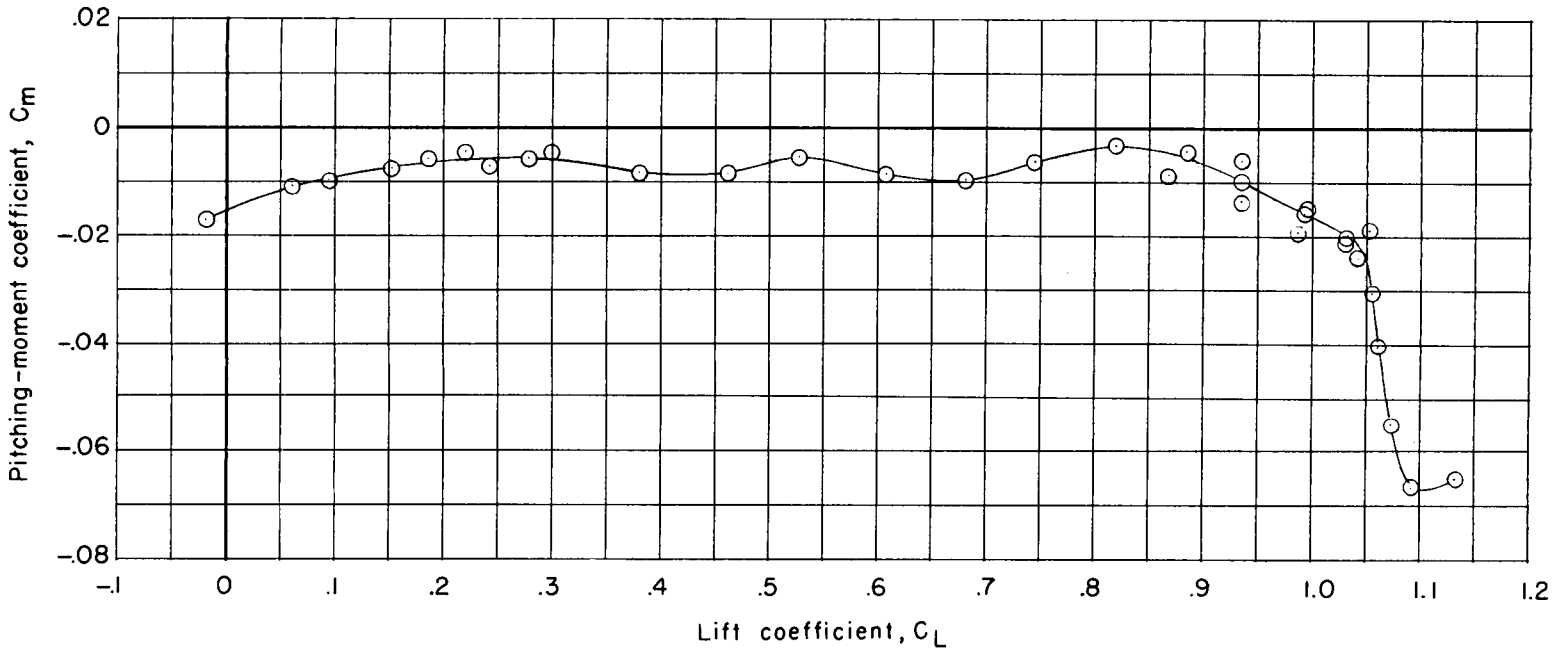

(c) Pitching-moment coefficient.

Figure 23.- Concluded.

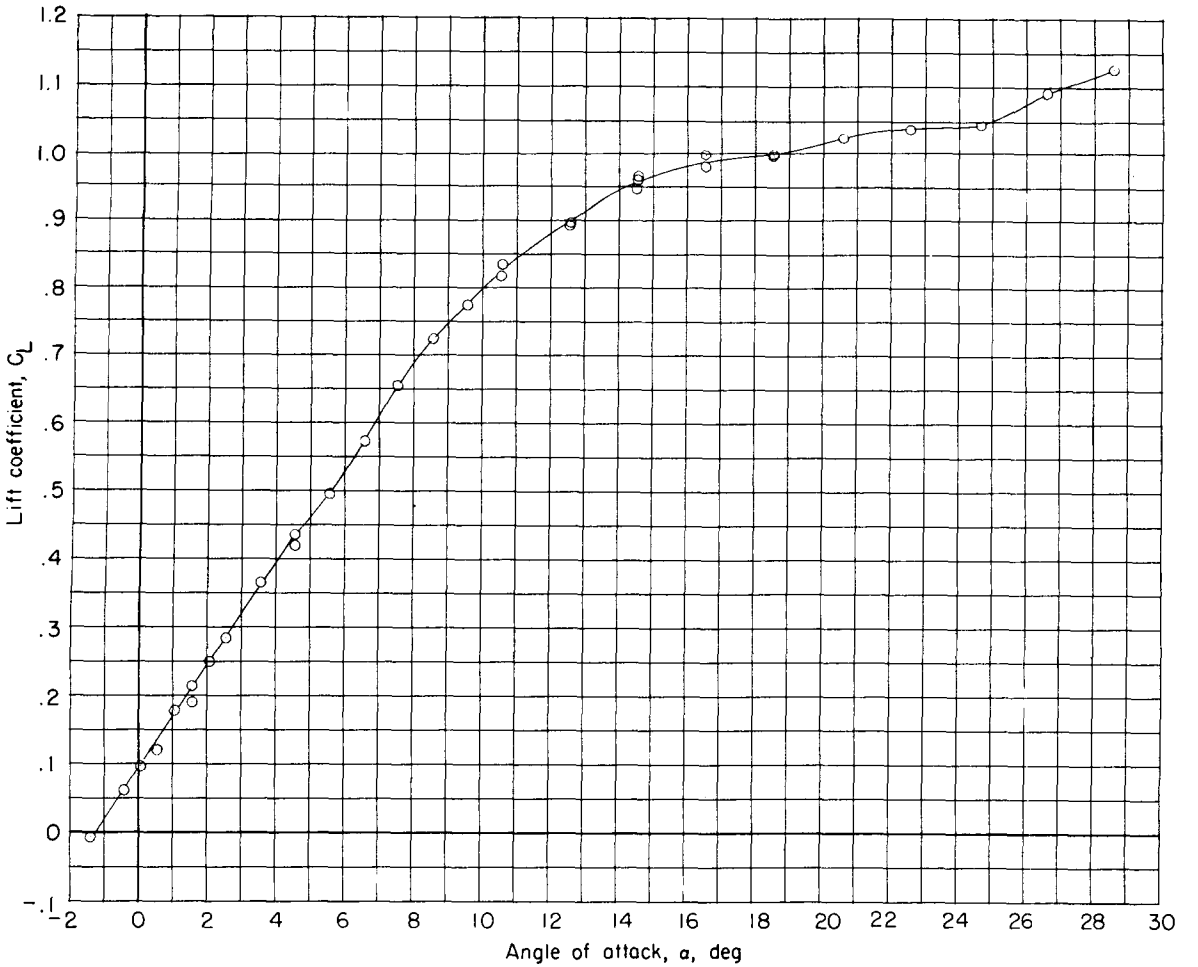

(a) Lift coefficient.

Figure 24.- Aerodynamic characteristics for configuration BWE with $\delta_{le} = 40^\circ$, $\delta_{te} = 25^\circ$, and $\delta_{tr} = 25^\circ$ at M = 0.30.

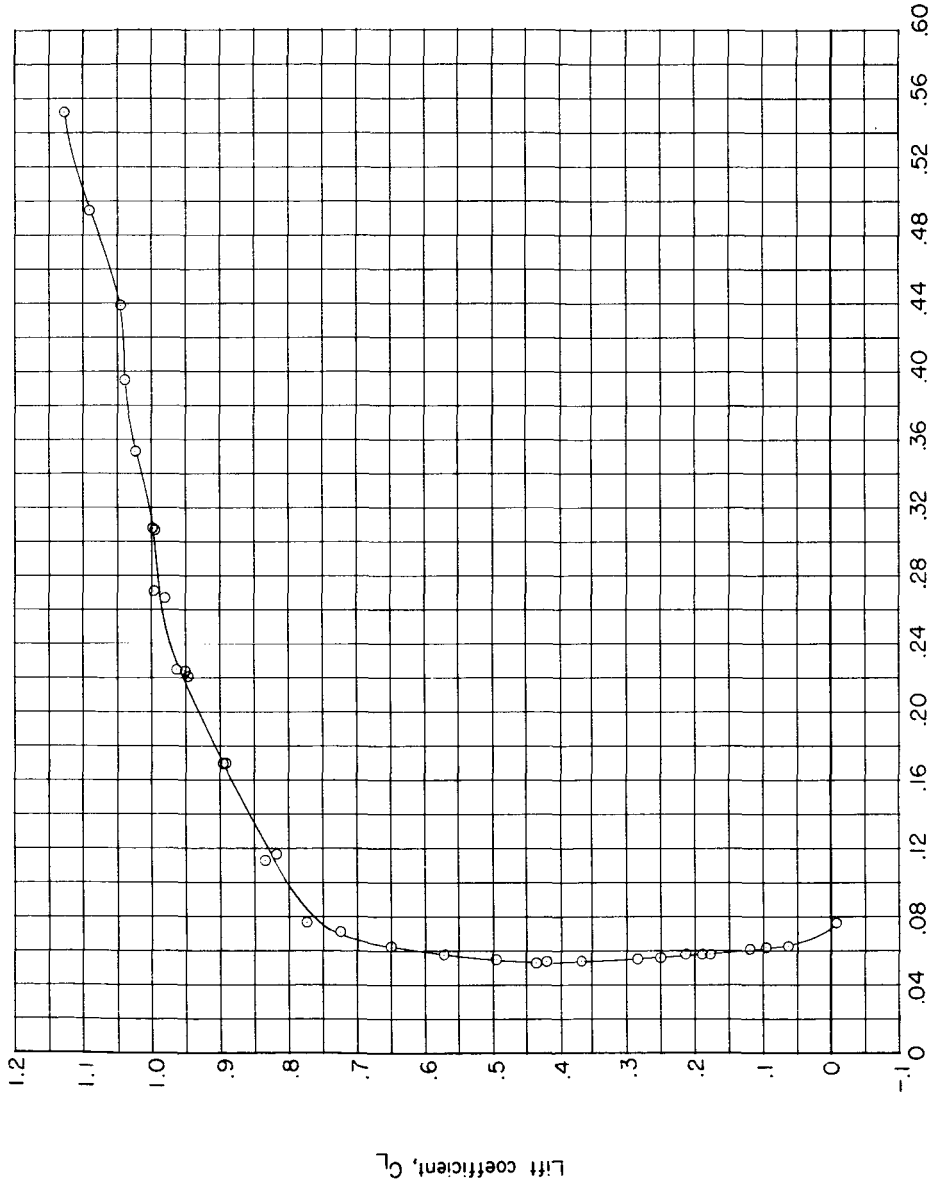

(b) Drag coefficient.

Figure 24.- Continued.

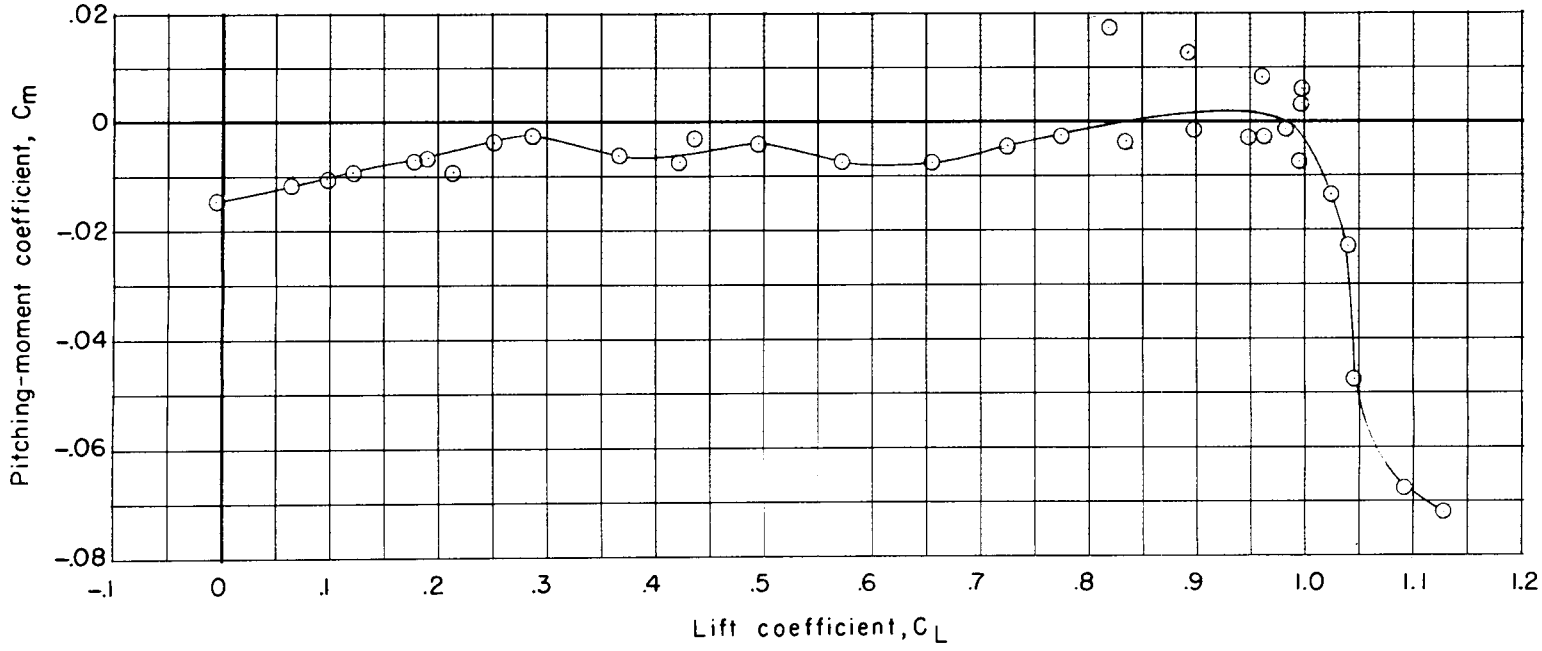

(c) Pitching-moment coefficient.

Figure 24.- Concluded.

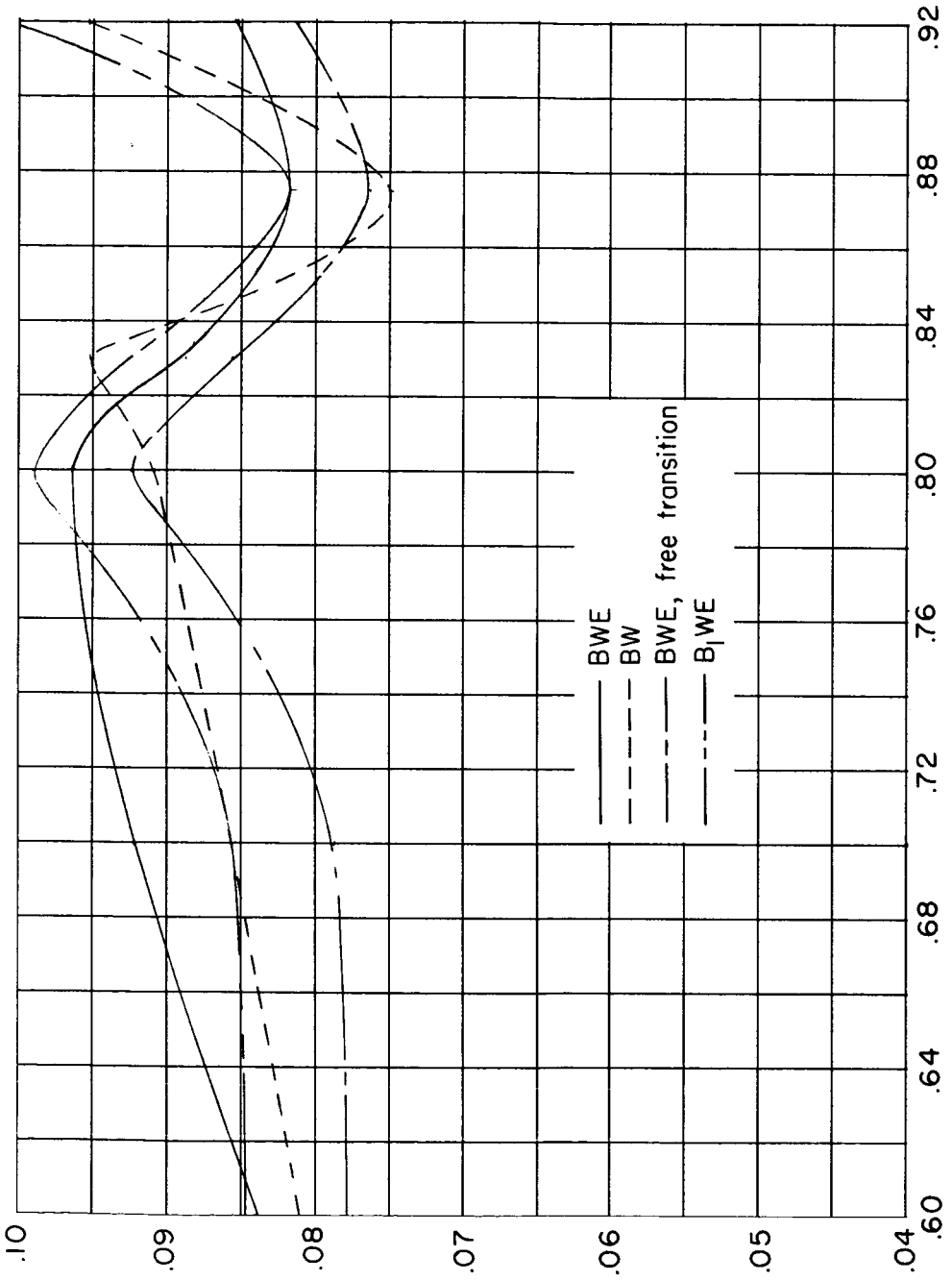

Figure 25.- Variation of lift-curve slope with Mach number. $\delta_{le} = 12^{\circ}$.

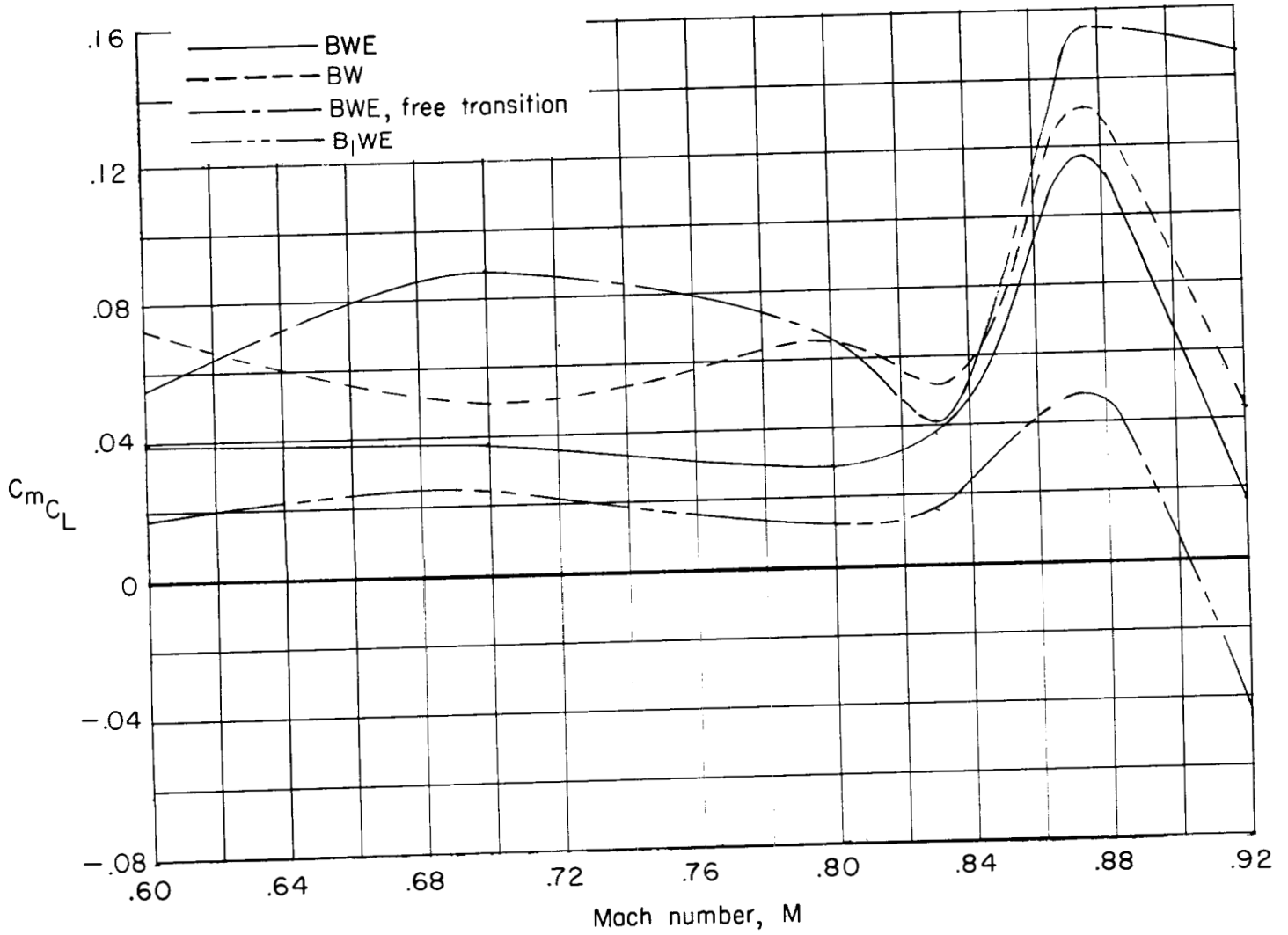

Figure 26.- Variation of $C_{m_{C_L}}$ with Mach number. $\delta_{le} = 12^{\circ}$.

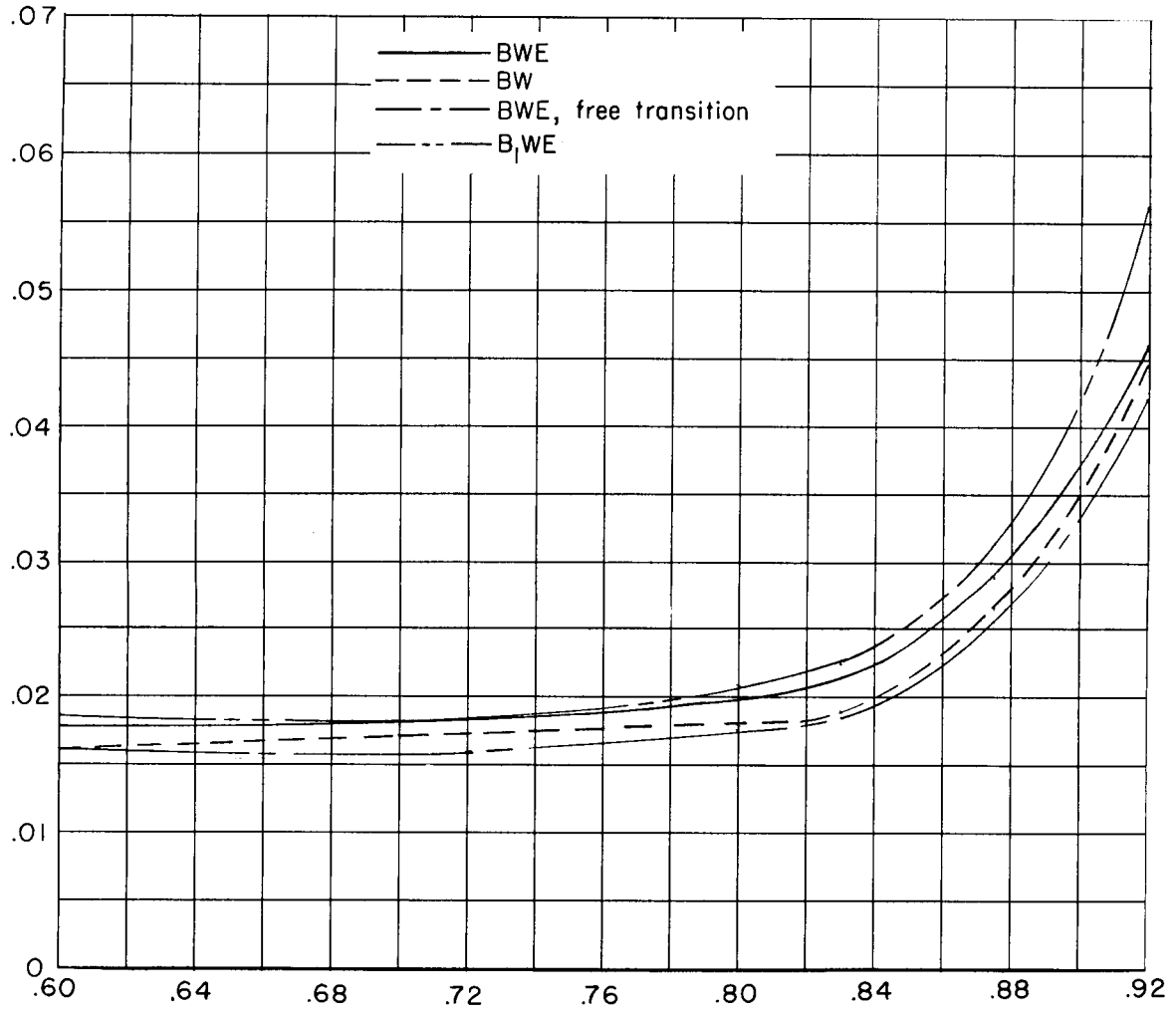

Figure 27.- Variation of $C_{D,min}$ with Mach number. $\delta_{le} = 12^{\circ}$.

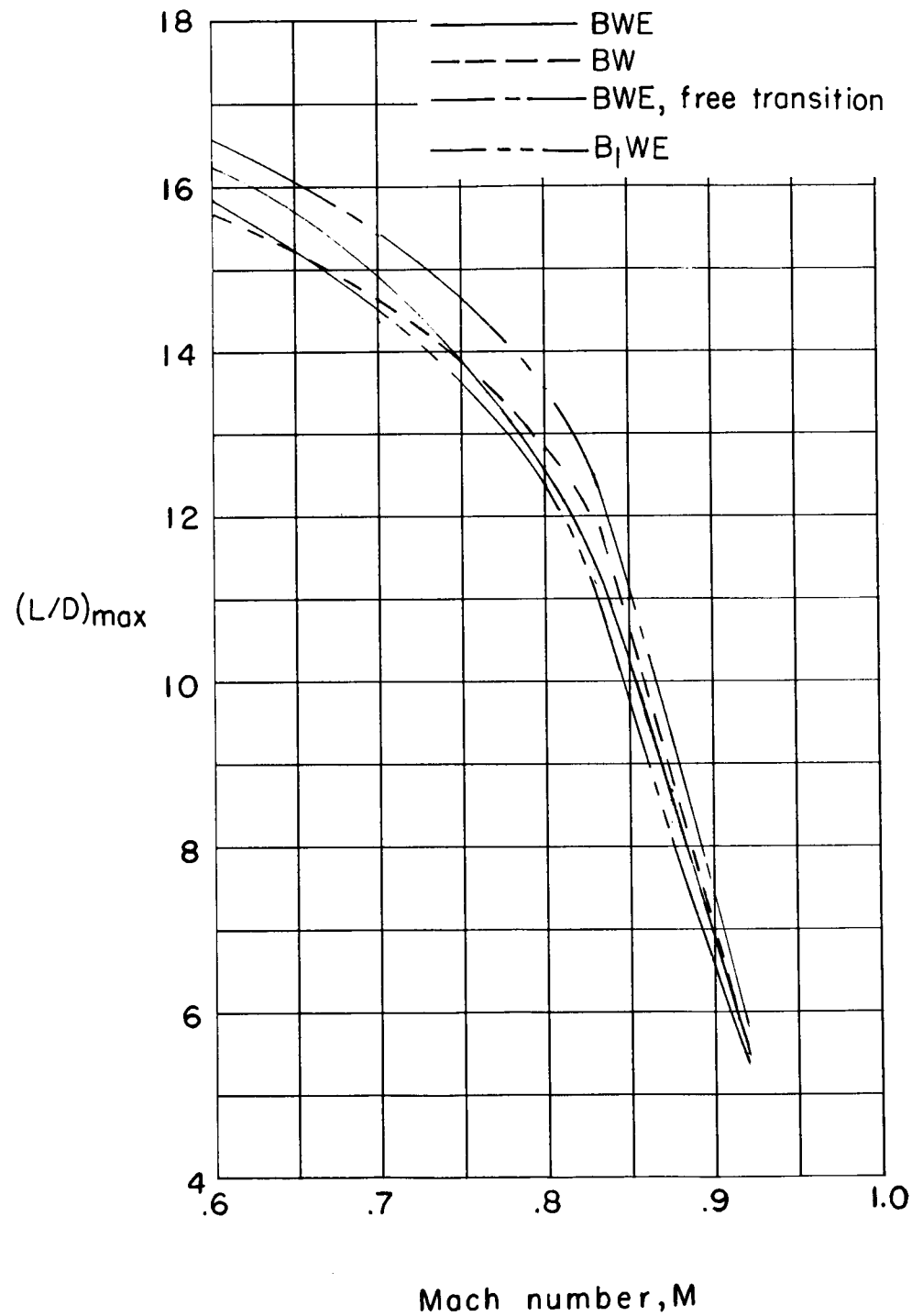

Figure 28.- Variation of $(L/D)_{max}$ with Mach number. $\delta_{le} = 12^{\circ}$.

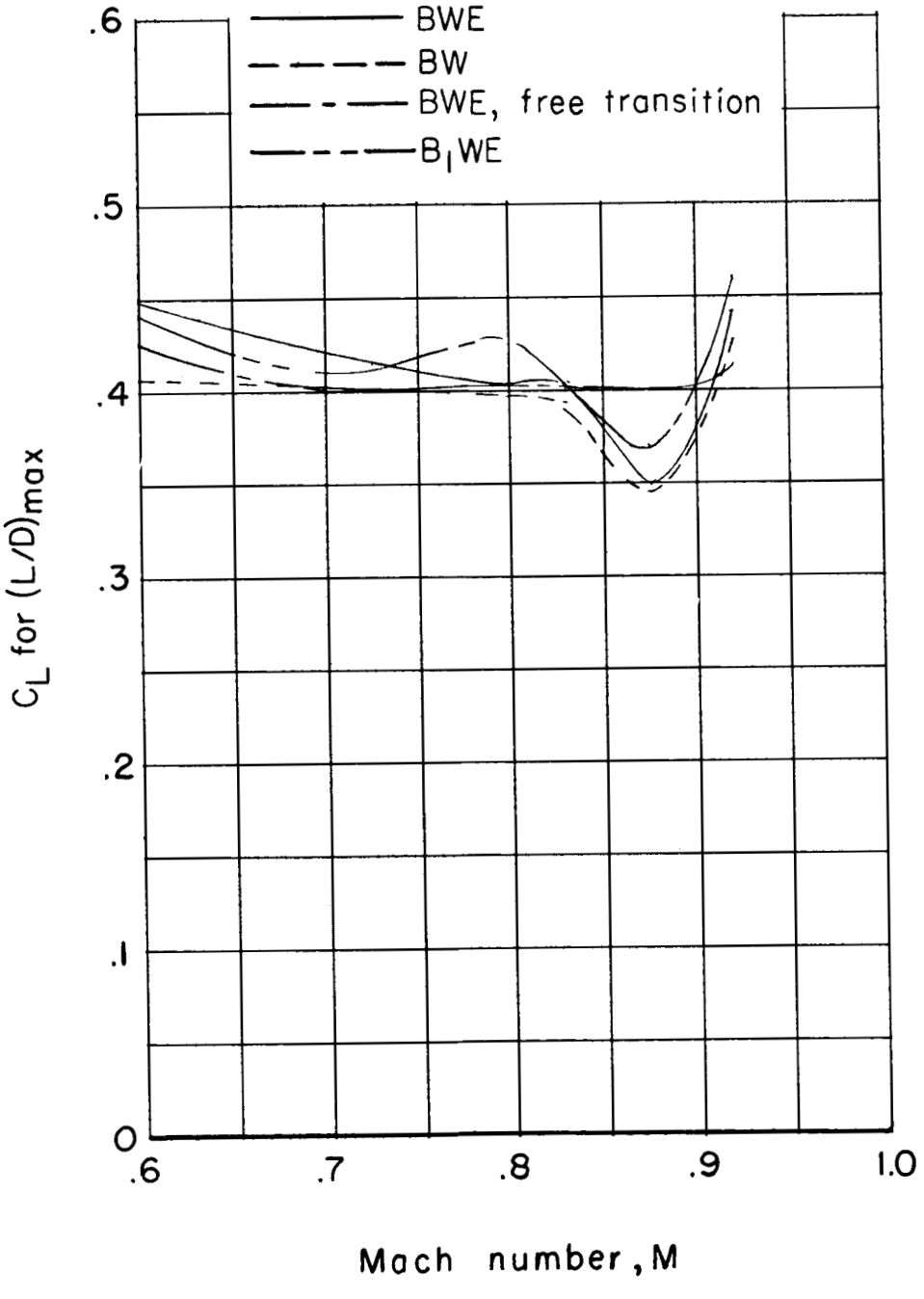

Figure 29.- Variation of C_L for $(L/D)_{max}$ with Mach number. $\delta_{le} = 12^{\circ}$.

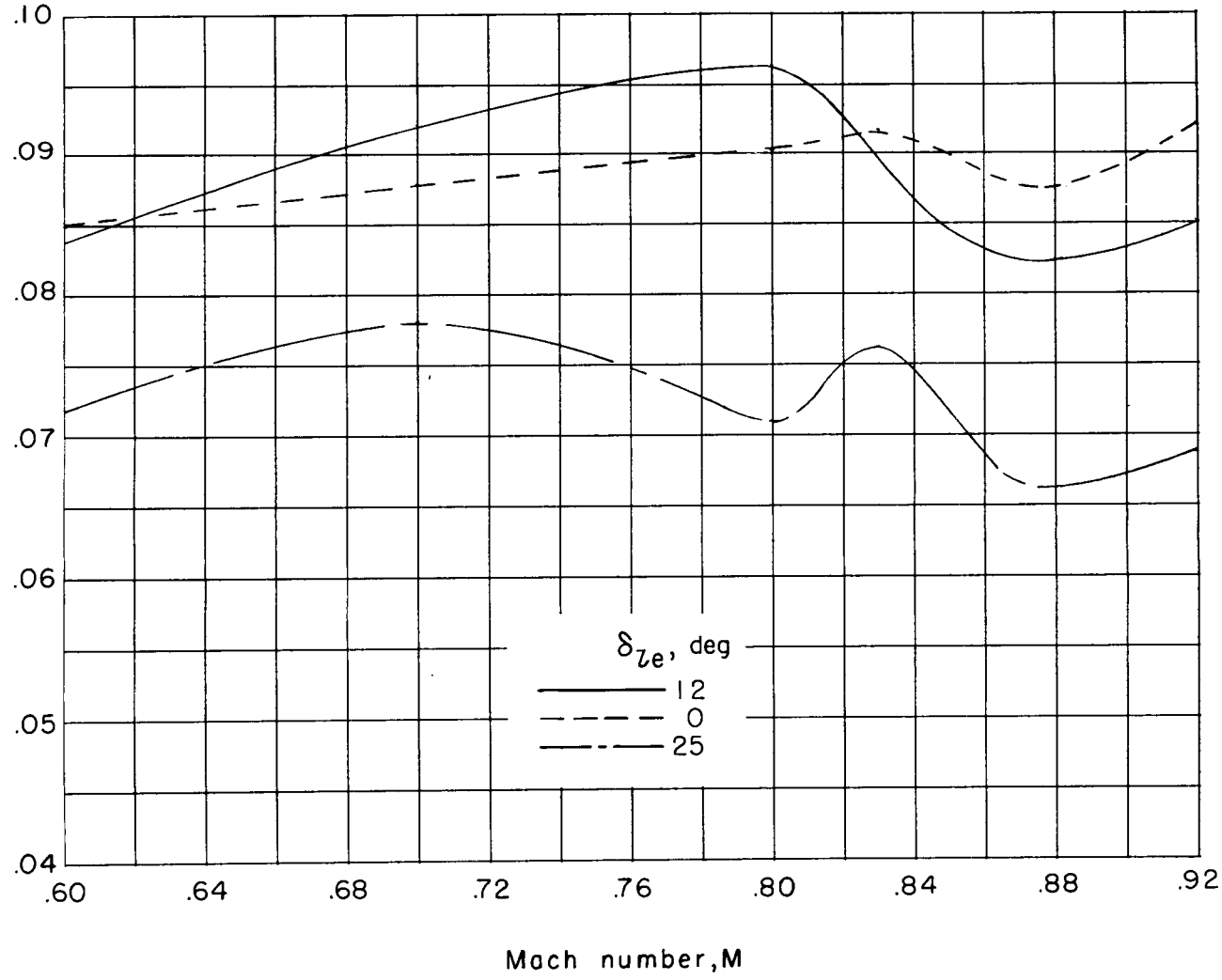

Figure 30.- Effect of deflection of leading-edge chord-extension on the variation of lift-curve slope with Mach number for configuration BWE.

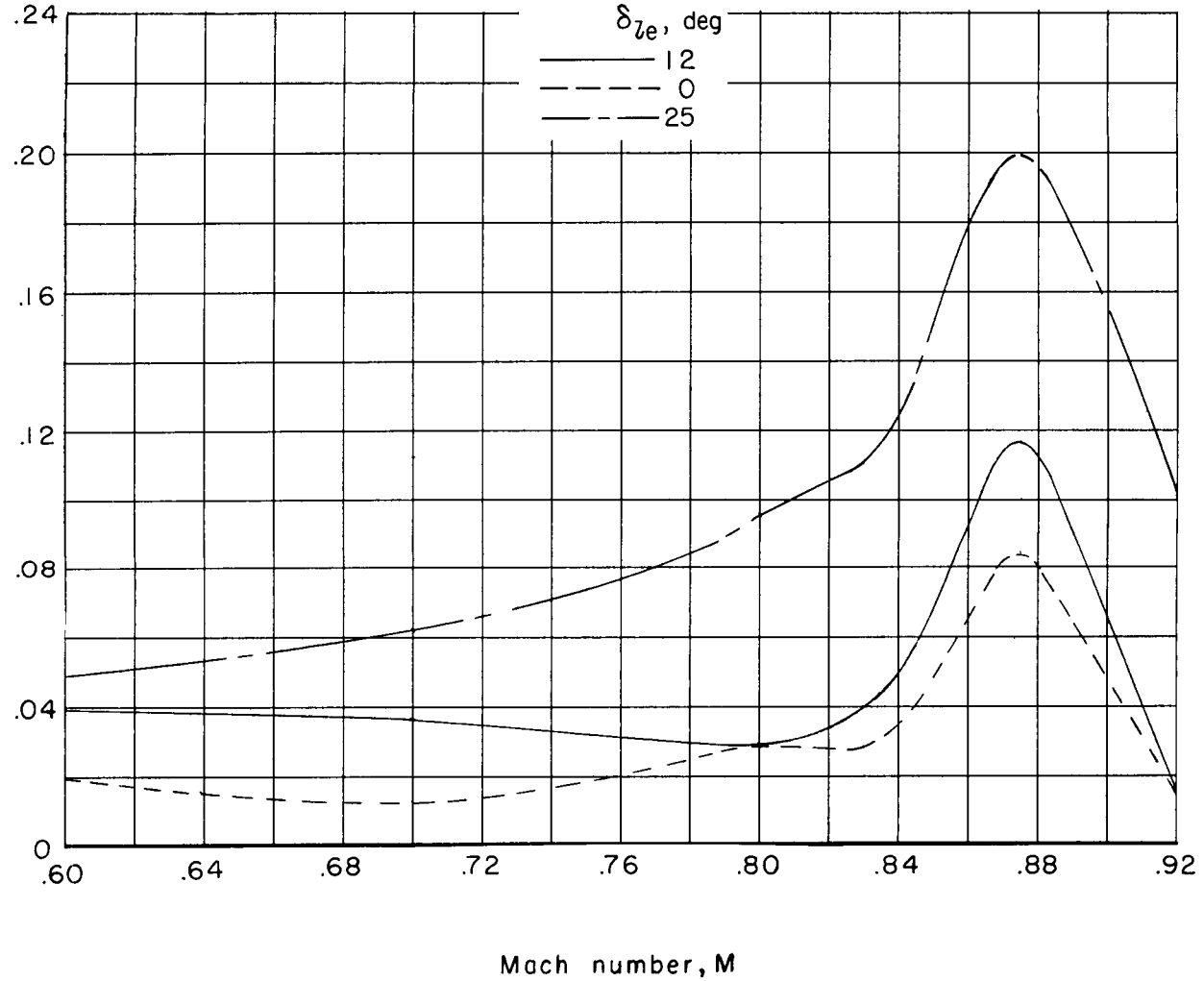

Figure 31.- Effect of deflection of leading-edge chord-extension on the variation of $C_{m_{C_L}}$ with Mach number for configuration BWE.

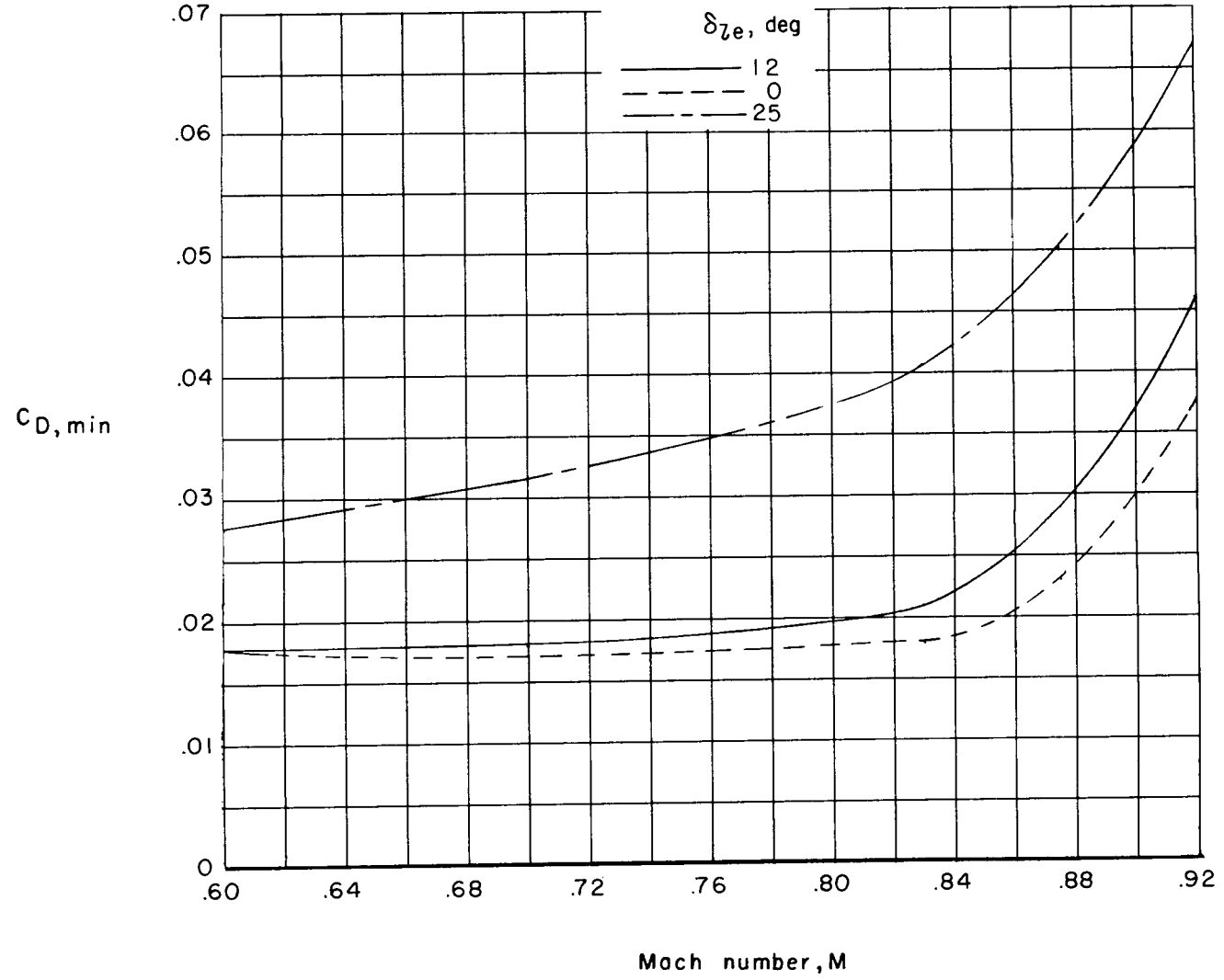

Figure 32.- Effect of deflection of leading-edge chord-extension on the variation of $C_{D,min}$ with Mach number for configuration BWE.

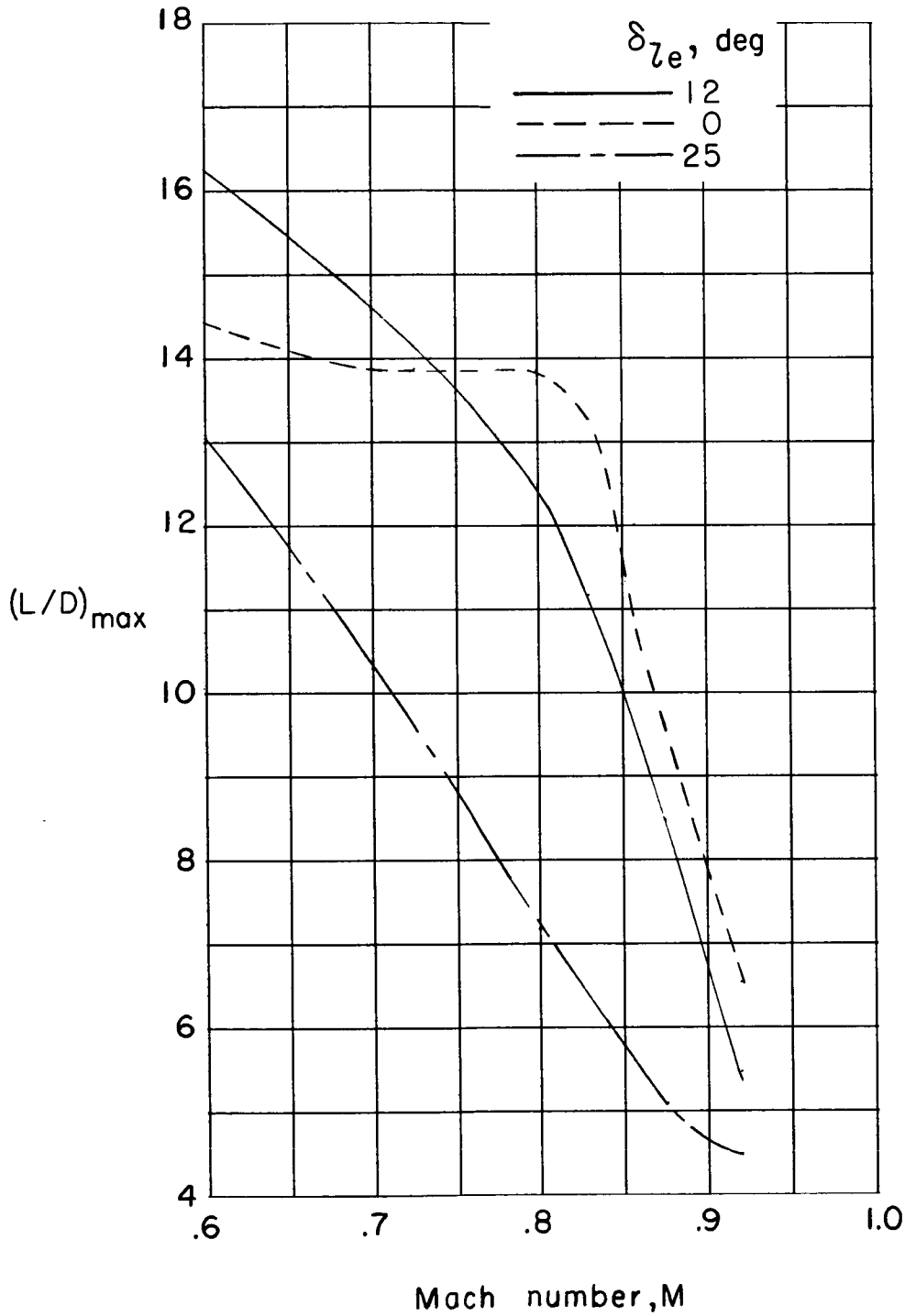

Figure 33.- Effect of deflection of leading-edge chord-extension on the variation of $(L/D)_{max}$ with Mach number for configuration BWE.

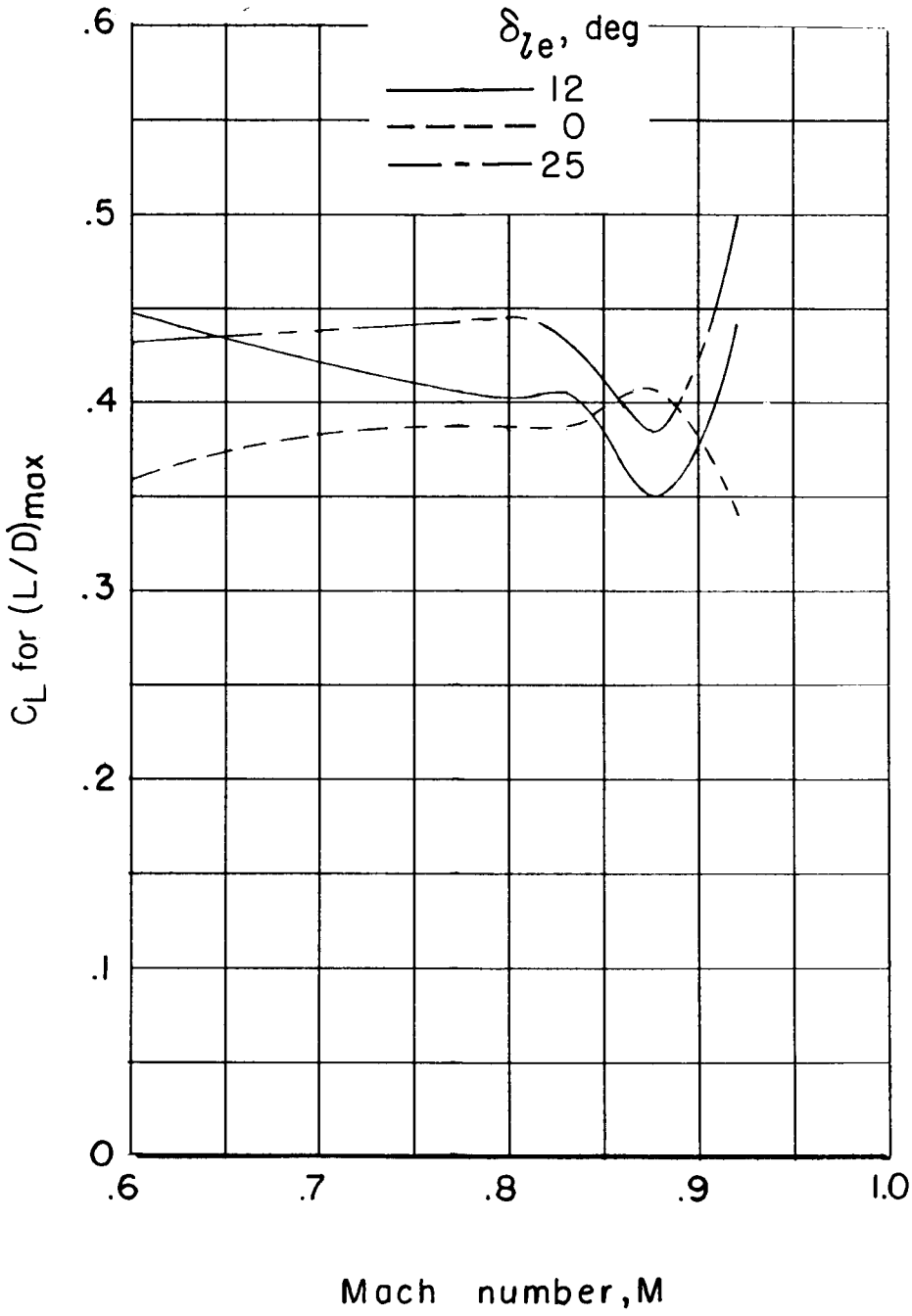

Figure 34.- Effect of deflection of leading-edge chord-extension on the variation of C_L for $(L/D)_{max}$ with Mach number for configuration BWE.

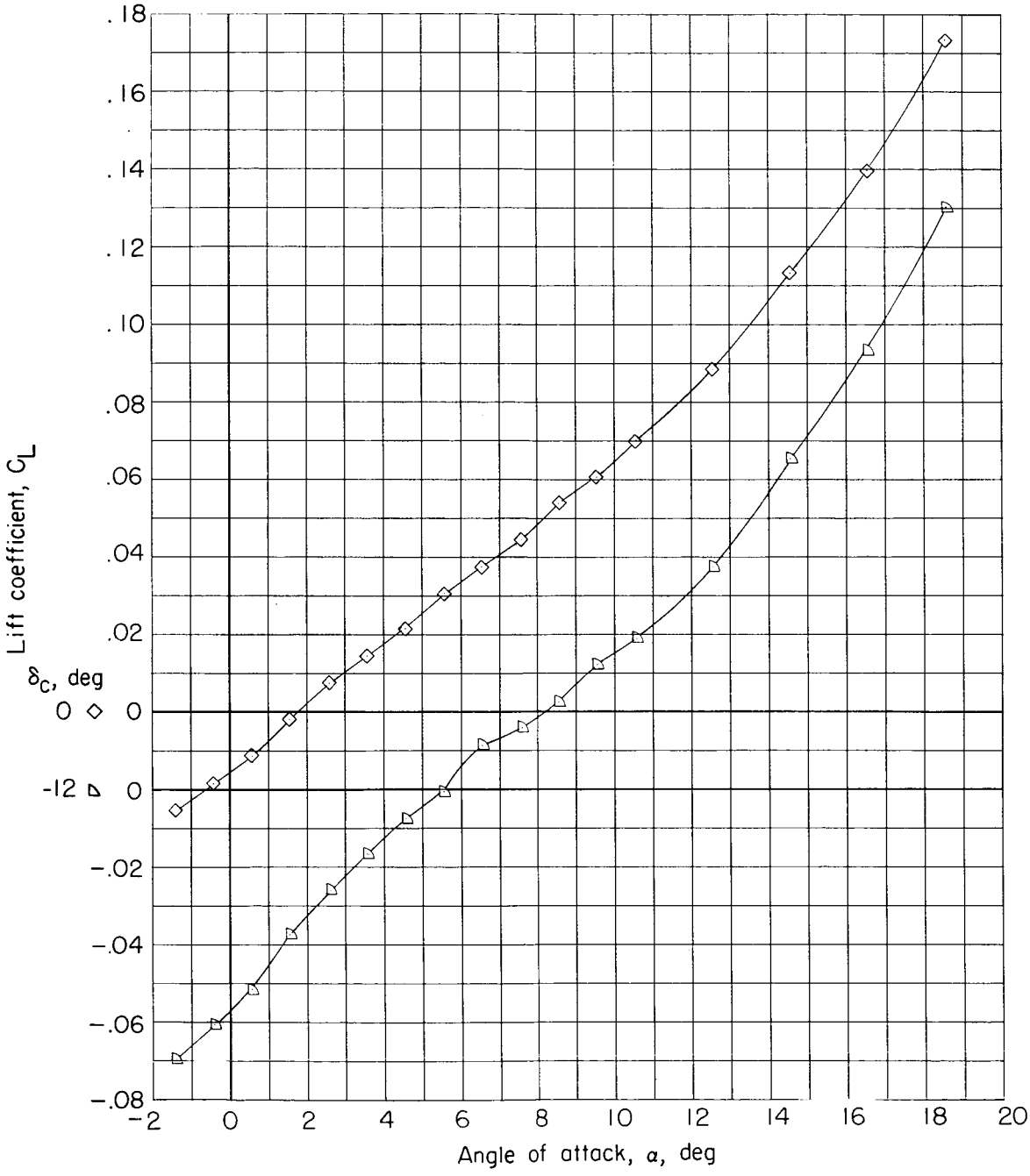

(a) Lift coefficient.

Figure 35.- Aerodynamic characteristics for configuration BC with $\delta_{tab} = 0^\circ$ at M = 0.80.

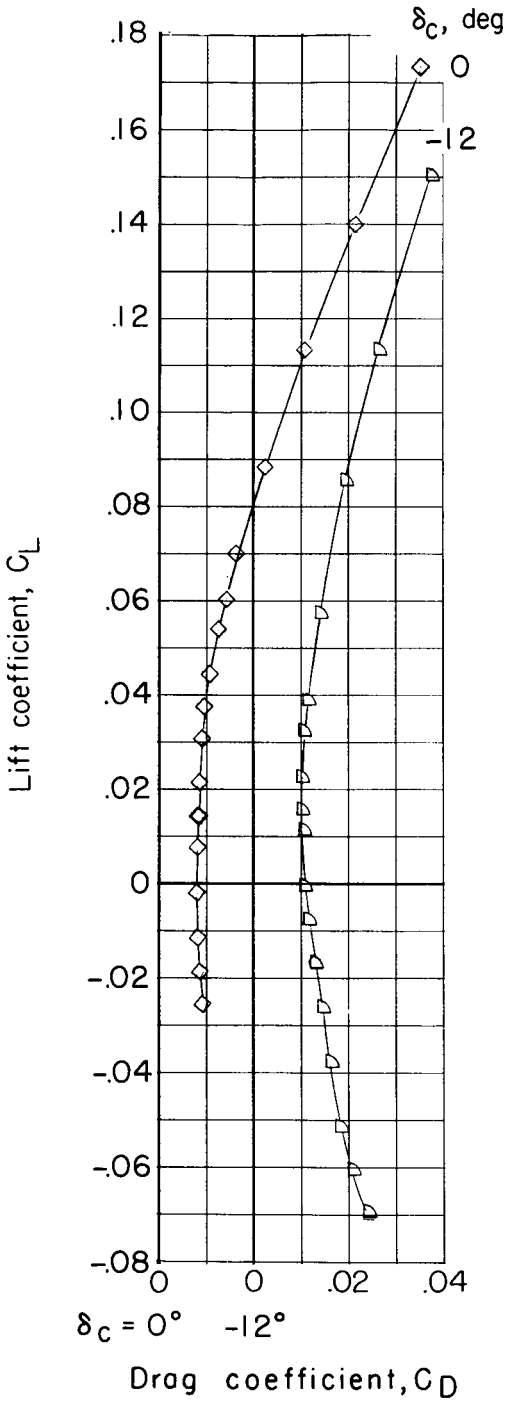

(b) Drag coefficient.

Figure 35.- Continued.

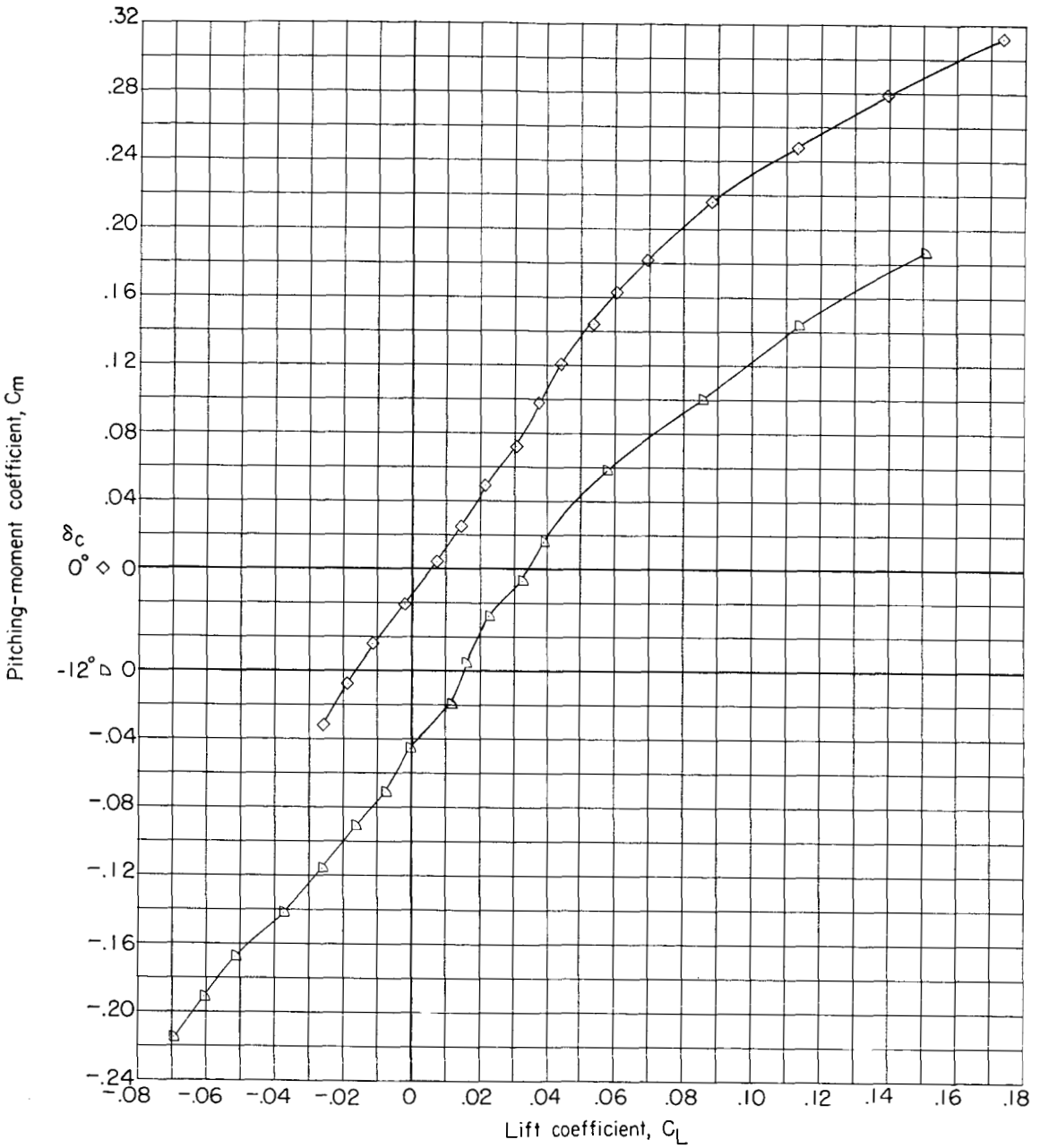

(c) Pitching-moment coefficient.

Figure 35.- Concluded.

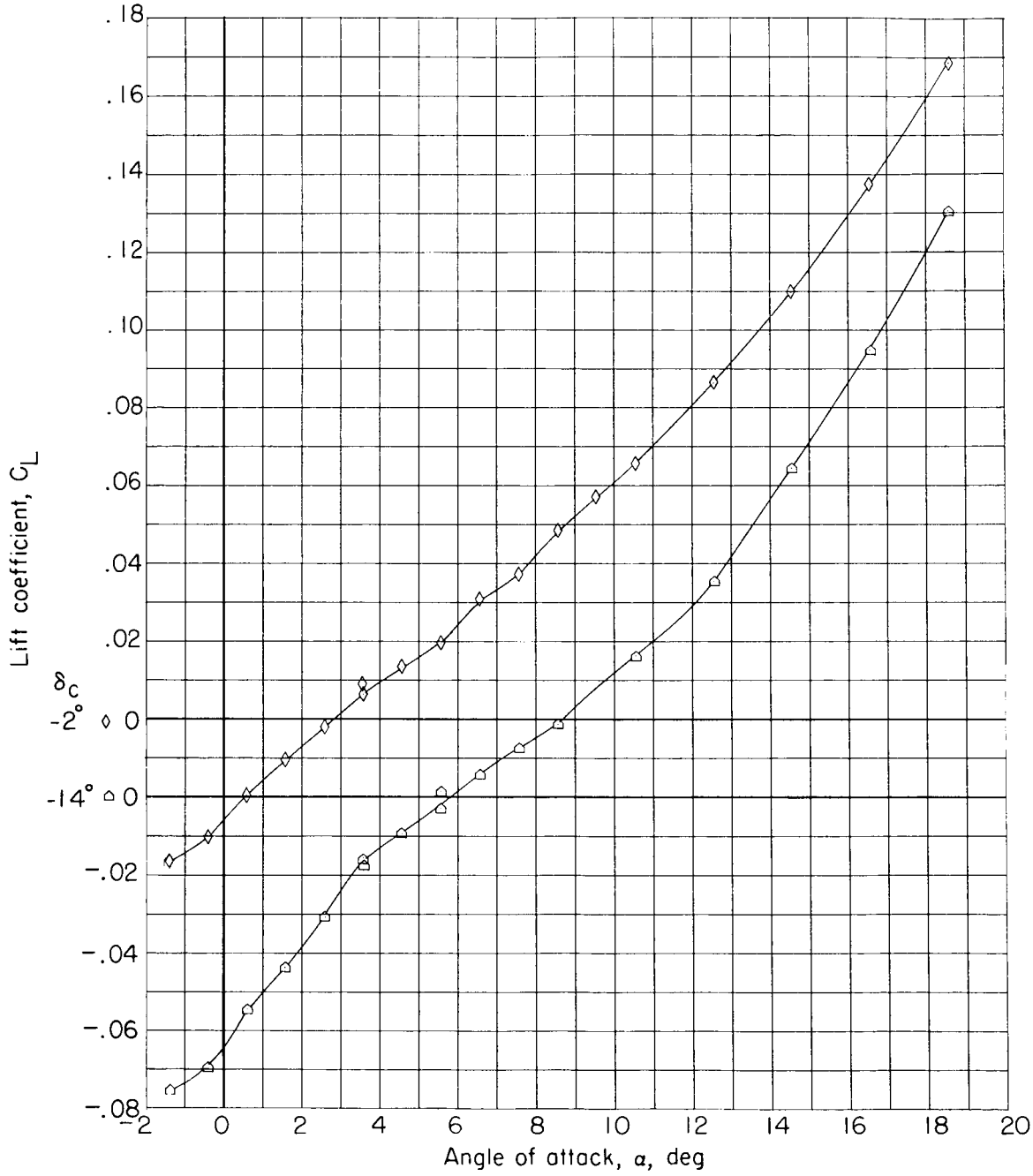

(a) Lift coefficient.

Figure 36.- Aerodynamic characteristics for configuration BC with $\delta_{tab} = 0^\circ$ at $M = 0.85$.

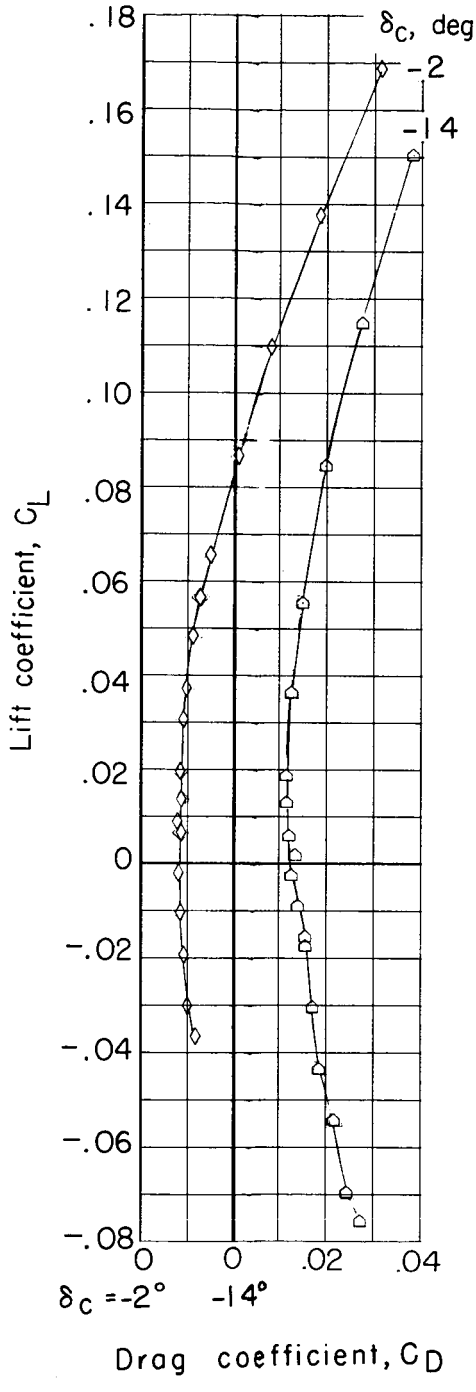

(b) Drag coefficient.

Figure 36.- Continued.

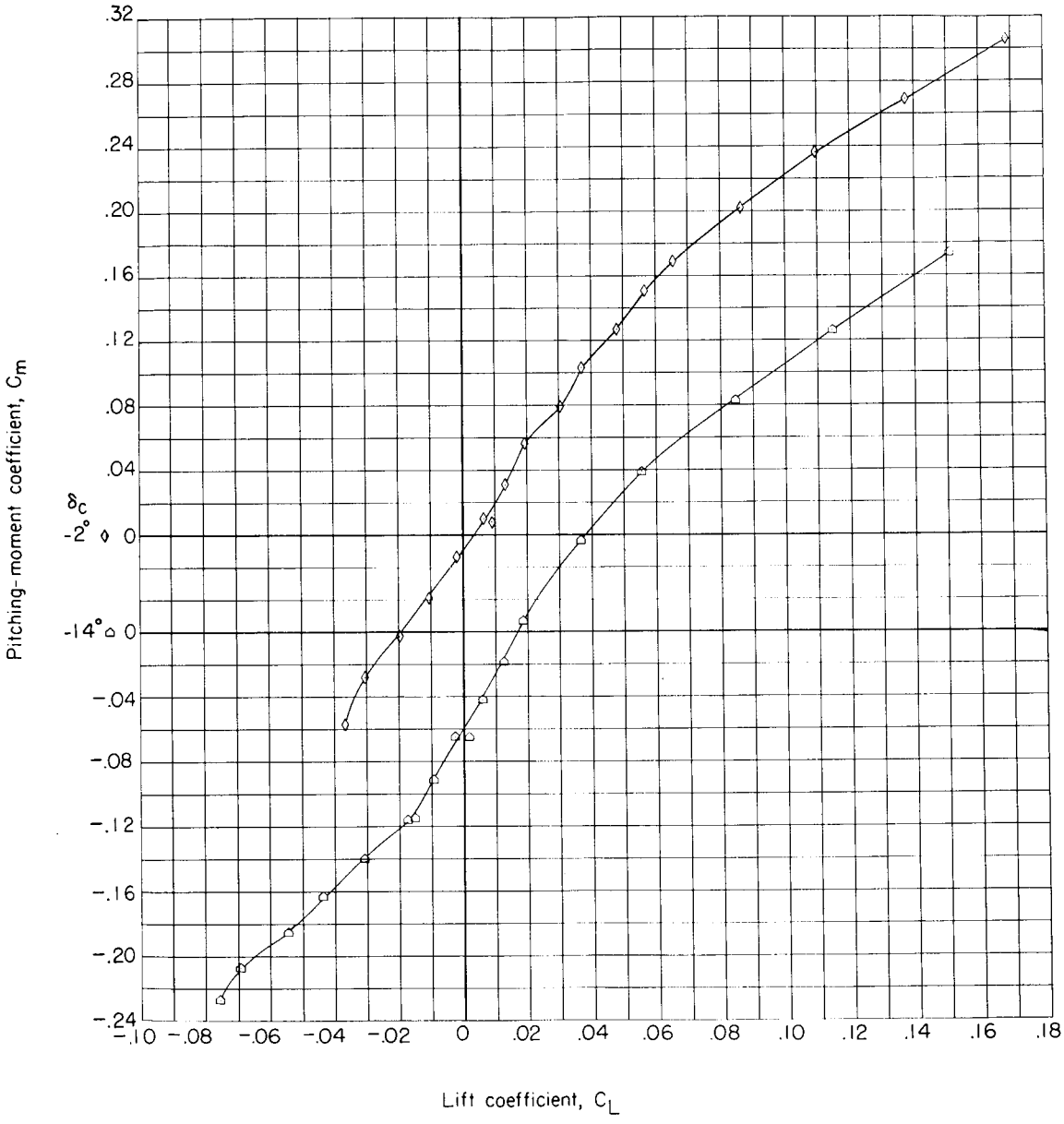

(c) Pitching-moment coefficient.

Figure 36.- Concluded.

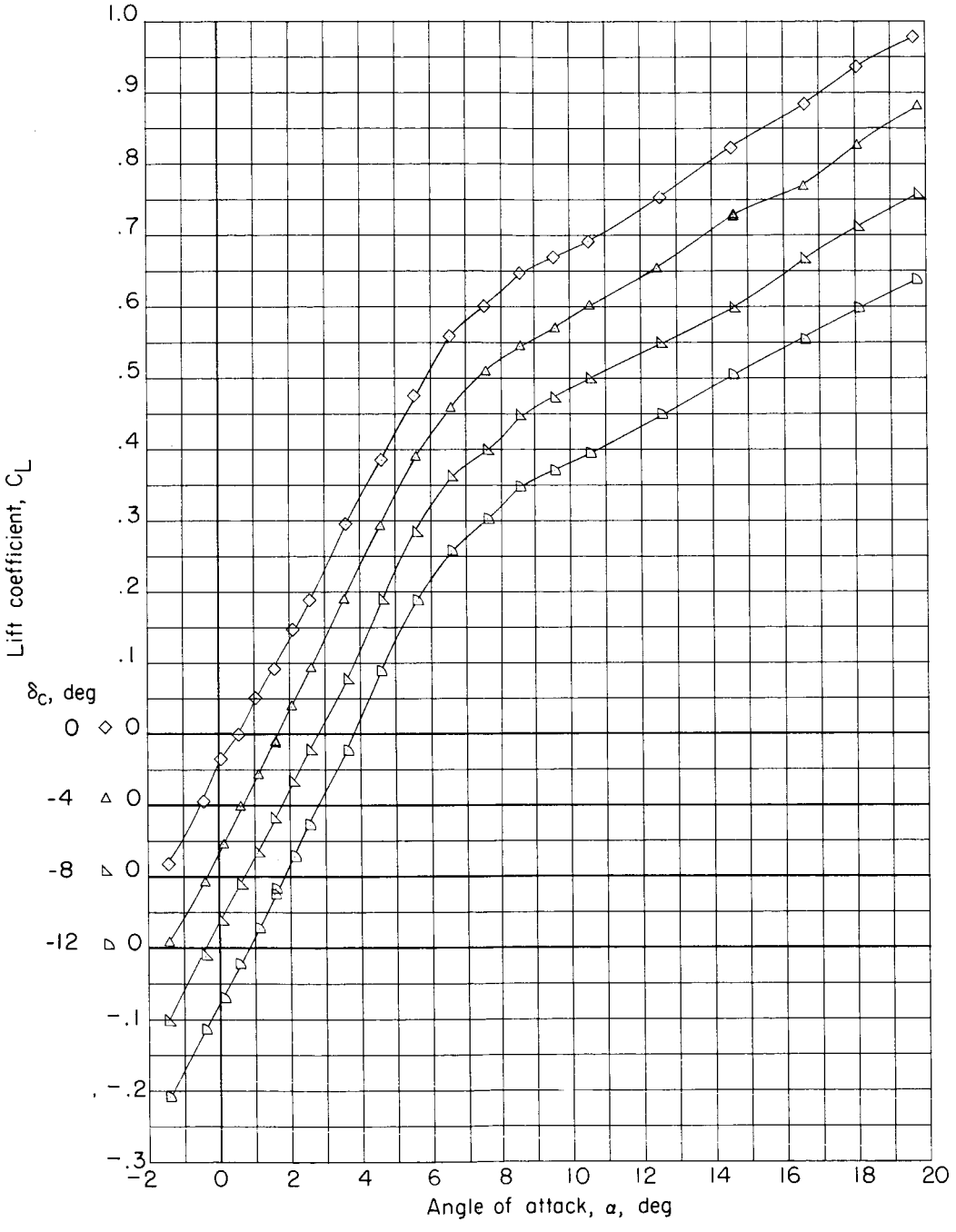

(a) Lift coefficient.

Figure 37.- Aerodynamic characteristics for configuration BCWE with $\delta_{le} = 12^\circ$ and $\delta_{tab} = 0^\circ$ at M = 0.80.

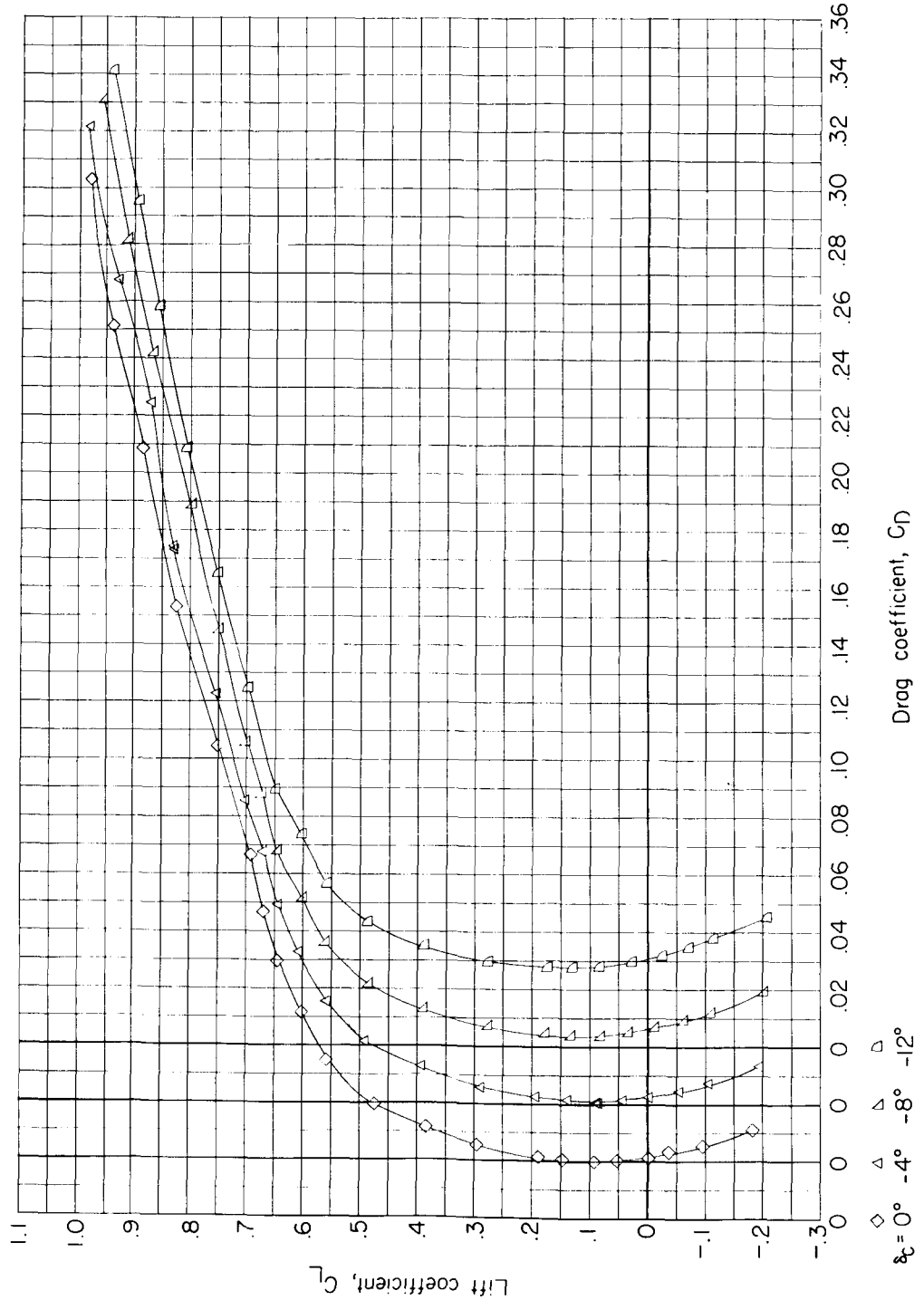

(b) Drag coefficient.

Figure 37.- Continued.

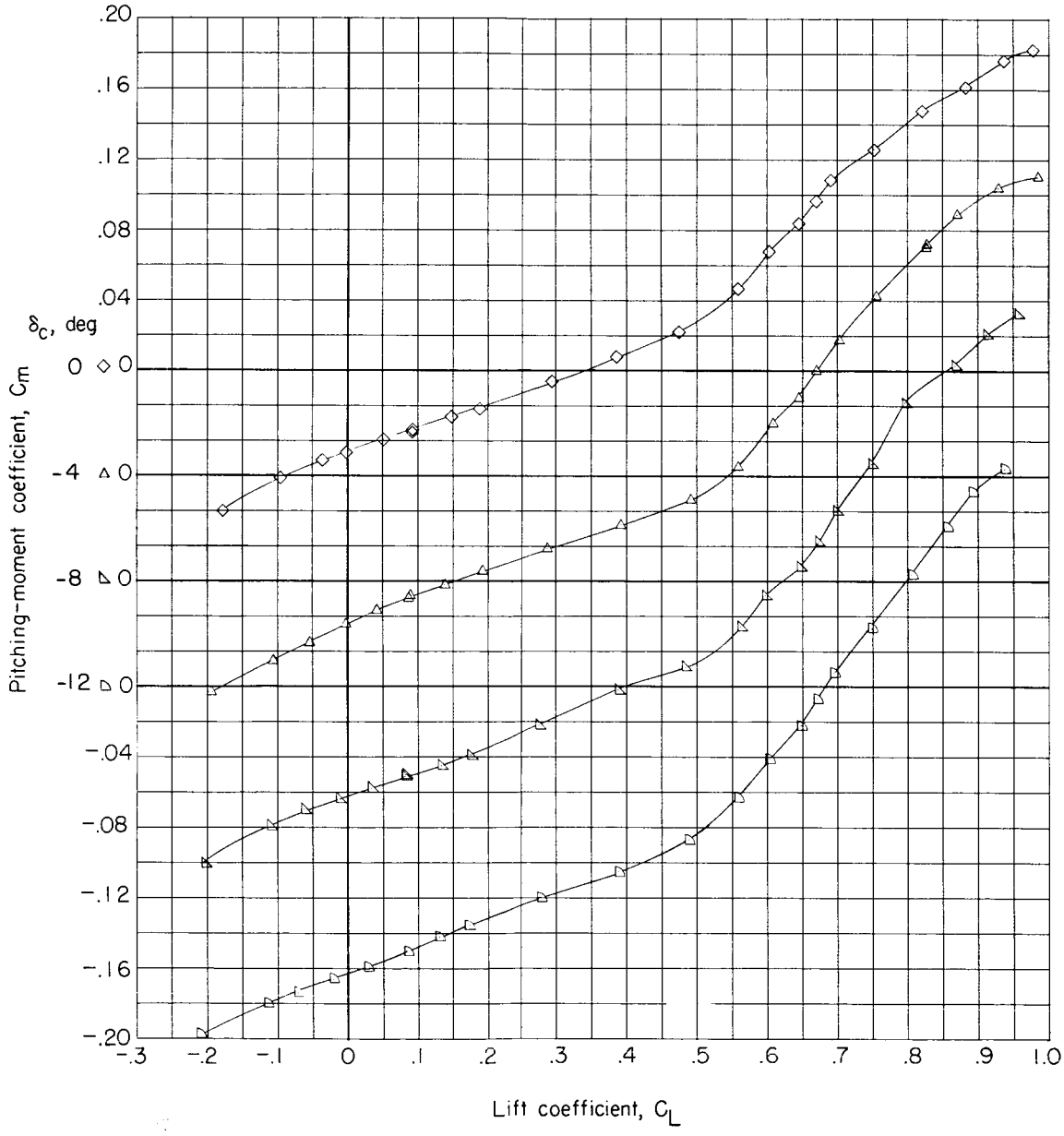

(c) Pitching-moment coefficient.

Figure 37.- Concluded.

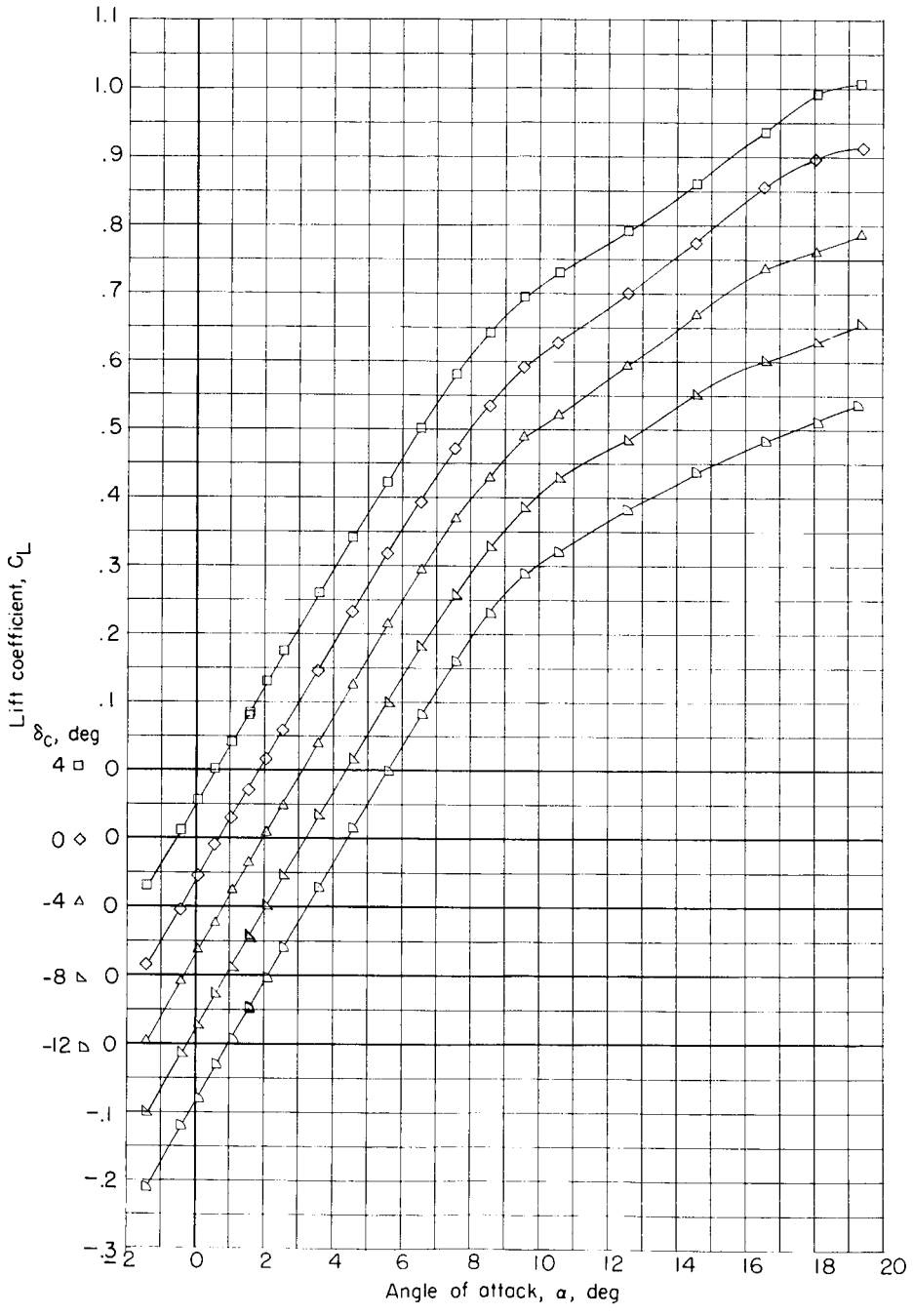

(a) Lift coefficient.

Figure 38.- Aerodynamic characteristics for configuration BCWE with $\delta_{le} = 12^\circ$ and $\delta_{tab} = -4^\circ$ at M = 0.60.

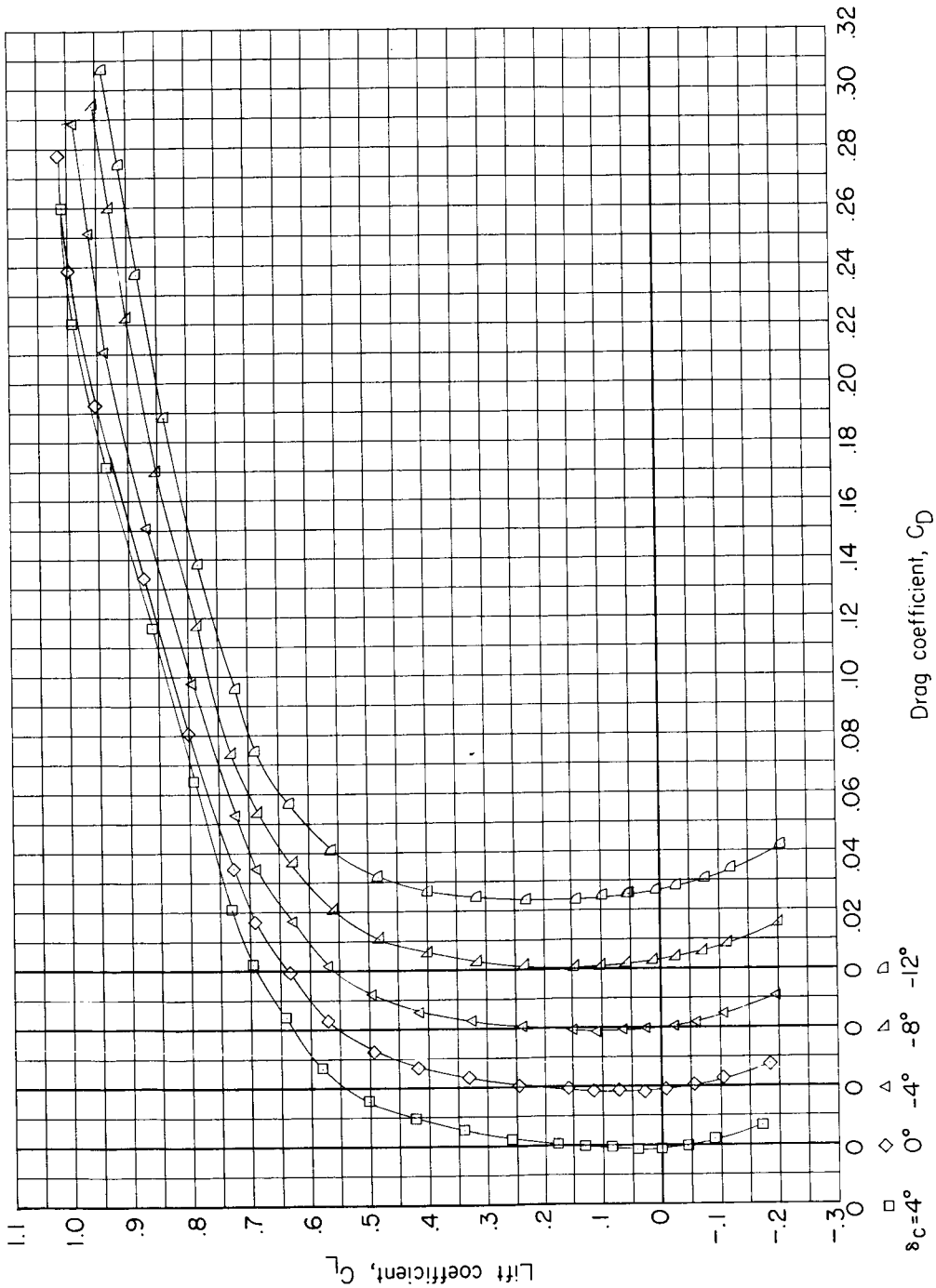

(b) Drag coefficient.

Figure 38.- Continued.

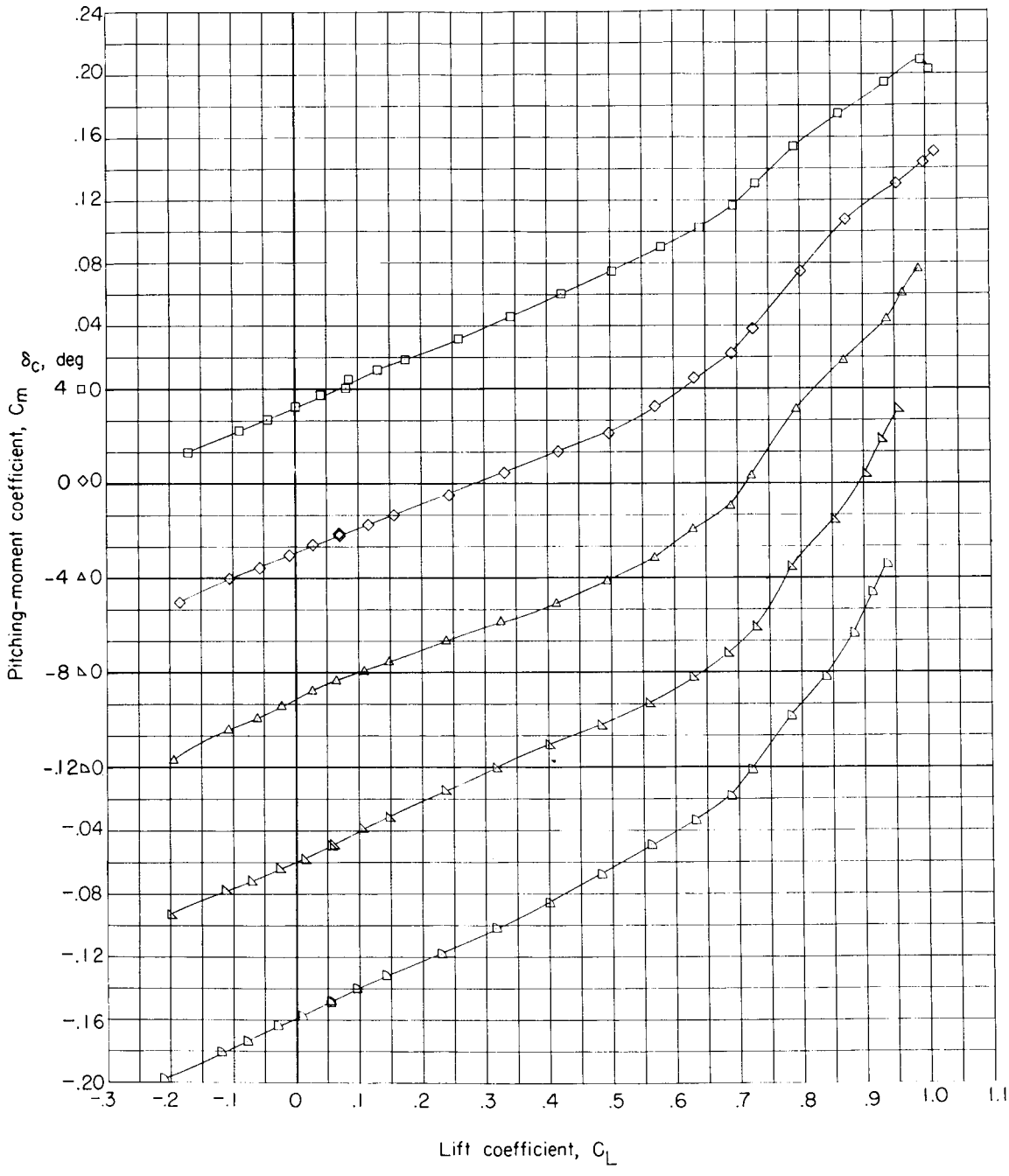

(c) Pitching-moment coefficient.

Figure 38.- Concluded.

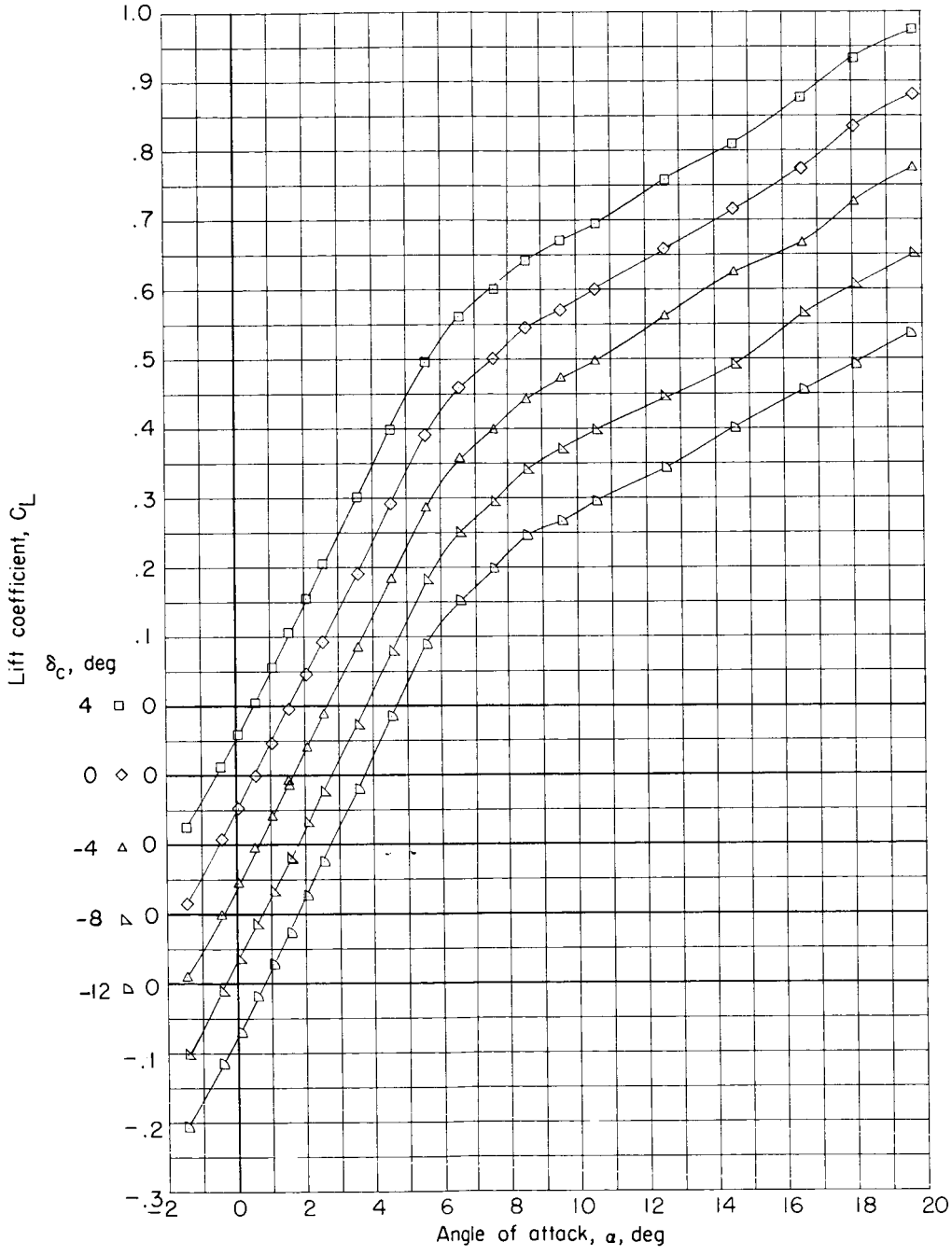

(a) Lift coefficient.

Figure 39.- Aerodynamic characteristics for configuration BCWE with $\delta_{le} = 12^\circ$ and $\delta_{tab} = -4^\circ$ at M = 0.80.

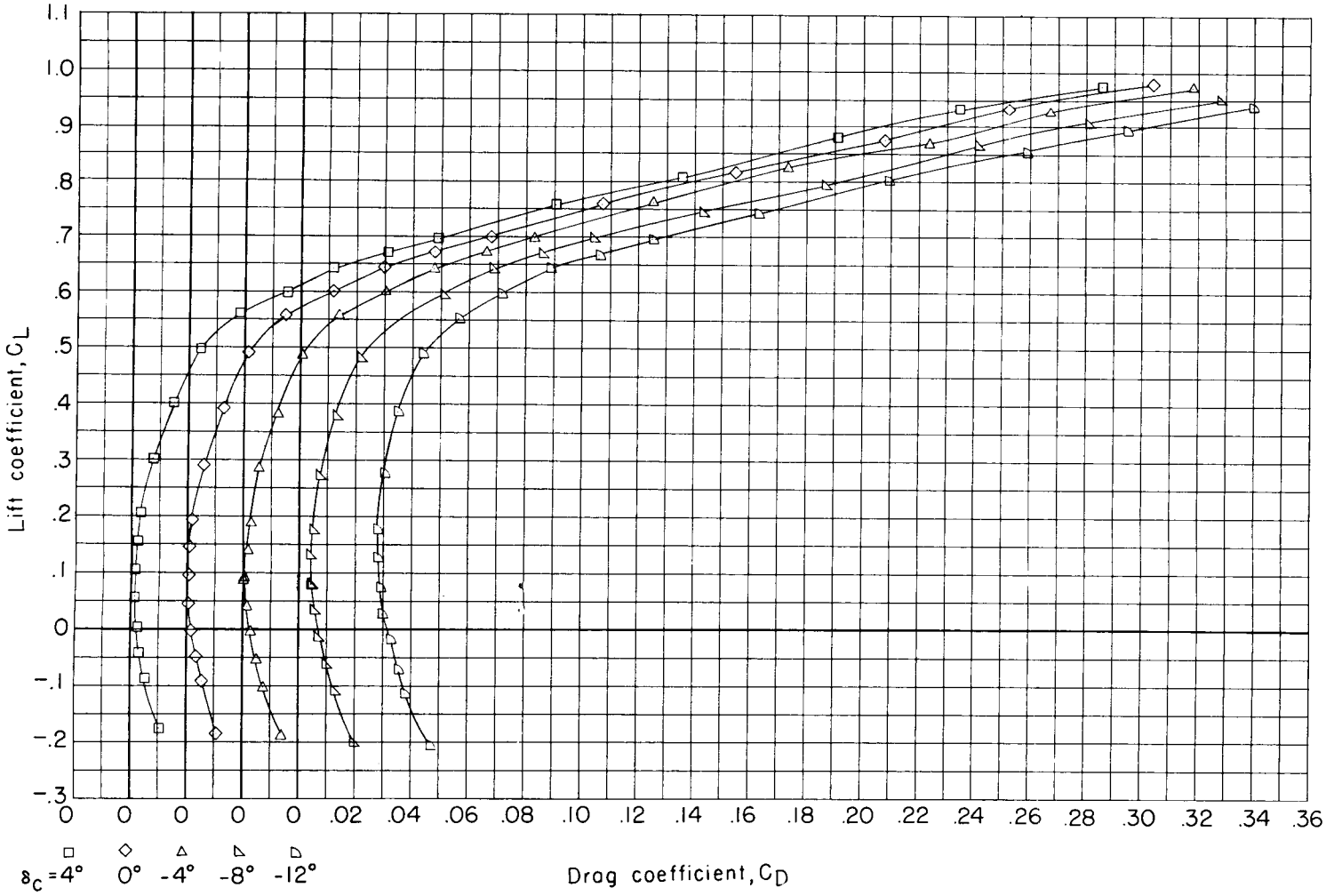

(b) Drag coefficient.

Figure 39.- Continued.

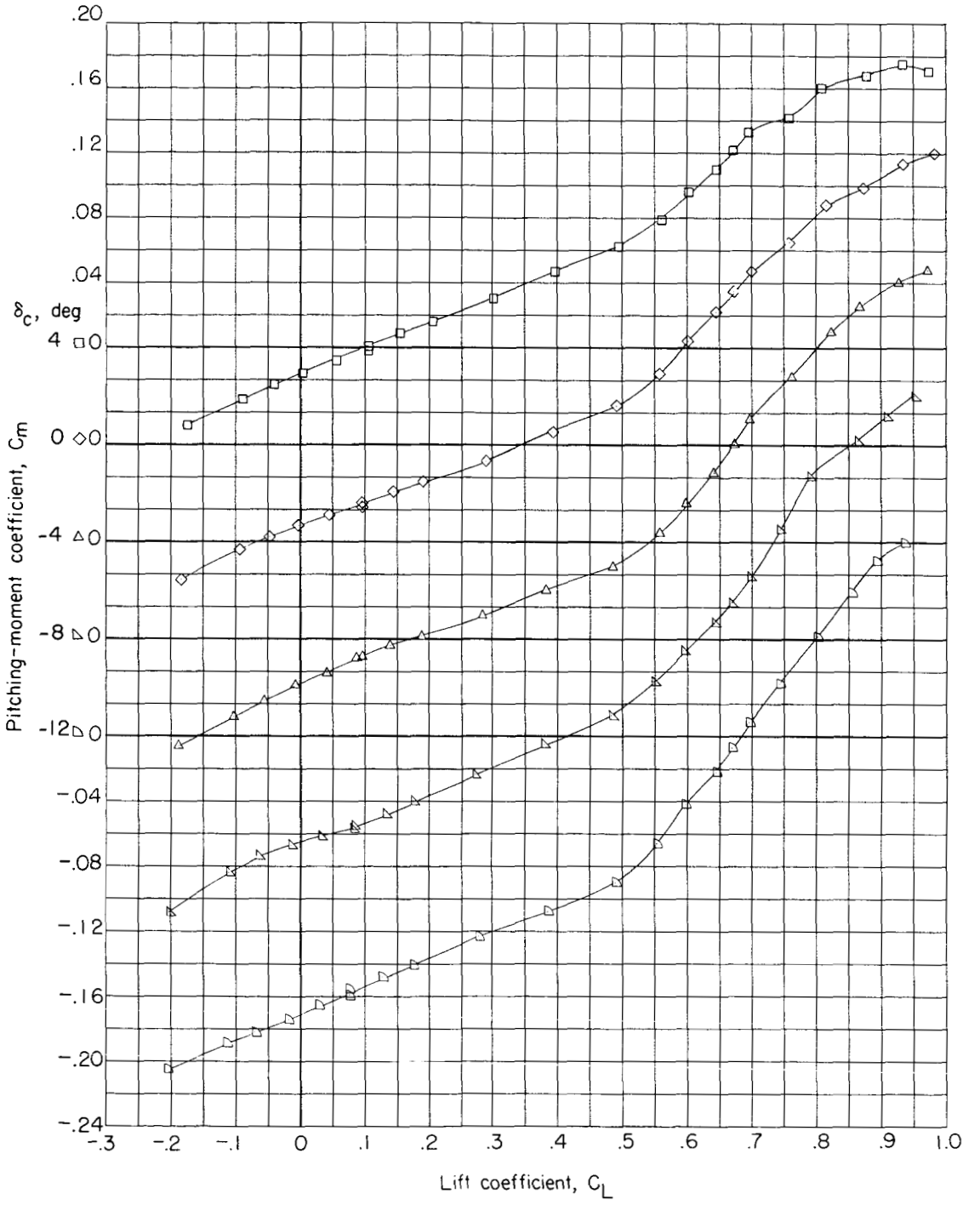

(c) Pitching-moment coefficient.

Figure 39.- Concluded.

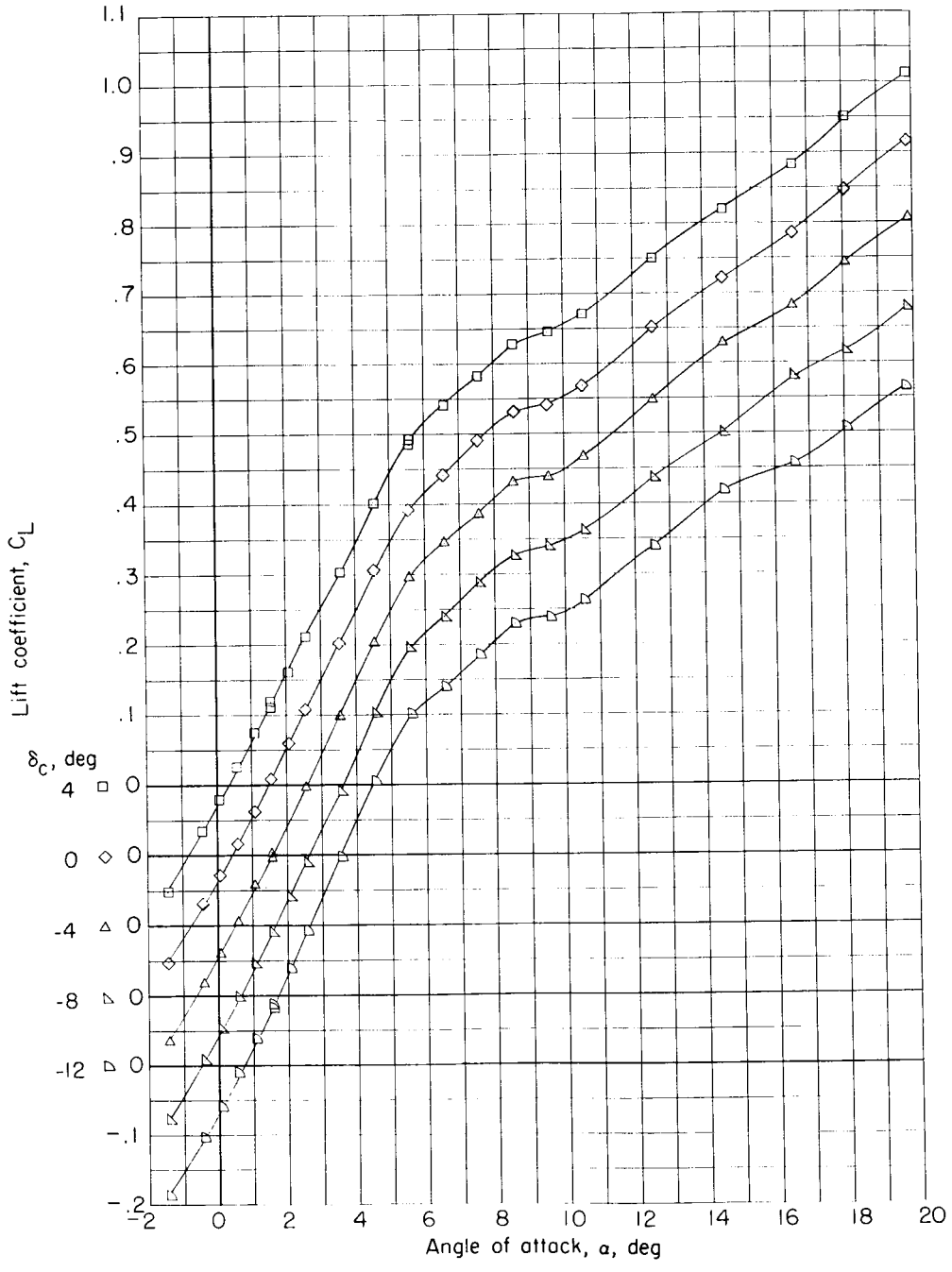

(a) Lift coefficient.

Figure 40.- Aerodynamic characteristics for configuration BCWE with $\delta_{le} = 12^{\circ}$ and $\delta_{tab} = -4^{\circ}$ at $M = 0.85$.

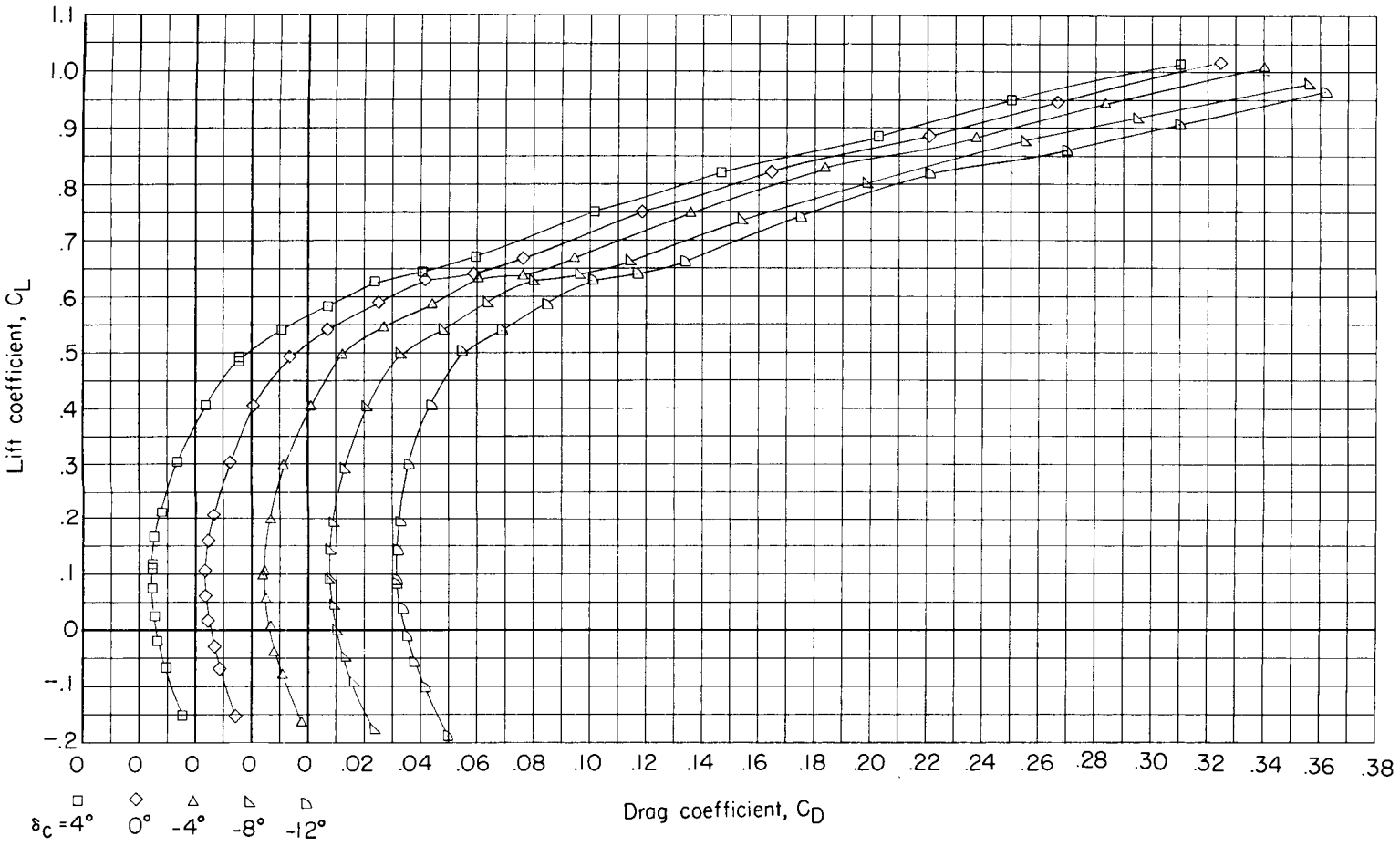

(b) Drag coefficient.

Figure 40.- Continued.

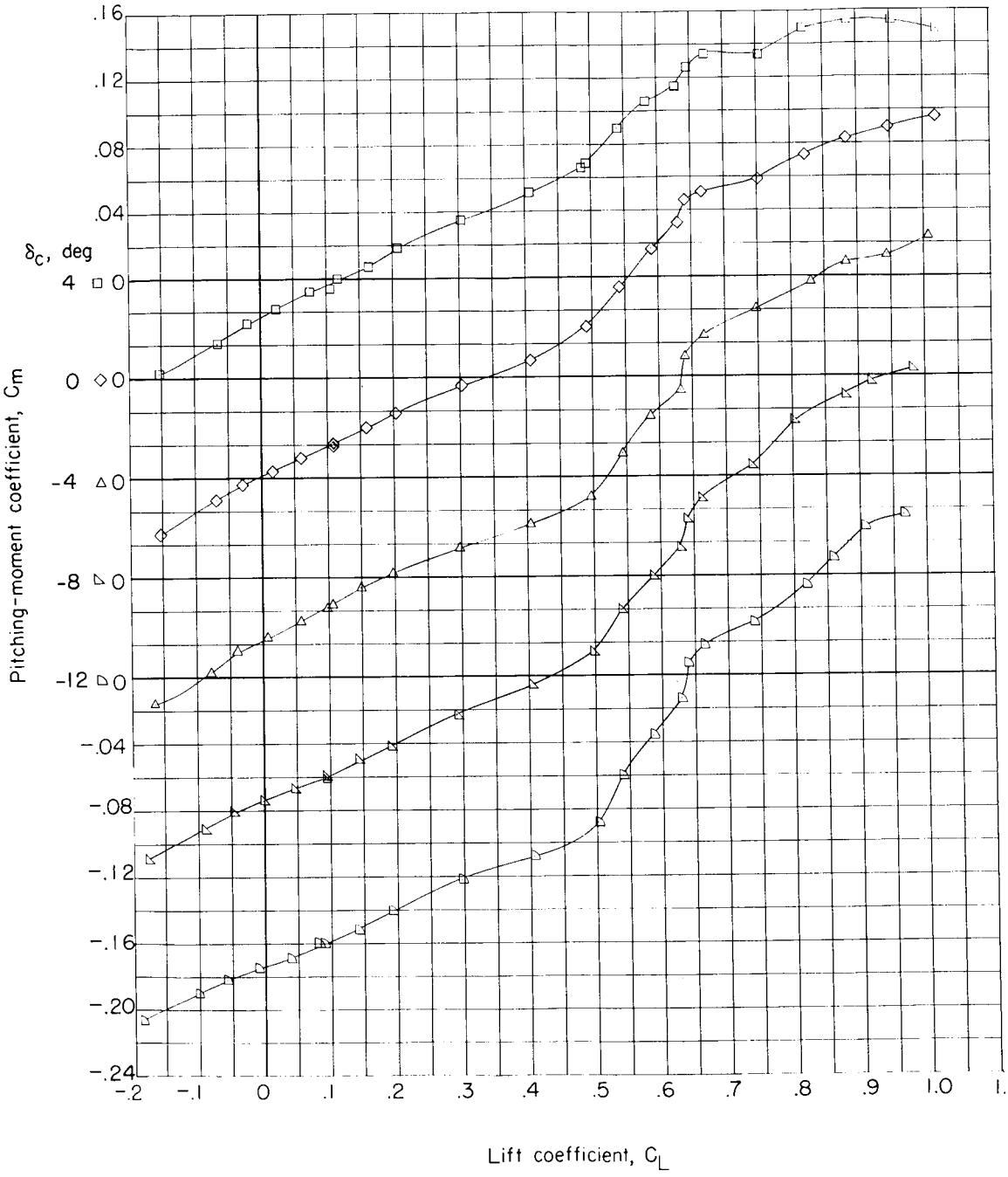

(c) Pitching-moment coefficient.

Figure 40.- Concluded.

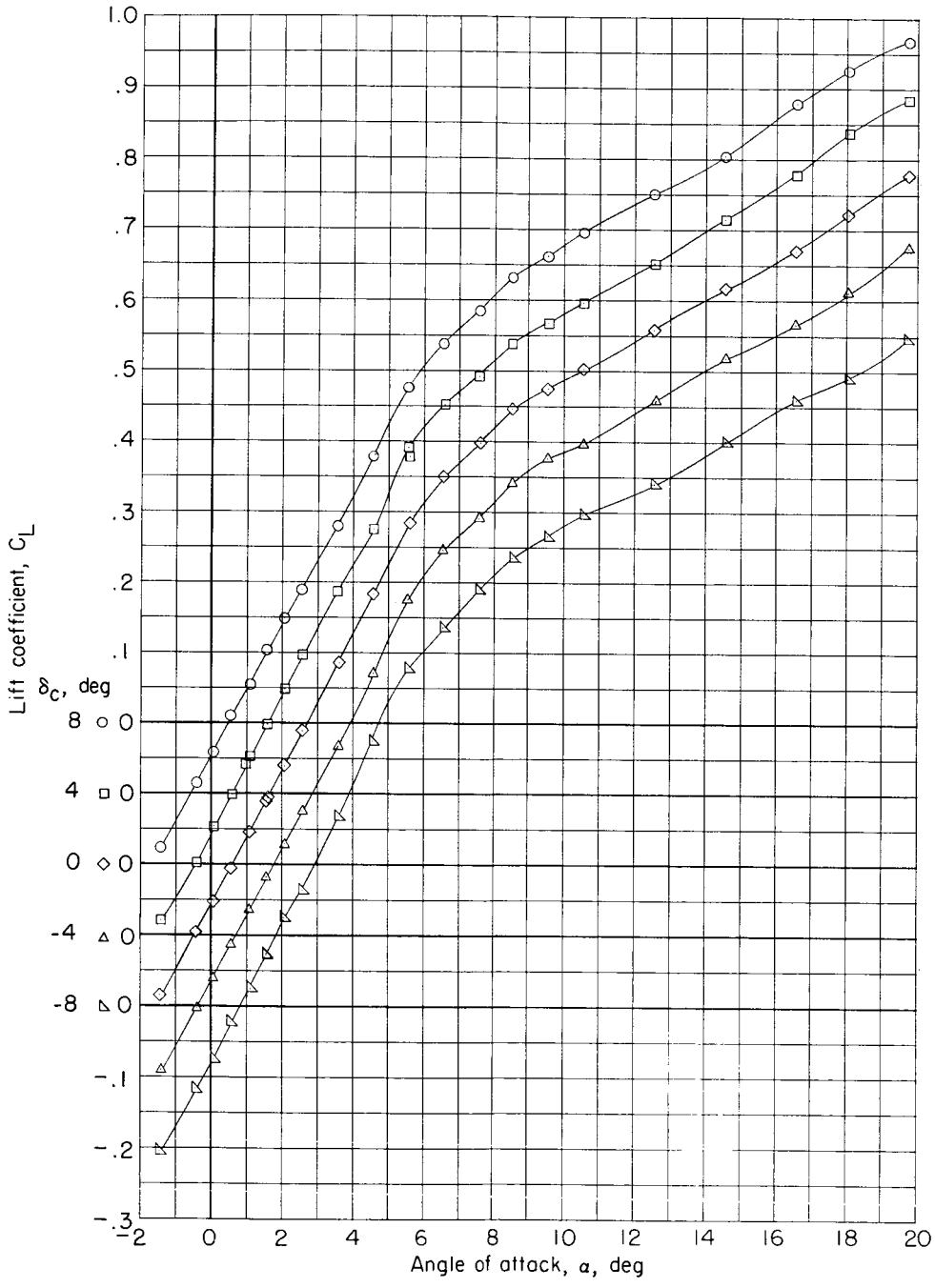

(a) Lift coefficient.

Figure 41.- Aerodynamic characteristics for configuration BCWE with $\delta_{le} = 12^{\circ}$ and $\delta_{tab} = -8^{\circ}$ at M = 0.80.

(b) Drag coefficient.

Figure 41.- Continued.

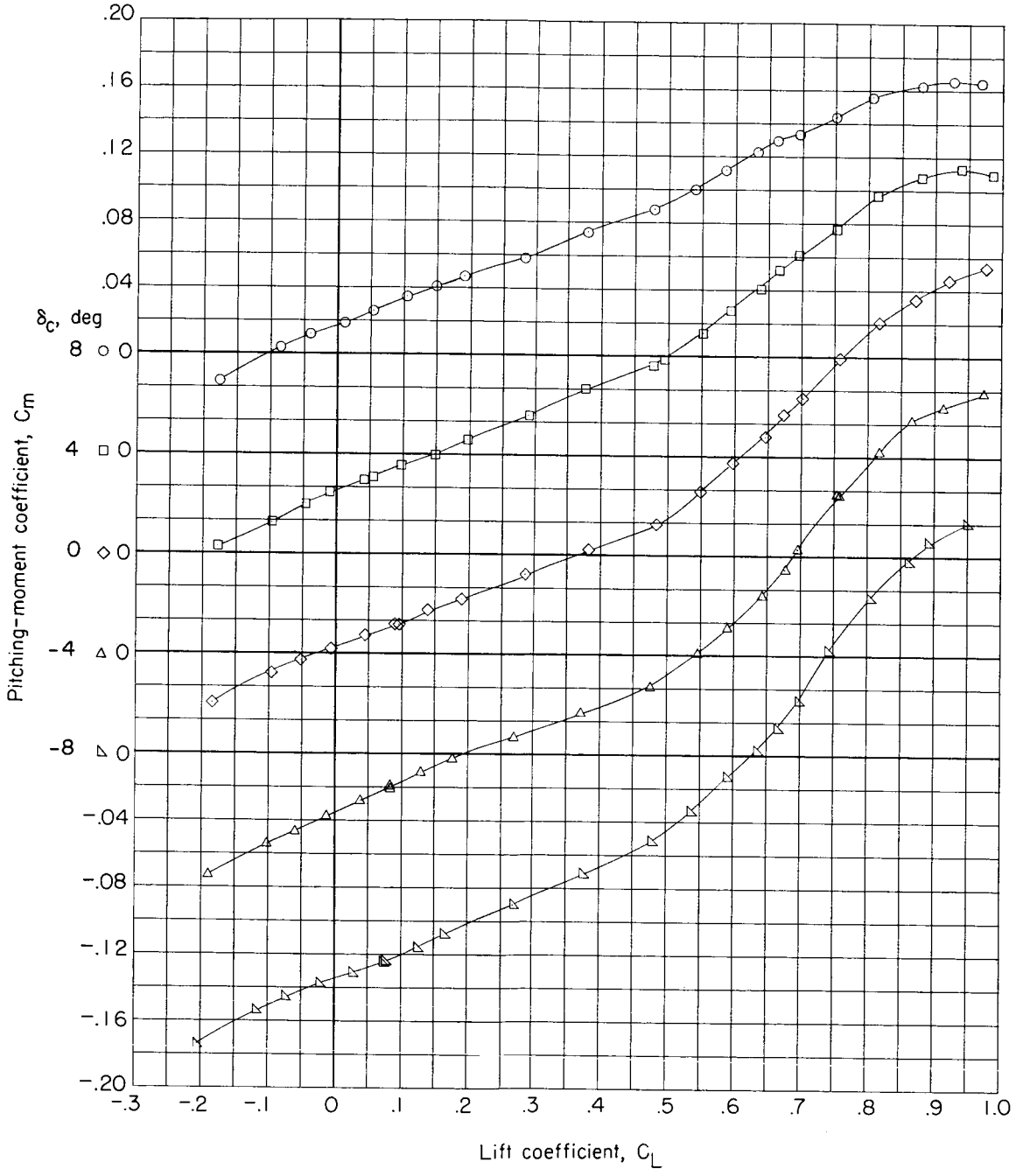

(c) Pitching-moment coefficient.

Figure 41.- Concluded.

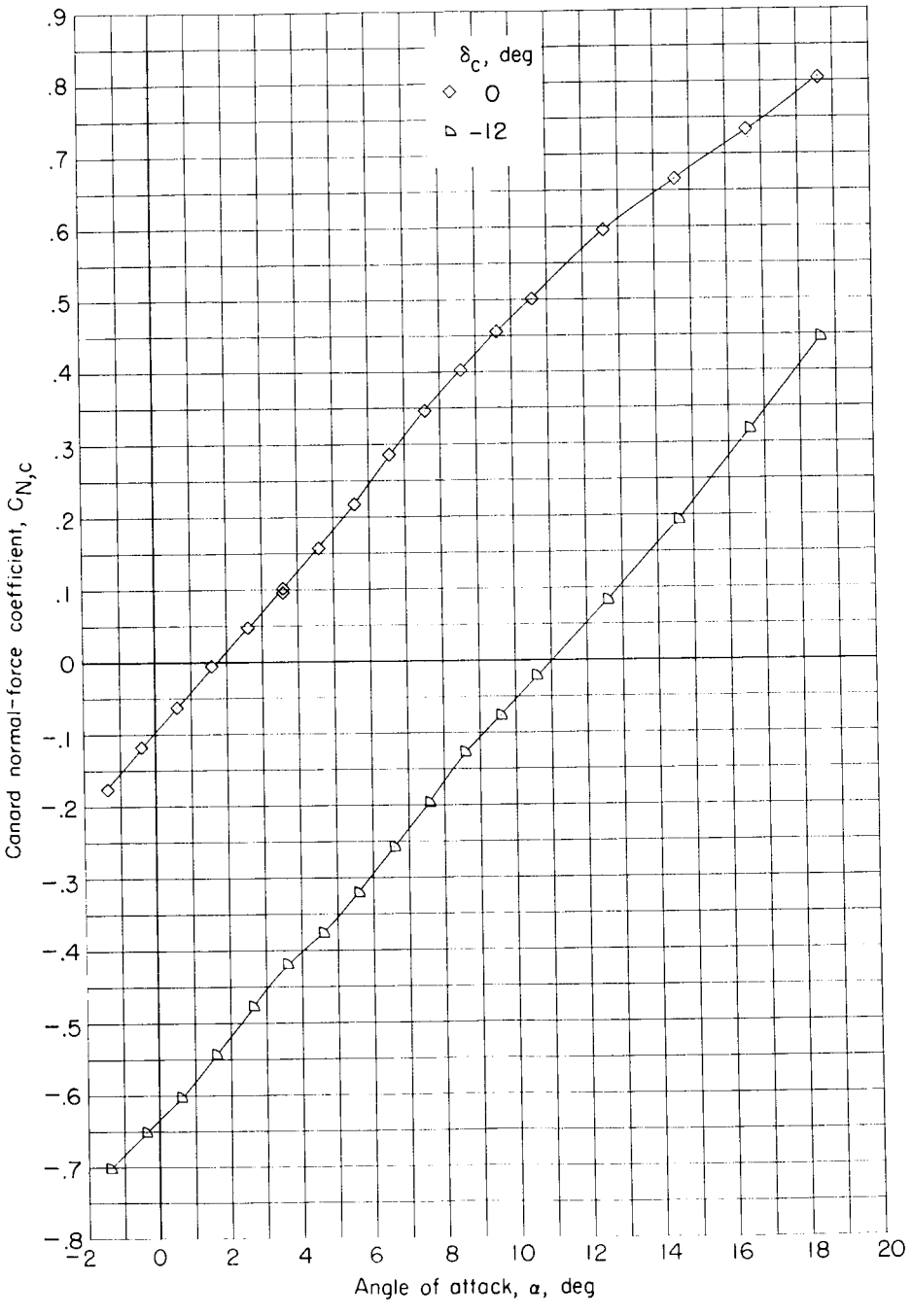

(a) Canard normal-force coefficient.

Figure 42.- Canard normal-force and hinge-moment coefficients for configuration BC with $\delta_{tab} = 0^{\circ}$ at M = 0.80.

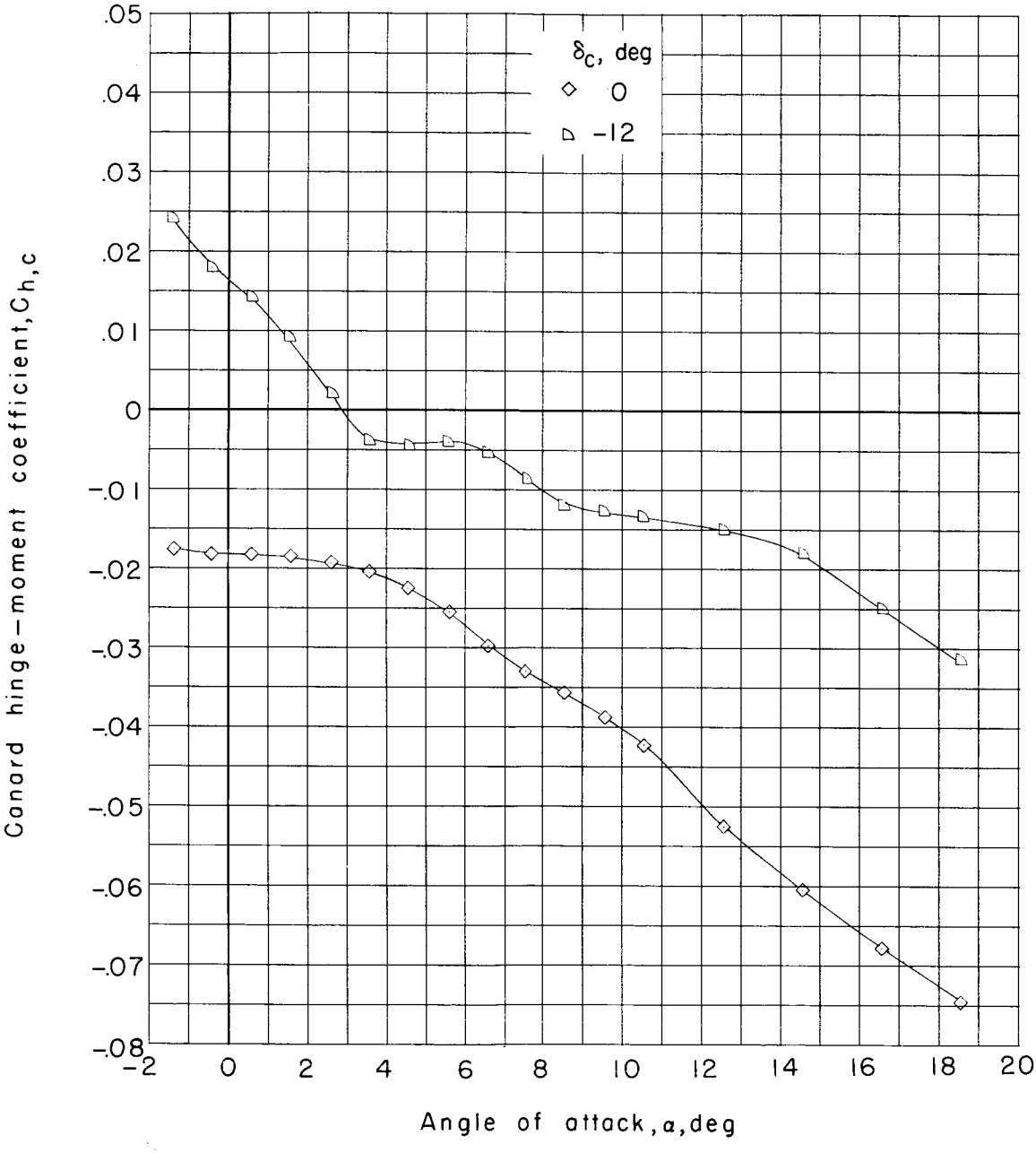

(b) Canard hinge-moment coefficient.

Figure 42.- Concluded.

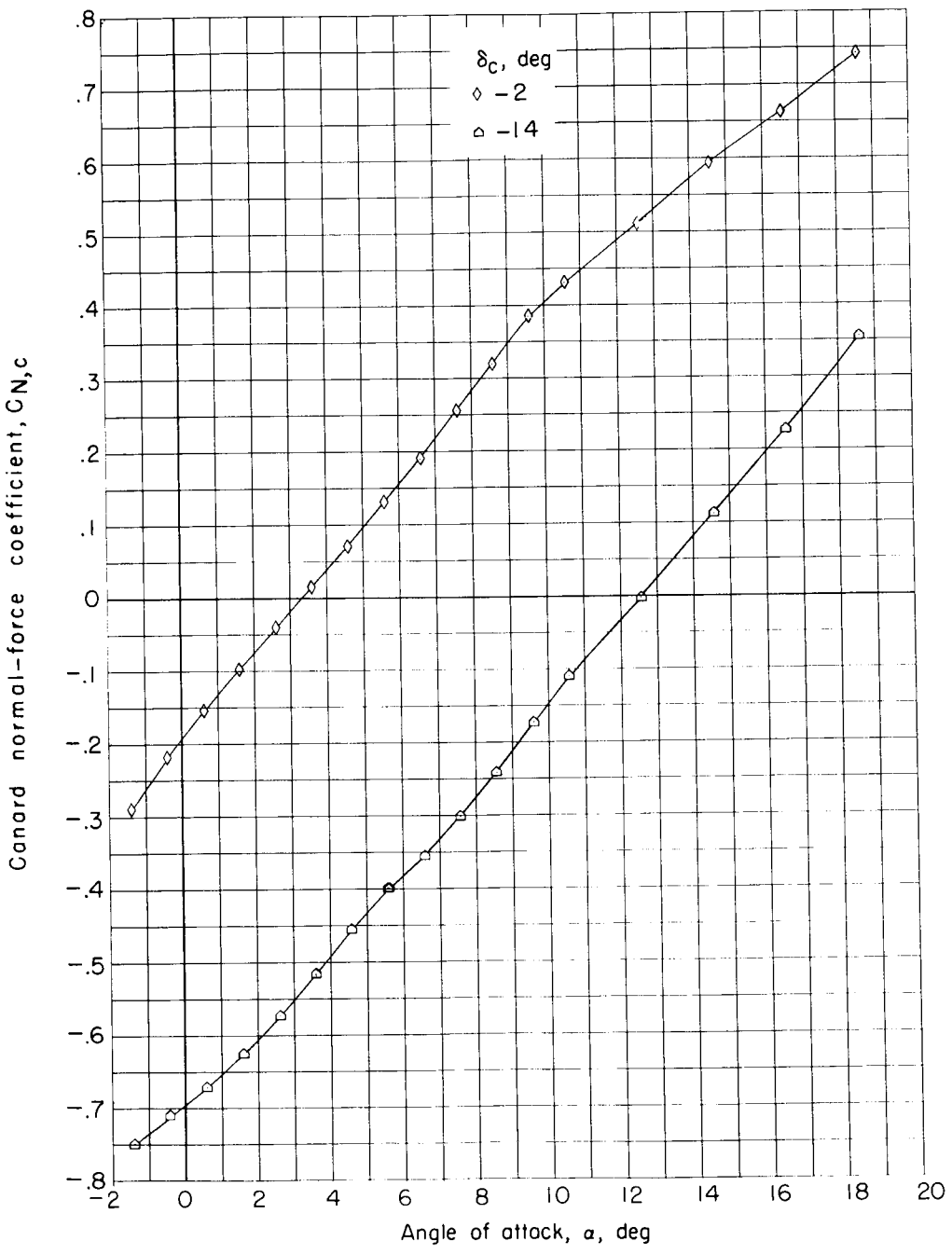

(a) Canard normal-force coefficient.

Figure 43.- Canard normal-force and hinge-moment coefficients for configuration BC with $\delta_{tab} = 0^\circ$ at $M = 0.85$.

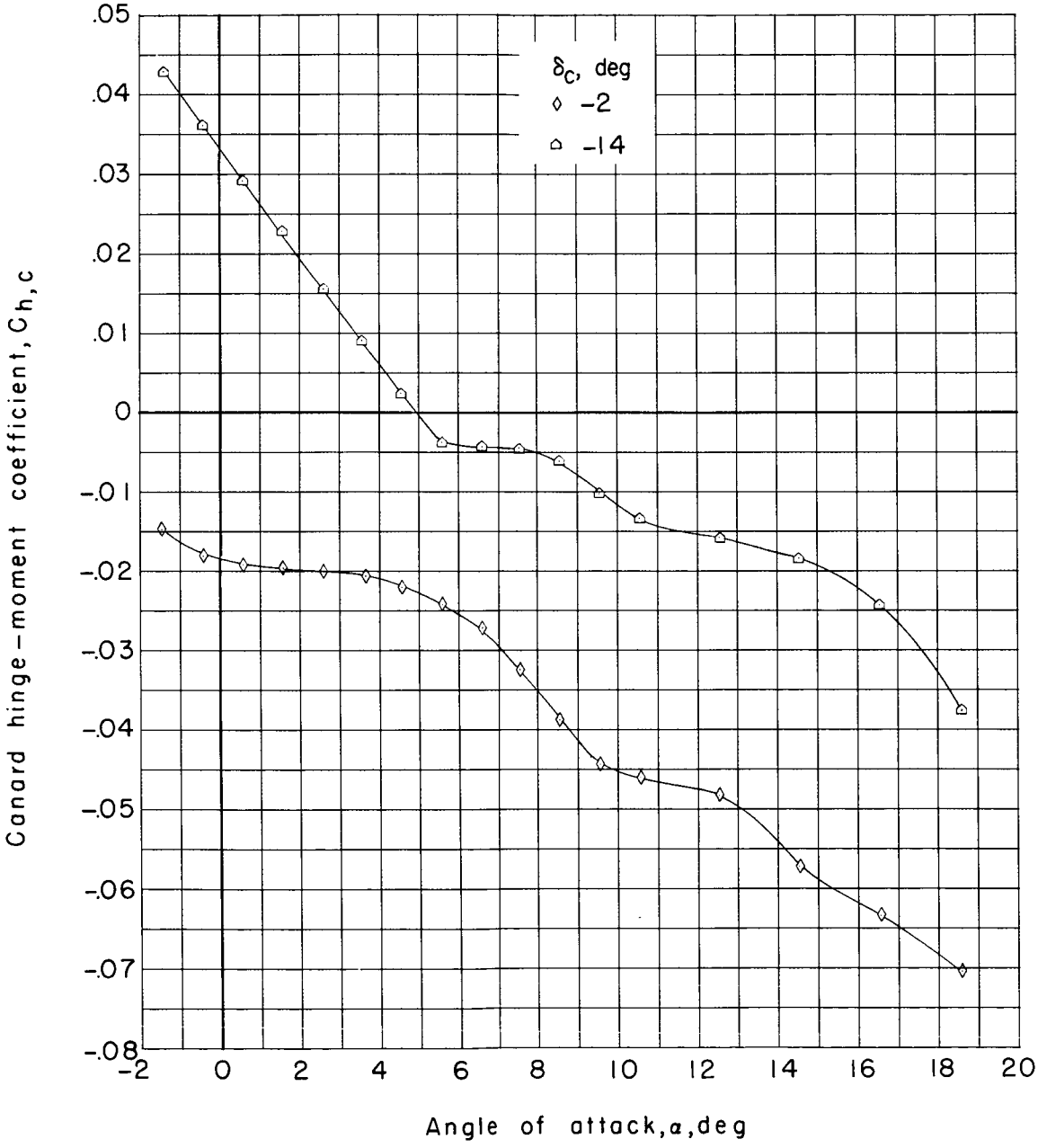

(b) Canard hinge-moment coefficient.

Figure 43.- Concluded.

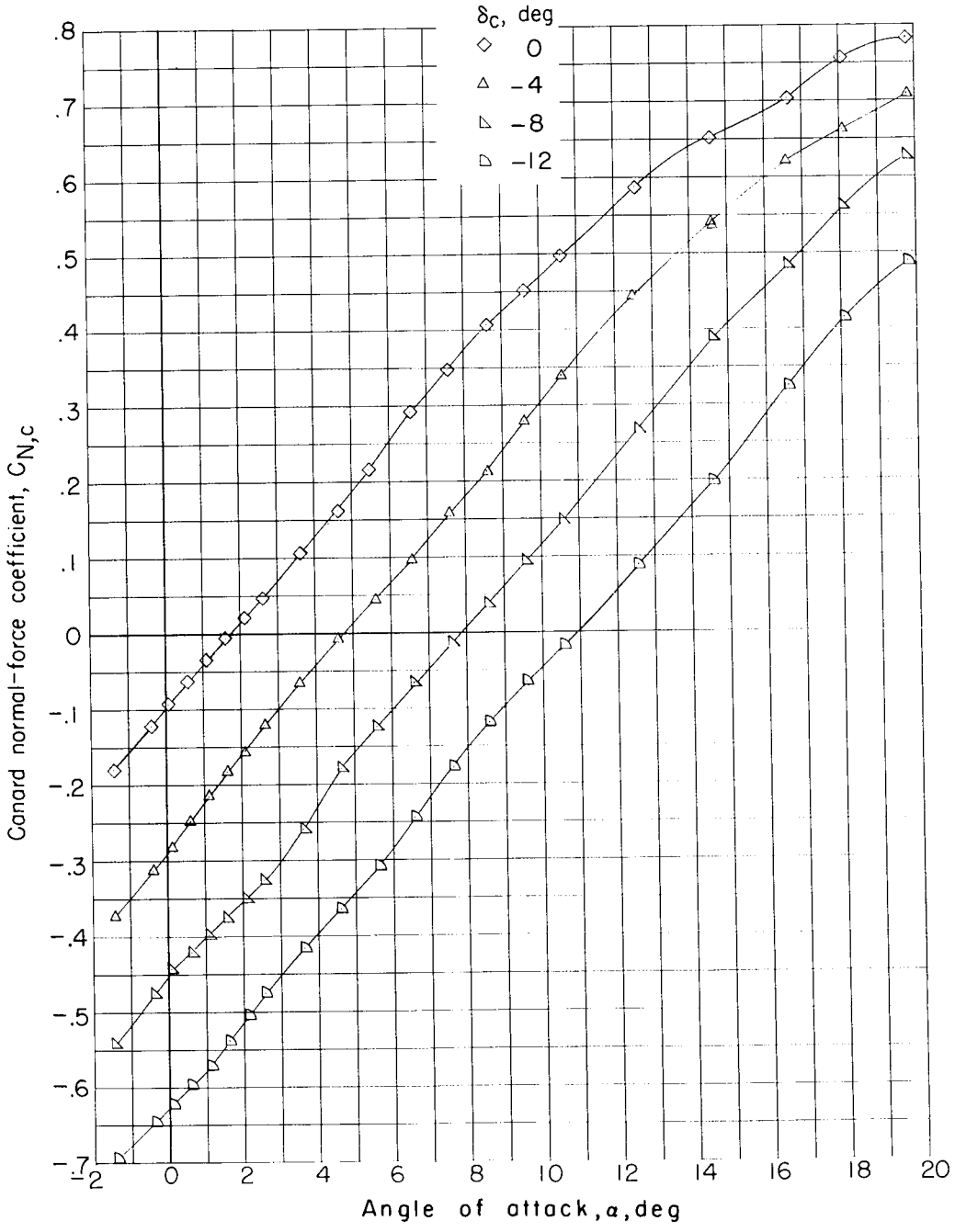

(a) Canard normal-force coefficient.

Figure 44.- Canard normal-force and hinge-moment coefficients for configuration BCWE with $\delta_{le} = 12^{\circ}$ and $\delta_{tab} = 0^{\circ}$ at M = 0.80.

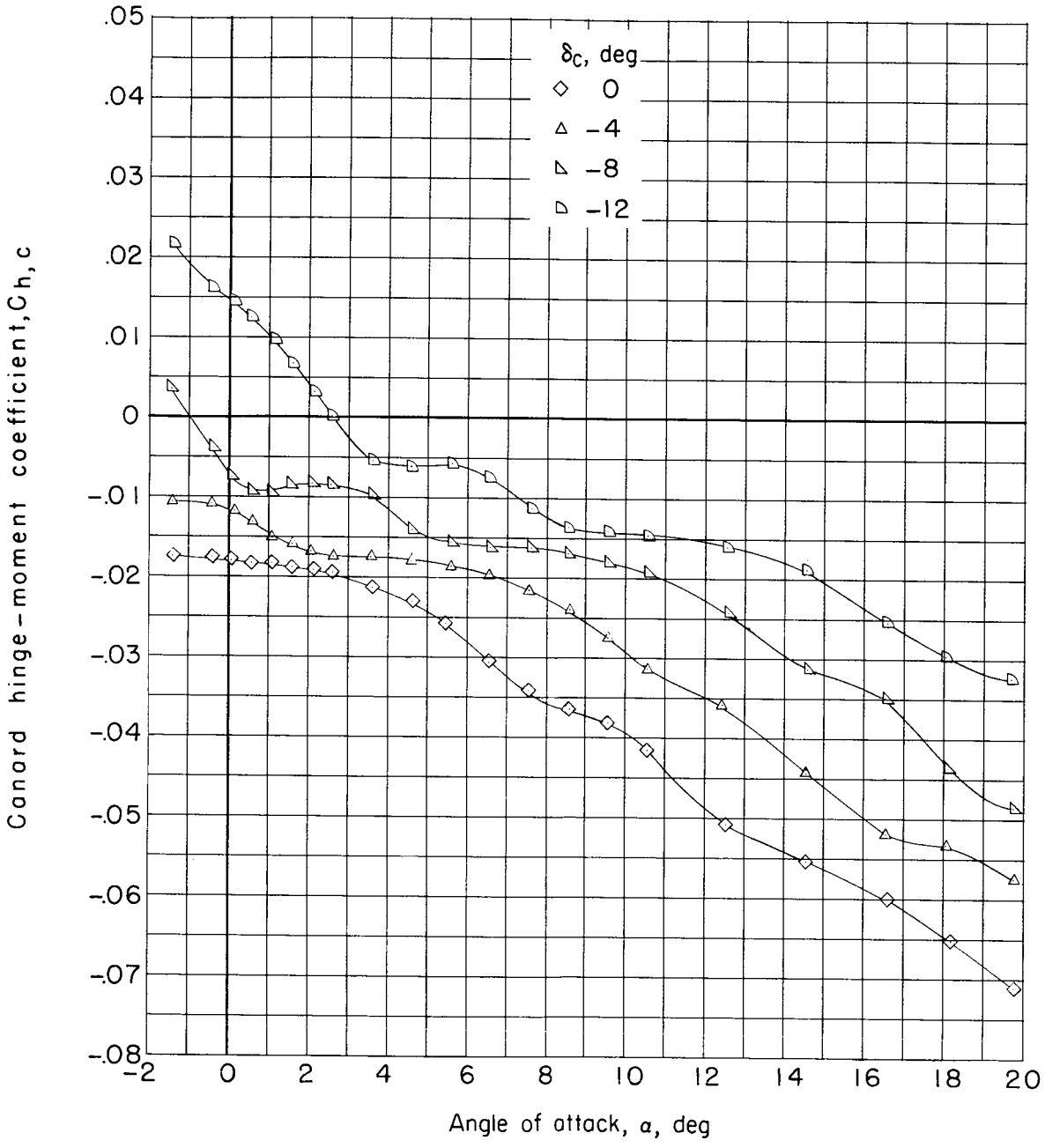

(b) Canard hinge-moment coefficient.

Figure 44.- Concluded.

L-1040

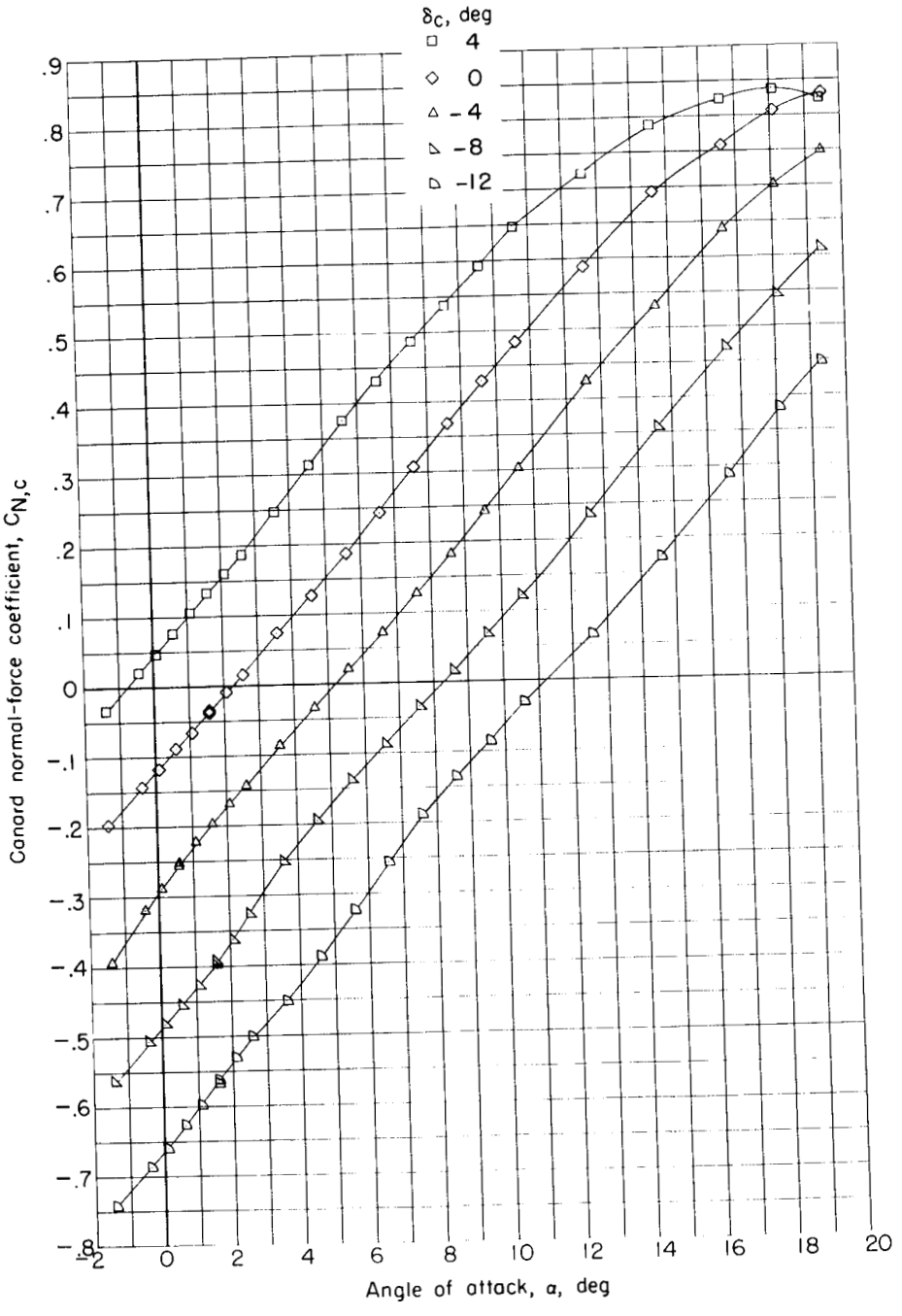

(a) Canard normal-force coefficient.

Figure 45.- Canard normal-force and hinge-moment coefficients for configuration BCWE with $\delta_{le} = 12^\circ$ and $\delta_{tab} = -4^\circ$ at M = 0.60.

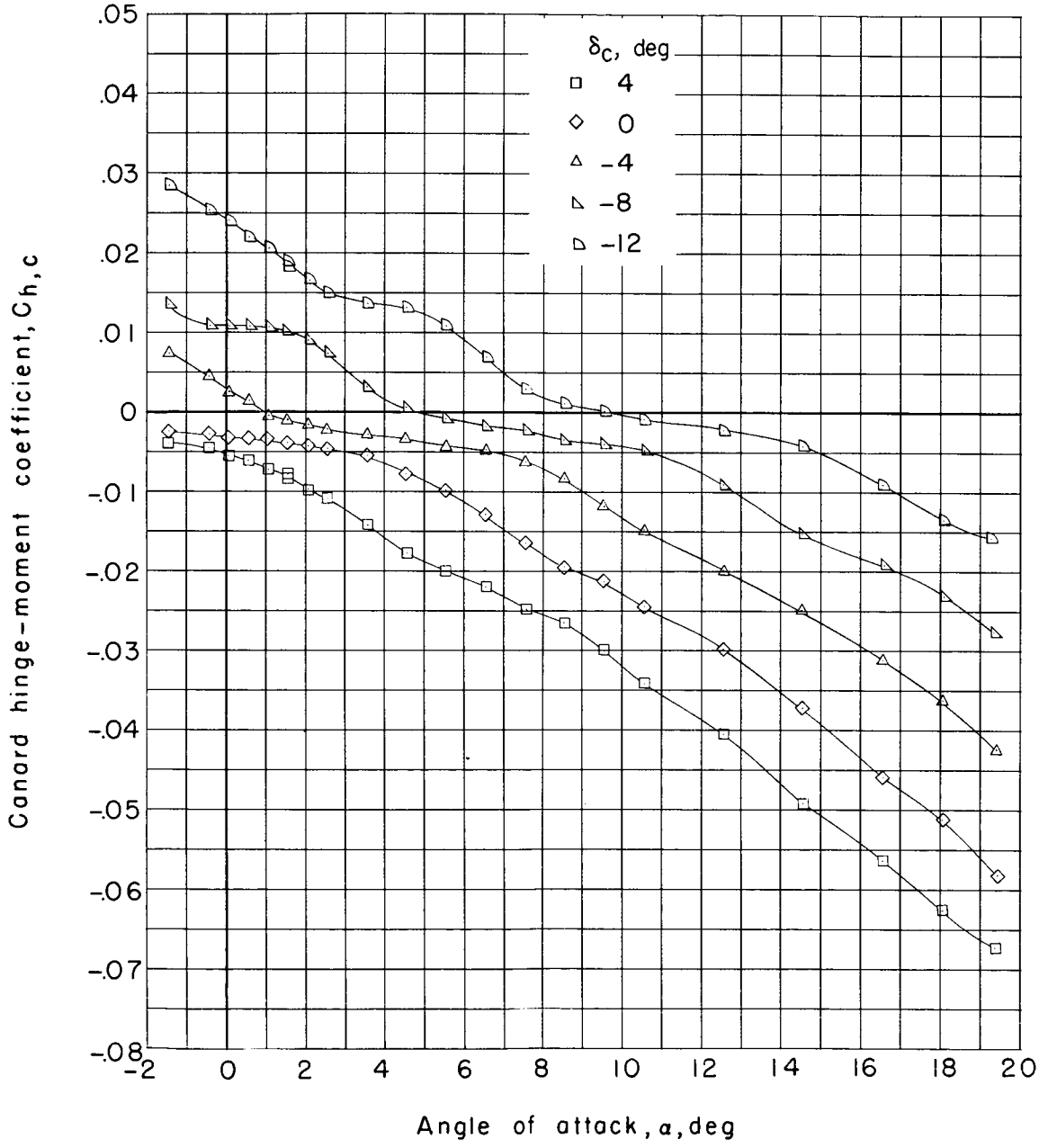

(b) Canard hinge-moment coefficient.

Figure 45.- Concluded.

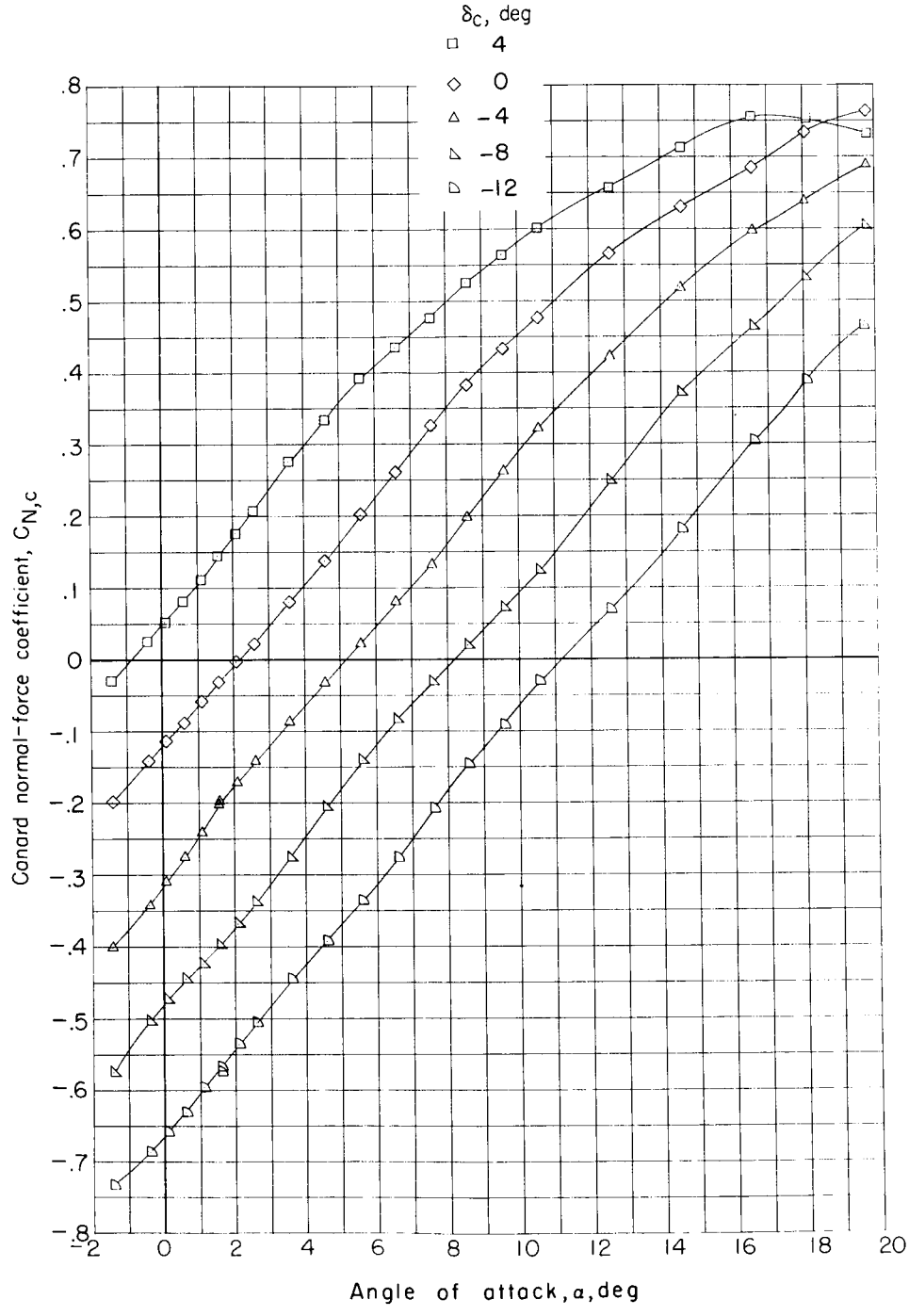

(a) Canard normal-force coefficient plotted against angle of attack.

Figure 46.- Canard normal-force and hinge-moment coefficients for configuration BCWE with $\delta_{le} = 12^\circ$ and $\delta_{tab} = -4^\circ$ at M = 0.80.

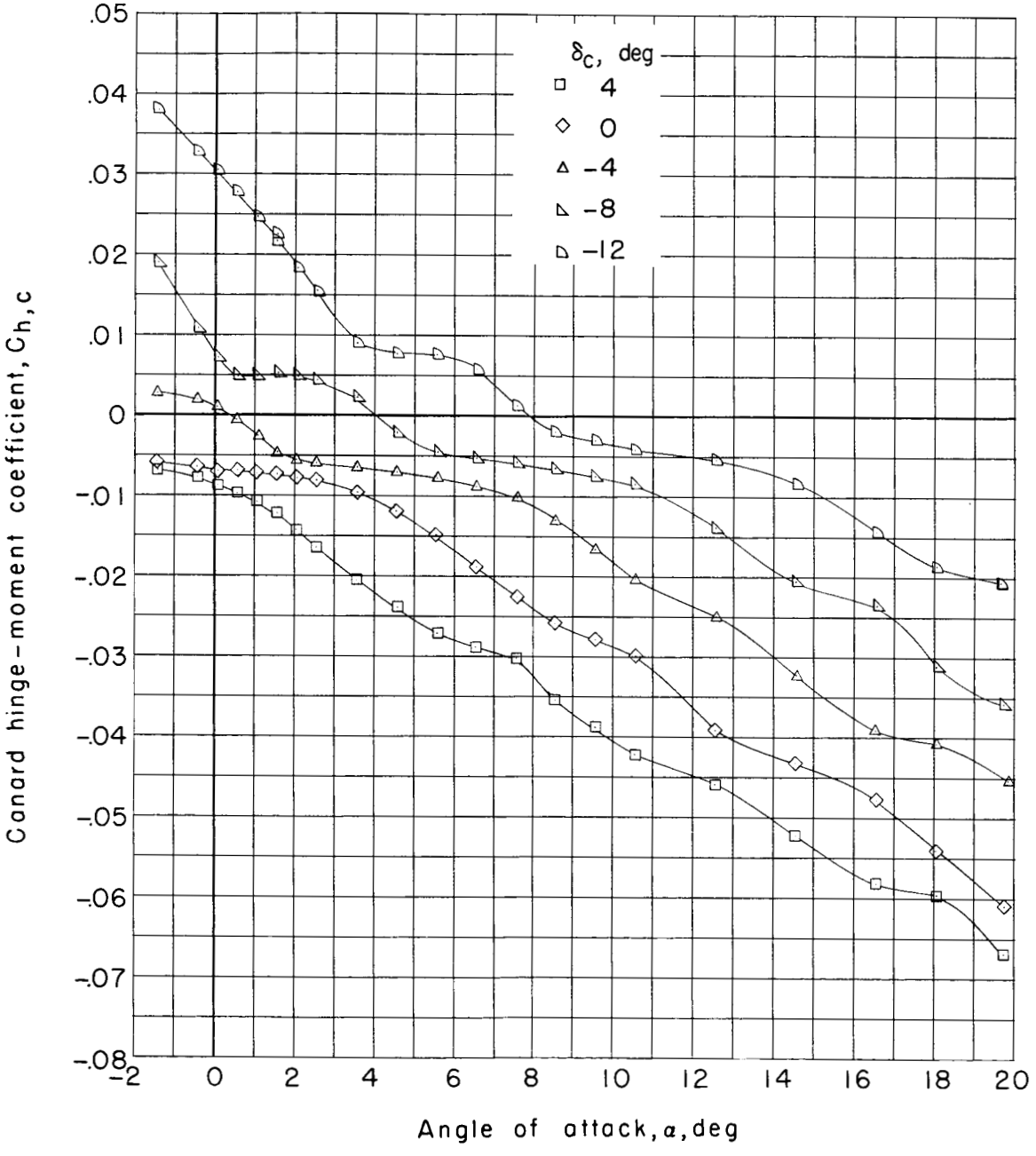

(b) Canard hinge-moment coefficient plotted against angle of attack.

Figure 46.- Continued.

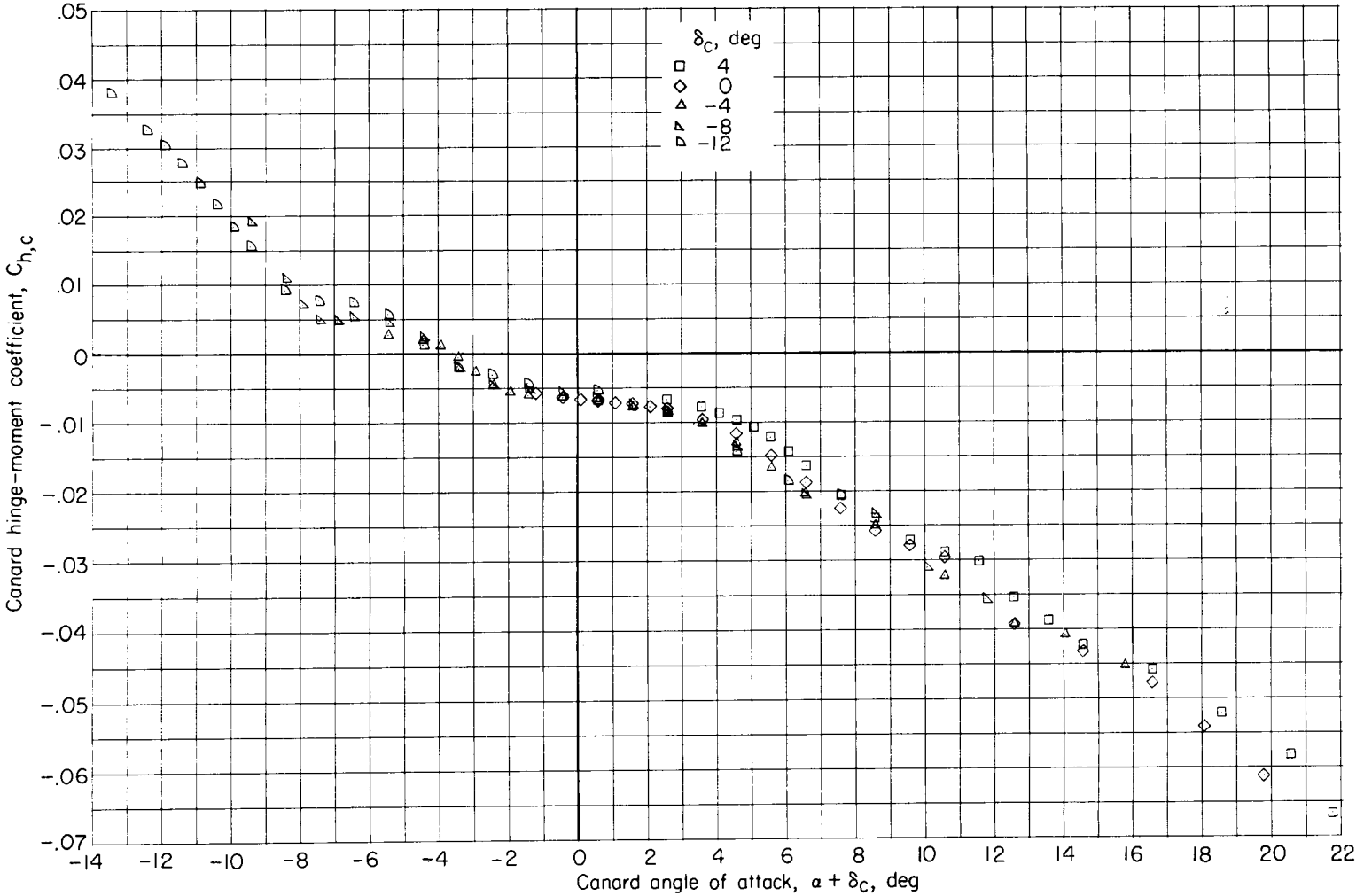

(c) Canard hinge-moment coefficient plotted against canard angle of attack.

Figure 46.- Concluded.

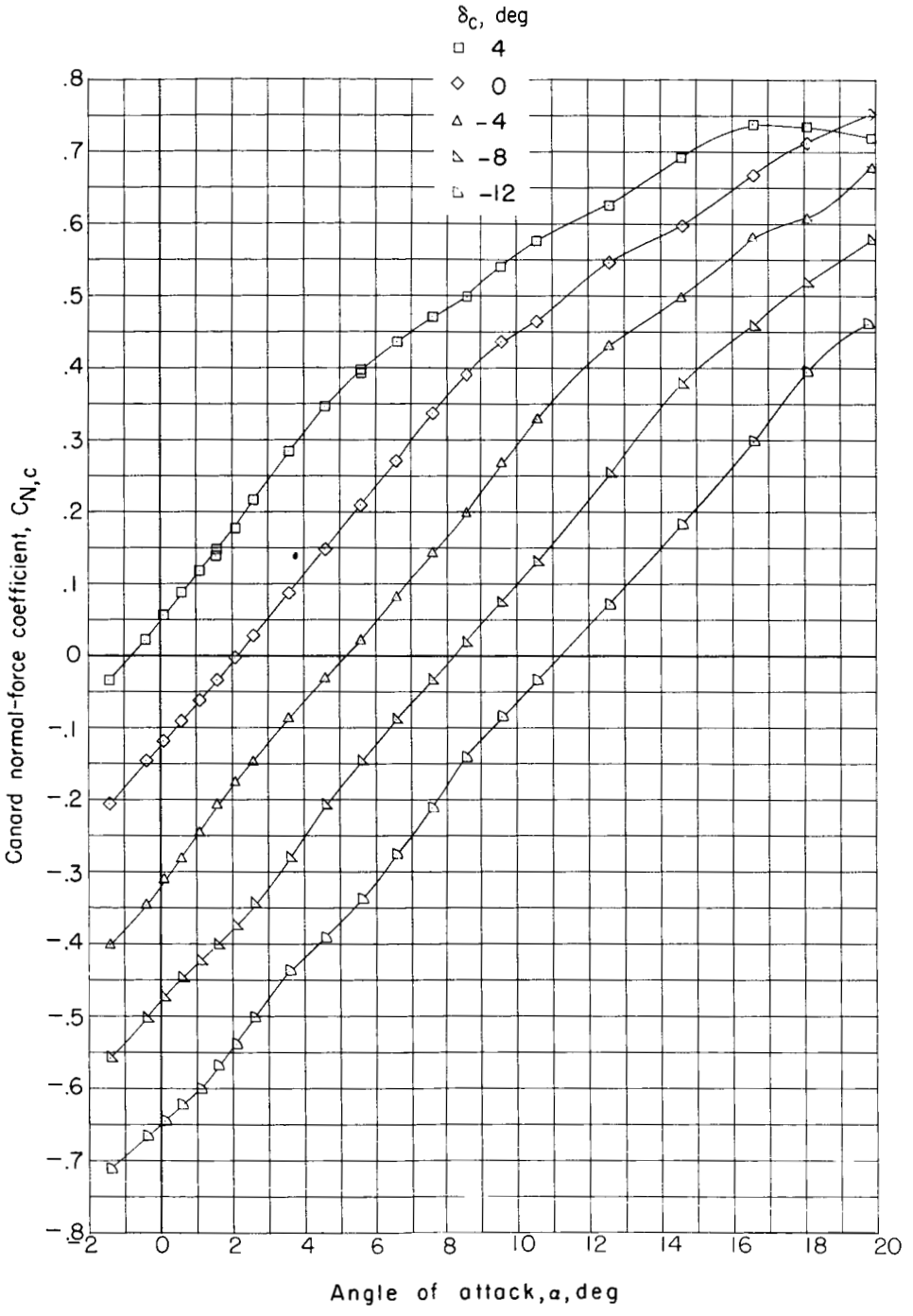

(a) Canard normal-force coefficient.

Figure 47.- Canard normal-force and hinge-moment coefficients for configuration BCWE with $\delta_{le} = 12^\circ$ and $\delta_{tab} = -4^\circ$ at M = 0.85.

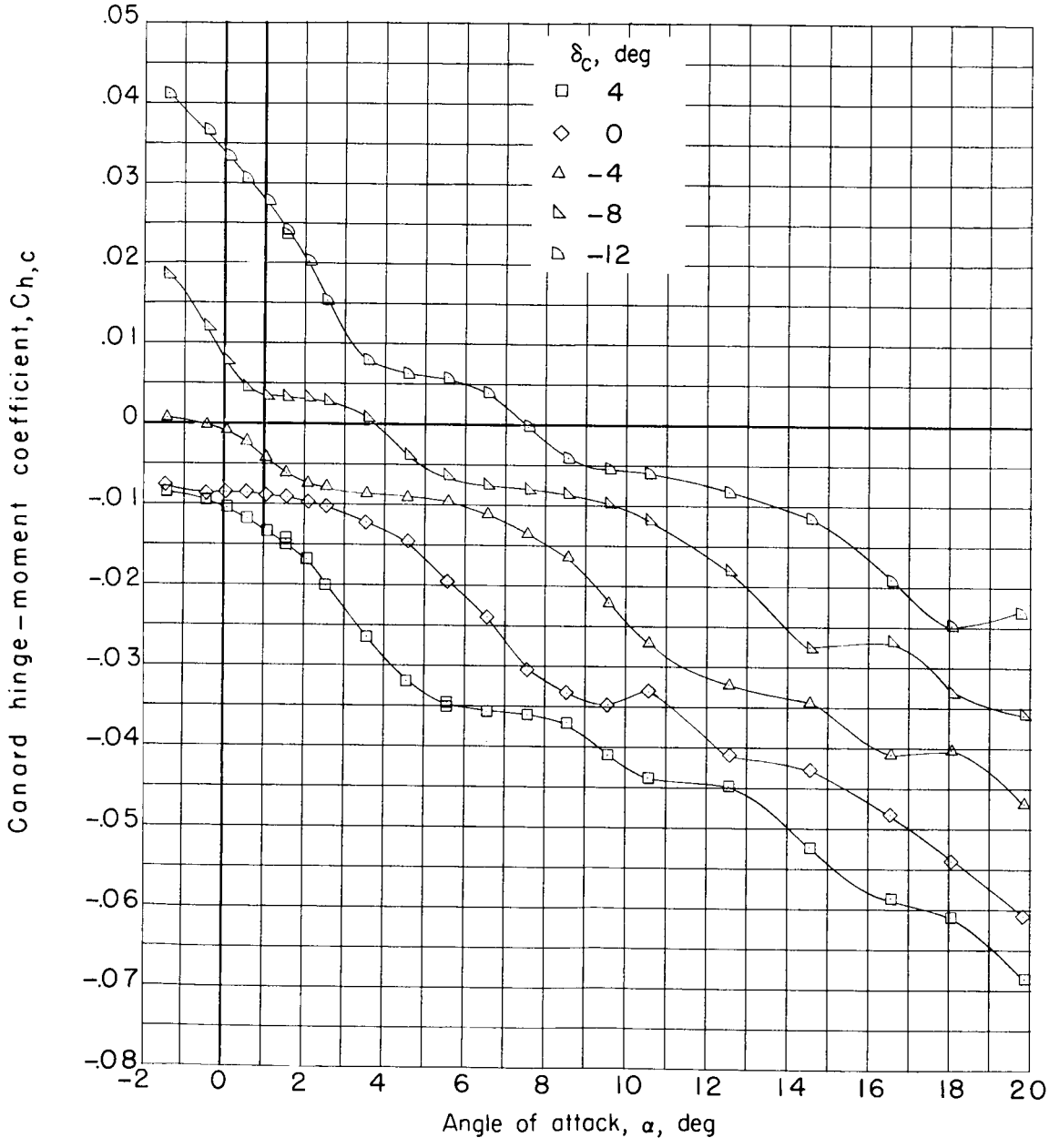

(b) Canard hinge-moment coefficient.

Figure 47.- Concluded.

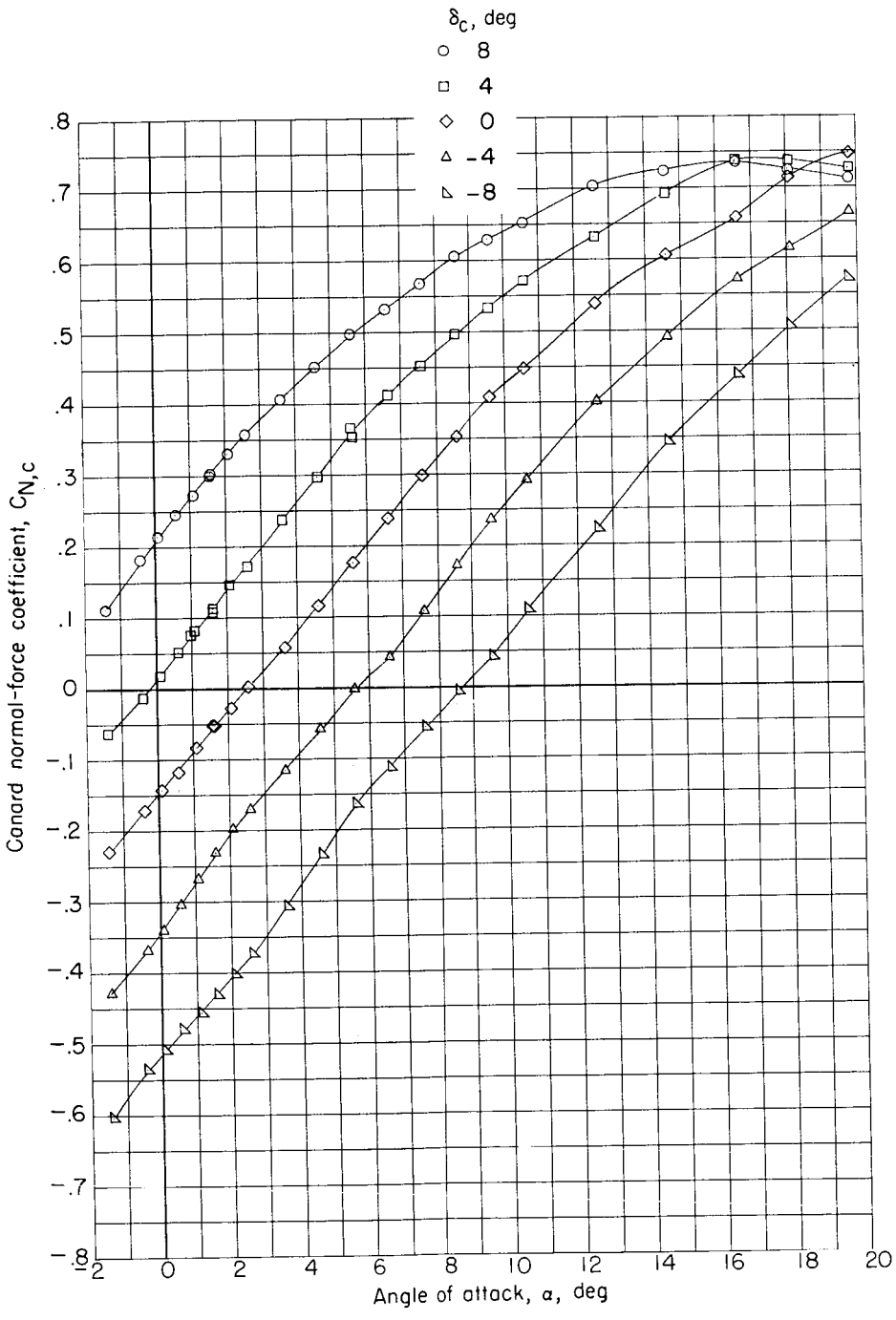

(a) Canard normal-force coefficient.

Figure 48.- Canard normal-force and hinge-moment coefficients for configuration BCWE with $\delta_{le} = 12^\circ$ and $\delta_{tab} = -8^\circ$ at M = 0.80.

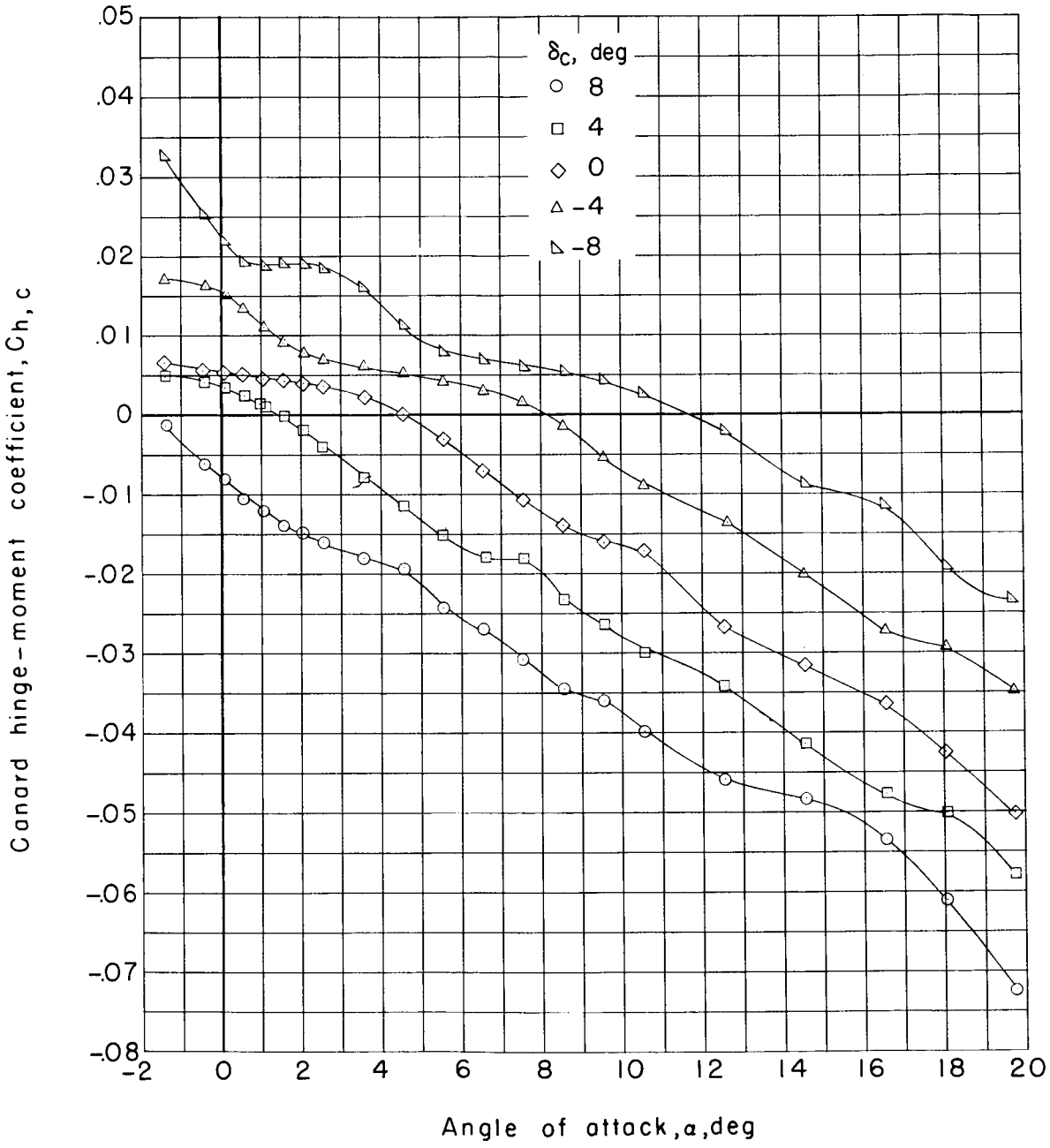

(b) Canard hinge-moment coefficient.

Figure 48.- Concluded.

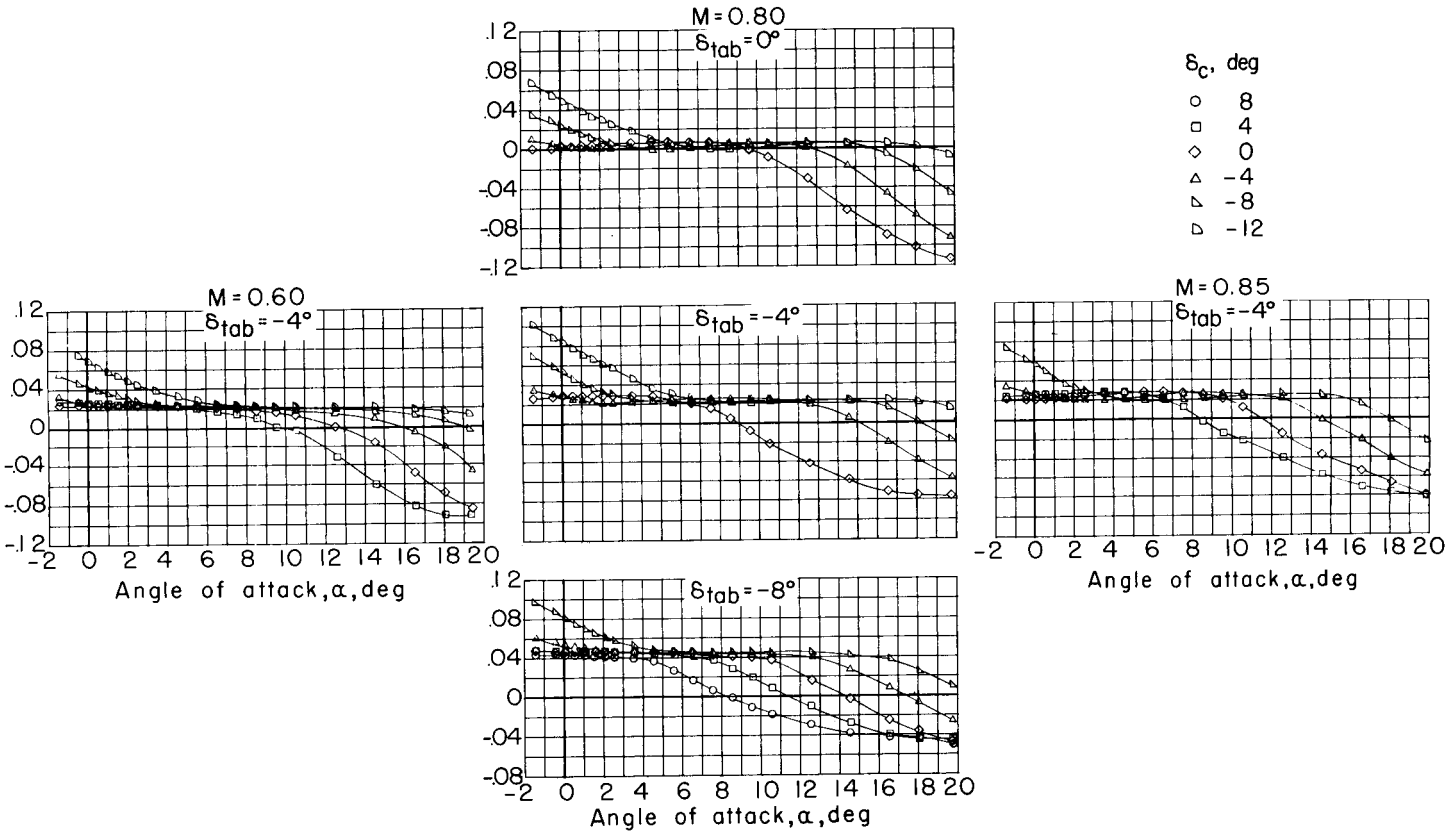

Figure 49.- Tab hinge-moment coefficient for configuration BCWE with $\delta_{le} = 12^{\circ}$.

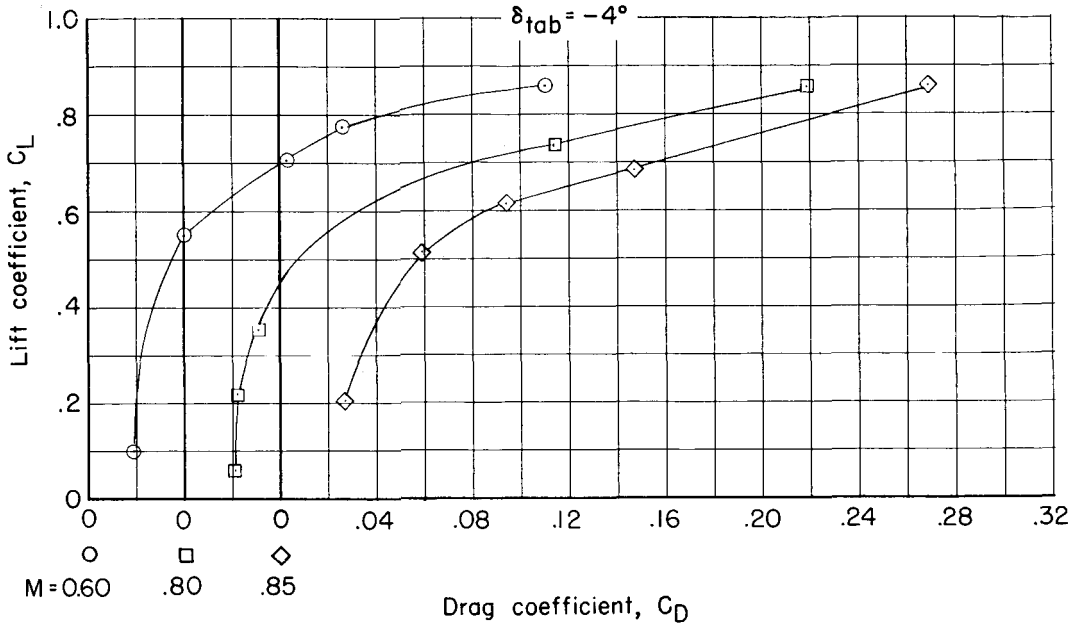

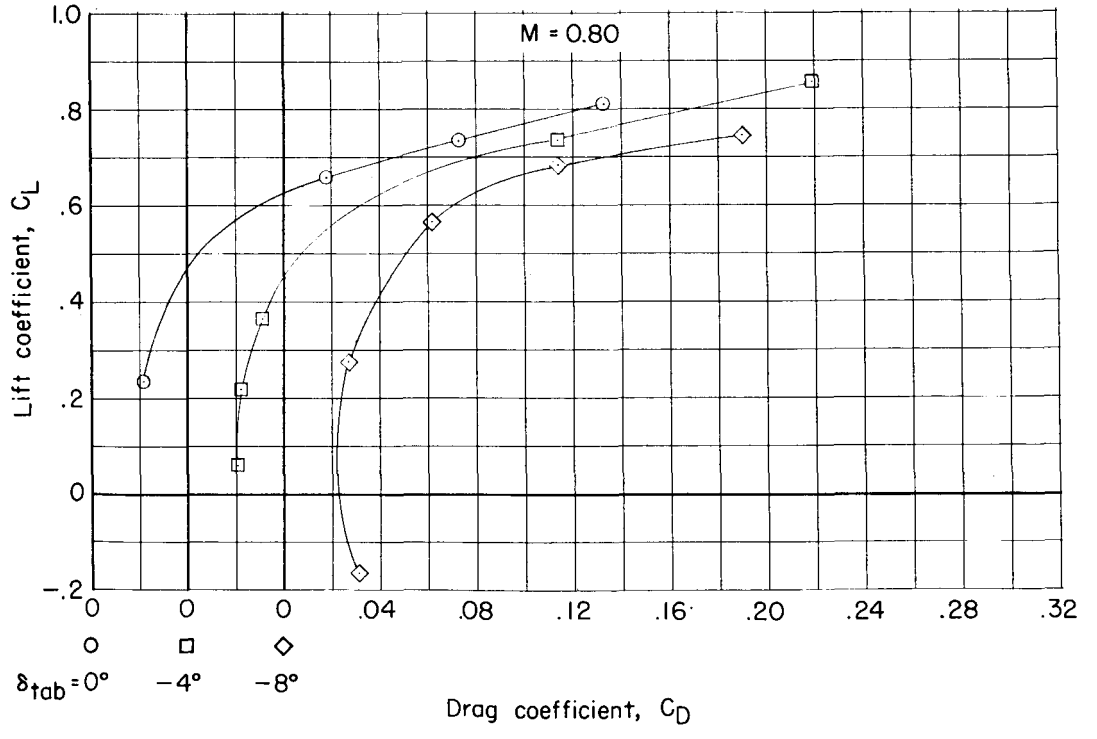

Figure 50.- Variation of trimmed drag polars with Mach number and canard tab deflection for configuration BCWE with $\delta_{le} = 12^{\circ}$. Symbols indicate interpolated points.